University of Massachusetts Amherst
ScholarWorks@UMass Amherst

Doctoral Dissertations 1896 - February 2014

1-1-2007

Adhesion of patterned polymer interfaces.

Edwin Pak-Nin Chan
University of Massachusetts Amherst

Follow this and additional works at: https://scholarworks.umass.edu/dissertations_1

Recommended Citation
Chan, Edwin Pak-Nin, "Adhesion of patterned polymer interfaces." (2007). *Doctoral Dissertations 1896 - February 2014*. 1104.
https://scholarworks.umass.edu/dissertations_1/1104

This Open Access Dissertation is brought to you for free and open access by ScholarWorks@UMass Amherst. It has been accepted for inclusion in Doctoral Dissertations 1896 - February 2014 by an authorized administrator of ScholarWorks@UMass Amherst. For more information, please contact scholarworks@library.umass.edu.

UMASS/AMHERST
312066 0310 4808 1


University of
Massachusetts
Amherst

LIBRARY

Digitized by the Internet Archive
in 2015

https://archive.org/details/adhesionofpatter00chan

This is an authorized facsimile, made from the microfilm master copy of the original dissertation or master thesis published by UMI.

The bibliographic information for this thesis is contained in UMI's Dissertation Abstracts database, the only central source for accessing almost every doctoral dissertation accepted in North America since 1861.

UMI® Dissertation Services

From:ProQuest COMPANY

300 North Zeeb Road
P.O. Box 1346
Ann Arbor, Michigan 48106-1346 USA

800.521.0600 734.761.4700
web www.il.proquest.com

Printed in 2008 by digital xerographic process
on acid-free paper

ADHESION OF PATTERNED POLYMER INTERFACES

A Dissertation Presented

by

EDWIN PAK-NIN CHAN

Submitted to the Graduate School of the
University of Massachusetts in partial fulfillment
of the requirements for the degree of

DOCTOR OF PHILOSOPHY

September 2007

Polymer Science and Engineering

UMI Number: 3289211

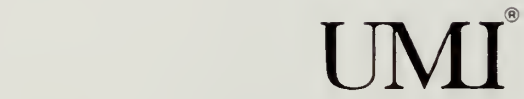

UMI Microform 3289211

Copyright 2008 by ProQuest Information and Learning Company.
All rights reserved. This microform edition is protected against unauthorized copying under Title 17, United States Code.

ProQuest Information and Learning Company
300 North Zeeb Road
P.O. Box 1346
Ann Arbor, MI 48106-1346

© Copyright by Edwin Pak-Nin Chan 2007

All Rights Reserved

ADHESION OF PATTERNED POLYMER INTERFACES

A Dissertation Presented

by

EDWIN PAK-NIN CHAN

Approved as to style and content by:

_____

Alfred J. Crosby, Chair

_____

Thomas J. McCarthy, Member

_____

Narayanan Menon, Member

_____

Shaw Ling Hsu, Department Head
Polymer Science & Engineering

ADHESION OF PATTERNED POLYMER INTERFACES

A Dissertation Presented

by

EDWIN PAK-NIN CHAN

Approved as to style and content by:

Alfred J. Crosby, Chair

Thomas J. McCarthy, Member

Narayanan Menon, Member

Shaw Ling Hsu, Department Head
Polymer Science & Engineering

To my family.

ACKNOWLEDGEMENTS

I want to thank my thesis advisor Prof. Alfred J. Crosby for mentoring me and helping me develop my project. The story of how I chose Al as my advisor is interesting. When I joined PSE 4 years ago, I was dead set on another professor who was much more established in polymer physics. I interviewed with Al on 2 separate occasions. The first time was at my interview in late March 2003, the second was a private talk during my first semester in the program. Both times, I never even considered working for him, partly due to my ignorance about polymer adhesion and partly because I was always intimidated by mechanics. All that changed when he gave his scheduled "sales" pitch to the class later in the first semester. I still don't know what it was that convinced me to work for Al; perhaps when he started to talk about Gecko adhesion. Regardless, I was 100% certain afterwards that I should work for him. Four years have passed and I still think it was the best decision that I have ever made. Al is the best mentor I have had and probably ever will. I cannot thank him enough for all of his encouragement and support. I had two main (there are many more) weaknesses coming in to the program: public speaking and technical writing; Al helped me tremendously in improving in both areas. A funny story, one that he brings up now and then, is how he characterized my writing after reading the first draft of our first paper. He said it was good overall, but that I wrote like Quentin Tarantino directs movies. Initially, I thought it was a compliment since he is a famous movie director. Then Al elaborated and I realized that he meant that my story writing is like Pulp Fiction – everything is described backwards. There are not enough pages to describe what a greater mentor Al is, but bottom line, Al, thank you for making me the scientist I am today.

I would also like to thank Prof. Thomas J. McCarthy and Prof. Narayanan Menon for being on my thesis committee. A funny story with Tom occurred during my Original Research Proposal when I proposed studying aerosol particles for drug delivery. Slide two into my talk, Tom asks: "Do you know how free-basing works?" Of course I did not know and Tom goes on to explain why free-basing is so effective in intoxicating people. Keep in mind that this was slide two of my talk, at this time, I was freaking out and thinking, "what will he asks next?" But if anyone knows Tom, he is just a very inquisitive guy. The same is true for Prof. Menon; he always makes sure that I know I derive all my equations properly. Al, Tom and Prof. Menon are scientists that I admire and respect the most, as you can tell they that really love doing science.

I want to thank all of my lab-mates (Jong-Young Lee, Charles (CJ) Rand, Douglas Holmes, Jessica Zimberlin, Derek Breid, as well as post-docs Kyriaki Kalaitzidou and Santanu Kundu) and co-workers that I have worked with during my time at PSE for they help and feedback of my work. Jong-Young, CJ and I were Al's first students, so, we went through a lot of the initial development of the group. To Jong-Young, thank you for proof-reading my manuscripts and giving me feedback. I will always miss our lunch time, going to get noodle bowl at the Campus Center or going to the Diner in Sunderland for some fried chicken, and also the funny stories about picking up dinosaurs on motorcycles. To CJ, thanks for all the suggestions for my research, but mostly for being a good friend. We had some fun times at conferences and I am sure you will always let me know about the ONE time that you beat me at something – the Adhesion Society Poster Competition. It has been a fun 4 years and interesting to see how the group has evolved.

I also want to thank all the REUs that I got to work with (Erica Smith, Andrew Smith and John Wang). Special thanks go to Erica as she helped develop the wrinkled adhesive project. She is a great experimentalist and tried a lot of crazy ideas that I wanted to try, but didn't have enough time to complete them.

Last, but certainly not least, I want to thank the support and encouragement of my family (Mom – Avis, Dad – Francis and sister – Dorothy). I dedicate this thesis to my parents. Mom and Dad, I would not be who I am today without your love, support, and encouragement. Thanks.

ABSTRACT

ADHESION OF PATTERNED INTERFACES

SEPTEMBER 2007

EDWIN PAK-NIN CHAN, B.S., PENNSYLVANIA STATE UNIVERSITY

M.S., MASSACHUSETTS INSTITUTE OF TECHNOLOGY

PH.D., UNIVERSITY OF MASSACHUSETTS AMHERST

Directed by: Professor Alfred J. Crosby

Nature has demonstrated that a powerful strategy for tuning adhesion lies in the development of patterns at an interface. Inspired by the amazing attachment abilities of geckos, we demonstrate that similar design approaches can tune the adhesion of polymer interfaces. In this research, we investigate the role of patterned surfaces in the control of polymer adhesion. Specifically, we demonstrate that patterned surfaces control adhesion by enhancement of the total contact line, or perimeter of the interface, as opposed to increasing the total contact area. This insight is very powerful as it provides new strategies for designing patterned adhesives.

To demonstrate that the pattern control of adhesion is associated with the enhancement in contact line, we explore two unique types of patterned interfaces and their control in adhesion. First, we begin our investigation of patterned adhesion (Chapter 2) by understanding how surface-chemical patterns – i.e. a pattern of periodic variation in surface chemistry, can tune the adhesion of a commercial silicone elastomer. This type of patterned adhesive is unique as almost all previous patterned adhesives are based on topographic patterns. We find a surface-chemical pattern can enhance the adhesion of the elastomer and significant increases are observed for specific pattern geometries. More importantly, the mechanism of enhancement is linked to the changes in the contact line which is controlled by the periodic variation in surface chemistry.

Our results on the adhesion of surface-chemical patterns open new opportunities for developing alternative patterned interfaces for adhesion control. Since the mechanism of control is associated with the enhancement in contact line, we explore an alternative patterning strategy without the use of lithography. In Chapter 3, we explore the concept of surface wrinkling to pattern polymers. We use a combination of osmotic stress, coupled with lateral confinement to generate wrinkles on polymer surfaces. We show control of both the orientation and the length-scale the wrinkle patterns. The wrinkles form as a result of the development of a compressive stress within the polymer film due to the balance between osmotic stress and lateral confinement. There are two main contributions from this work. First, we demonstrate the control of the degree of lateral confinement determines the wrinkling morphology. More importantly, this control leads to the discovery of two new wrinkling morphologies that have not been observed previously. Second, our approach provides direct applications of these structured

materials as functional devices. Specifically, we illustrate that our wrinkled polymers can directly be used as an optical array or patterned adhesive (Chapter 4).

In Chapter 4, we combine the lessons learned in the adhesion of surface-chemical patterns (Chapter 2) along with the patterning approach based on surface wrinkling (Chapter 3) to generate a "self-patterned" wrinkled "smart" adhesive. We demonstrate that the adhesive properties are connected with the wavelength of the surfaces wrinkles. With the understanding of the mechanism of contact line enhancement, wrinkled patterns are developed that enhance adhesion by increasing the total contact line during separation. Based on the mechanism of contact line splitting, we develop a scaling relationship that explains how the contact line enhancement is controlled by the wavelength of the wrinkles.

TABLE OF CONTENTS

LIST OF TABLES

LIST OF FIGURES

CHAPTER ONE

INTRODUCTION

1.1 Project Overview

Broadly defined, adhesion is the study of the strength of an interface. While adhesion can be considered as simple as the sticking of two surfaces together with Scotch™ tape or glue, the field of adhesion has much broader technological impacts. In microelectronics, adhesion is necessary to ensure that interconnects adhere to bond wires and pass current. For structural applications that use carbon fiber, adhesion is needed to bond fibers with the epoxy matrix to ensure high strength. However, there are instances where the enhancement in release properties (equivalent to a lack of adhesion) is equally important. For example, a Band-Aid should be easily removed from the skin on demand or when the wound has healed. In micro/nanofabrication technologies such as imprint lithography, the enhanced release of a template from the molded polymer film is crucial to the success of pattern replication in polymer films. Hence, our goal is not just to maximize or minimize interfacial strength but to be able to control adhesion. There are numerous parameters that control polymer adhesion (i.e. – mechanical properties, surface energy, surface roughness, etc.), but in our research, we focus on the impact of well-defined surface patterns on adhesion. The surface patterns can be naturally occurring such as surface roughness or predefined topography, as in the case of certain insects and lizards. As we demonstrate in our work, topography can have a significant impact on adhesion; we explore the role of topography in controlling adhesion and use it to control the strength of polymer interfaces.

The focus of our research is the study of adhesion of patterned polymer interfaces. Specifically, we understand the role of microscale patterns on the adhesion of soft elastomers. This thesis is divided into four parts. Chapter 1 gives a background to polymer adhesion and discusses previous work in the field of patterned adhesion. In Chapter 2, we begin our study with understanding how surface-chemical patterns – i.e a pattern of periodic variation in surface chemistry, can tune the adhesion of a commercial silicone elastomer. As we demonstrate in Chapter 2 and 4, the primary mechanism of adhesion control is the contact line, as opposed to contact area of the interface. In Chapter 3, we develop an alternative strategy to generate patterned polymer surfaces. We explore the concept of surface wrinkling as a "self-assembled" approach to pattern polymers. To demonstrate understanding and control, we establish scaling laws relating the wrinkling morphology with the materials' properties. We further develop the surface wrinkling approach in Chapter 4 to generate wrinkled, soft polymer surfaces for adhesion control. We quantify the adhesive properties of these "self-assembled" wrinkled surfaces and understand the role of wrinkles in controlling adhesion. Chapters 2 through 4 are modified peer-reviewed publications that include additional experiment details. Finally, in the appendix, we include another publication dealing with adhesion issues in imprint lithography.

1.2 Polymer Adhesion

In describing polymer adhesion, we are interested in the separation process between a polymer adhesive and another material such as a rigid surface. For elastic

materials that are non-patterned, adhesion is often described by the critical energy release rate or critical adhesion energy, G_c. This descriptor represents the critical driving force for moving a "crack" at an interface and has units of energy per area. Specifically, G_c represents the amount of energy required to drive the crack forward a unit area, dA. An important point to note is that G_c does not represent the properties of a single material but contributions from both materials (i.e. the polymer adhesive and the rigid surface). If the applied driving force is greater than a critical value (i.e. G_c), then the interface will separate. Once G_c is known for a given materials interface, then practical design parameters such as the maximum sustainable force or stress for a given geometry can be determined.

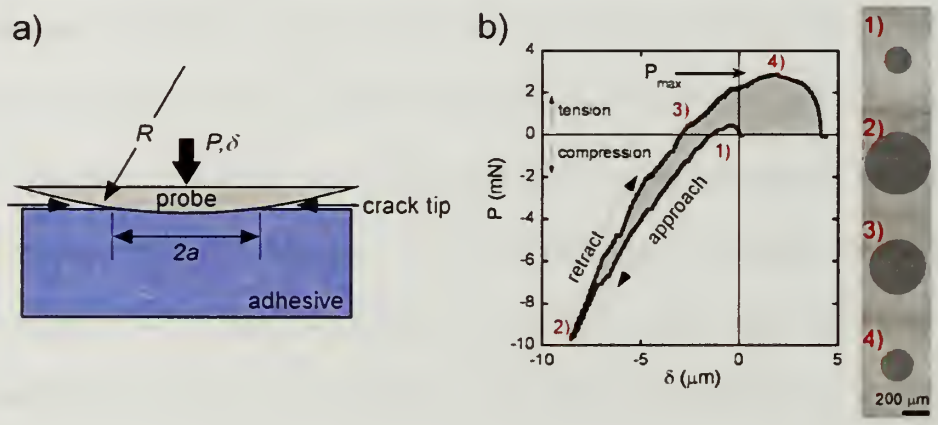

Figure 1.1 – A probe-type contact adhesion test. a) Formation of an interface between a rigid probe surface and a deformable adhesive. b) The results for a contact adhesion test between a rigid probe and deformable elastomer. Figure reproduced from Chan *et al.*[1]

Frequently the contact probe adhesion test is used to measure the adhesion for both patterned and non-patterned materials (Fig. 1.1a). In contact probe testing, a probe (e.g. a circular punch or spherical cap) is brought into contact with another material, and the established interface is subsequently separated. During the process of interface

formation and separation, the force, P, displacement, δ and contact area ($A=\pi a^2$) are monitored to provide a complete description of the adhesion properties (Fig. 1.1b). These measured parameters are used to calculate G_c in a straightforward manner using existing theories. From G_c, practical adhesion descriptors such as the maximum separation force and stress can be determined. The direct relationship between G_c and these practical adhesion descriptors depends on the specific contact geometry. For example, the maximum separation force, P_s, for a hemispherical probe scales with the radius of curvature of the probe, R and G_c:[2]

$$P_s = \frac{3}{2}\pi G_c R \tag{1.1}$$

For a circular punch of radius, a:[3]

$$P_s = \left(\frac{8\pi E G_c a^3}{1-\nu^2}\right)^{1/2} \tag{1.2}$$

where E and ν are the elastic modulus and Poisson's ratio of the adhesive and we have assumed that the probe is much stiffer than the adhesive. Based on these relationships, we see that the maximum separation force is geometry-dependent. P_s for a hemispherical probe is independent of elastic properties as well as the maximum contact area; whereas, P_s for a circular punch is dictated by both the elastic properties and dimensions of the interface. If we normalize for a circular punch by the interfacial area to define an average stress, σ_s, then P_s is still dependent upon dimensions and materials properties:

$$\sigma_s = \frac{\left(\frac{8\pi E G_c a^3}{1-\nu^2}\right)^{1/2}}{\pi a^2} = \left(\frac{8EG_c}{\pi(1-\nu^2)a}\right)^{1/2} \tag{1.3}$$

For patterned interfaces, G_c cannot be defined quantitatively; therefore, most researchers (including ourselves) have substituted descriptors such as P_s, σ_s, and a term called W_{adh}.

$$W_{adh} = \frac{\oint P \cdot d\delta}{\pi a^2} \tag{1.4}$$

W_{adh} is defined by the energy dissipated during the contact and separation of a contacting probe normalized by the maximum contact area.[4, 5] For elastic materials, W_{adh} is related to G_c:[4]

$$W_{adh} = \frac{2\pi \oint G_c \cdot a \cdot da}{\pi a^2} \tag{1.5}$$

It is important to note that these quantities are useful, but they do not represent absolute properties. For example, W_{adh} will not approach thermodynamic quantities for fully reversible materials (since the formation and separation of the interface is non-hysteric, therefore, $W_{adh} = 0$), and it is dependent upon the maximum interfacial contact area. Also, P_s, σ_s and W_{adh} will depend upon the contact history, such as maximum compressive force during interface formation. A summary of the descriptors used to quantify adhesion is presented in Table 1.1.

Finally, while G_c is a materials-defined quantity, there are certain limitations or assumptions we must make to justify its use. In all of our previous discussion, we have assumed that the deformation occurs at or near the interface – the crack tip (Fig. 1.1a), and the applied energy is all supplied to advance the crack by *da*. If this assumption is justified, then G_c can be used to quantify the amount of energy needed for interfacial separation. Since most polymers are dissipative (rate-dependent response), we can still

justify the use of G_c if the dissipative processes are localized at the crack tip. If bulk, dissipative processes, such as bulk viscoelastic processes occur, than the use of G_c cannot be justified. In this case, alternative descriptors such as stress-intensity factor should be used. As we demonstrate in this thesis, each of the adhesion descriptors of P, σ, G_c and W_{adh} are unique in describing adhesion. As certain descriptors are more easily quantifiable when dealing with patterned adhesion, we use these different descriptors wherever appropriate.

	Descriptor	Comments	Advantages	Disadvantages
FORCE	P_{sep} *separation force*	For single fibril $=1.5\pi G_c R$ JKR contact $=\left(8\pi G_c E^* a^3\right)^{1/2}$ Flat punch contact	• simple quantification of strength	• extensive property • ignores contact geometry
FORCE	σ_{app} *contact strength*	$=\frac{P_{sep}}{A_{app}}$ • A_{app} is the projected or apparent contact area	• simple quantification of strength	• extensive property since it is normalized by apparent contact area
FORCE	$\overline{P}_{sep}$ *normalized separation force*	$=\frac{P_{sep,pattern}}{P_{sep,nonpattern}}$	• straightforward comparison with reference nonpatterned material	• extensive property • ignores contact geometry
ENERGY	U_{adh} *total separation energy*	$=\int P \cdot d\delta$	• accounts for total energy needed to form and fail the interface, including dissipative events such as viscoelastic effects	• extensive property • ignores contact geometry
ENERGY	G_c *critical adhesion energy*	• Defines the critical energy needed to cause the interface to fail spontaneously • Relevant forms of the expression depend on the contact geometry • For reversible systems, this quantity approaches the thermodynamic work of adhesion	• intensive property of the material • classic descriptor of adhesion	• cannot be rigorously implemented to account for viscoelastic effects • difficult to measure for patterned interfaces
ENERGY	W_{adh} *work of adhesion*	$=\frac{\int P \cdot d\delta}{A_{max}}$ • A_{max} is the true contact area at maximum compression	• accounts for energy dissipation across a defined contact area • practical description of adhesion for patterns	• extensive property • depends on true contact area
ENERGY	$\overline{W}_{adh}$ *normalized work of adhesion*	$=\frac{W_{adh,pattern}}{W_{adh,nonpattern}}$	• straightforward comparison with reference nonpatterned material	• extensive property • depends on true contact area

Table 1.1 – The different force and energy descriptors used to quantify adhesion. Table reproduced from Chan *et al.*[1]

1.3 Patterned Adhesion – Inspirations from Nature

The inspiration for studying the adhesion of patterned interfaces comes from nature. Many animals and insects use patterns to control adhesion and release. In the case of the gecko lizard and jumping spider, their feet are decorated with a hierarchical

arrangement of fibrillar microstructures called setae that allows them to walk on vertical surfaces (Fig. 1.2).

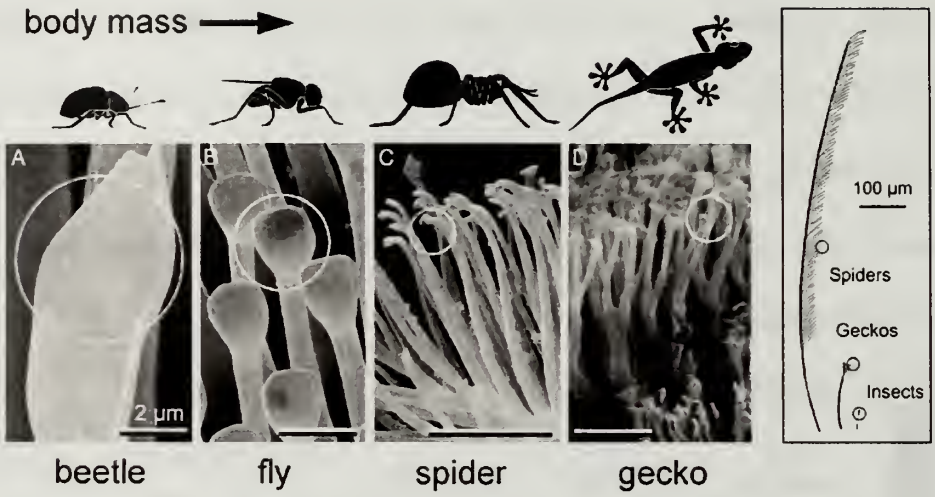

Figure 1.2 – Examples of fibrillar microstructures that decorate the feet of various insects and lizards. Figure reproduced from Arzt *et al.*[6]

In the gecko, the foot pads consist arrays of keratinous setae each approximately 100 µm in length and 5 µm in diameter. The seta then branch into arrays of smaller fibrils called spatulae.[7] The tip of a spatula is terminated by a flattened triangular pad approximately 200 nm in width. While the surface forces responsible for the strong adhesion in the gecko can vary (i.e. – weak van der Waals[8] versus capillary forces[9]), it is clear that the geometry of the fibrillar structure plays a critical role in controlling adhesion. In fact, morphological characterization by Arzt and coworkers show that pattern density is dependent upon the size of the animal (Fig. 1.3).[6]

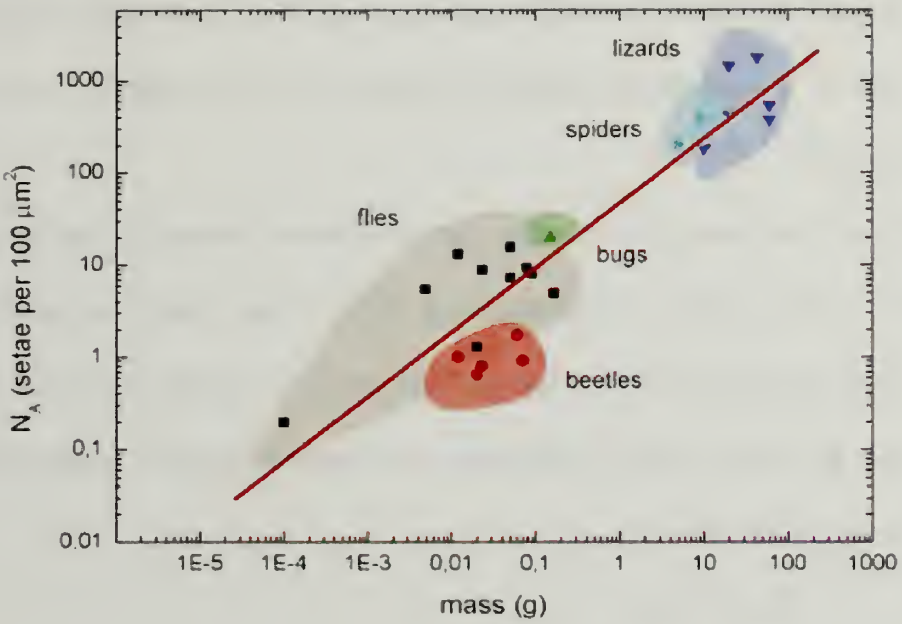

Figure 1.3 – Plot of setae density vs. mass of the animal for various insects and lizards. The setae density, N_A represents the number of setae per area. Hence, the value of N_A is independent of number of feet present for a given animal. Figure reproduced from Arzt *et al.*[6]

1.3.1 Enhancement by Contact Splitting

Nature has demonstrated that a patterned interface can provide enhanced control of adhesion, but how does the patterned interface contribute to the enhanced control of adhesion? While there are many possible contributions by a patterned interface, we can consider specific aspects of the pattern to understand the role of the pattern.

If we again consider the fibrillar interface of the gecko, it would seem counter-intuative to expect that a patterned interface would enhance adhesion (relative to the smooth analog) since breaking up the contacts reduces the contact area. Although the contact area is reduced for a patterned surface, its total contact line (defined by the sum contribution of the perimeter of each contact) can be increased provided the patterns are properly designed. This enhancement of increasing the total contact line length with

topographic patterns, referred to as contact splitting, has been demonstrated by several research groups as the primary mechanism for the enhanced control of polymer adhesion.[4, 5, 10]

We can understand how contact splitting enhances adhesion by the following examples (Fig. 1.4). Consider the peeling of a Scotch™ tape from a substrate (Fig. 1.4a, top image). Since the geometry is a peel test, the force required to peel the tape of width, w_s away from the surface is defined by the Kaelble equation.[11] In this specific geometry, the separation force is:

$$P_{s,s} = 2 \cdot (G_c w_s) \tag{1.6}$$

The separation of this interface is related to the separation force normalized by the total contact area.

$$\sigma_{s,s} = \frac{2 \cdot (G_c w_s)}{w_s^{\,2}} \tag{1.7}$$

To create a patterned peel surface, we will split up tape into n individual square contacts (Fig. 1.4a, bottom image), each with width, w_f. If all the individual contacts are identical in dimensions, and are all loaded simultaneously during separation, then the total separation force, $P_{s,n}$ to peel n independent contacts simultaneously is:

$$P_{s,n} = n \cdot (2 \cdot G_c w_f) \tag{1.8}$$

Again, the separation strength is defined as the separation force divided by the apparent contact area, which is w_s^2.

$$\sigma_{s,n} = \frac{n \cdot (2 \cdot G_c w_f)}{w_s^{\,2}} \tag{1.9}$$

As a comparison, we will set the total interfacial contact identical for both the smooth and the patterned tapes. Since we have assumed that the lateral dimensions for both the smooth and the patterned tapes to be squares, then:

$$A_s = w_s^{\,2} = A_n = n \cdot w_f^{\,2} \tag{1.10}$$

Rearrangement of Eqn. (1.10) leads to the following relationship between w_s and w_f.

$$w_s = n^{1/2} \cdot w_f \tag{1.11}$$

Substitution of Eqn. (1.7) and (1.9) into (1.11) shows that the peel strength for a patterned interface enhances adhesion by $n^{1/2}$ relative to the smooth peel interface.

$$\sigma_{s,n} = n^{1/2} \cdot \sigma_{s,s} \tag{1.12}$$

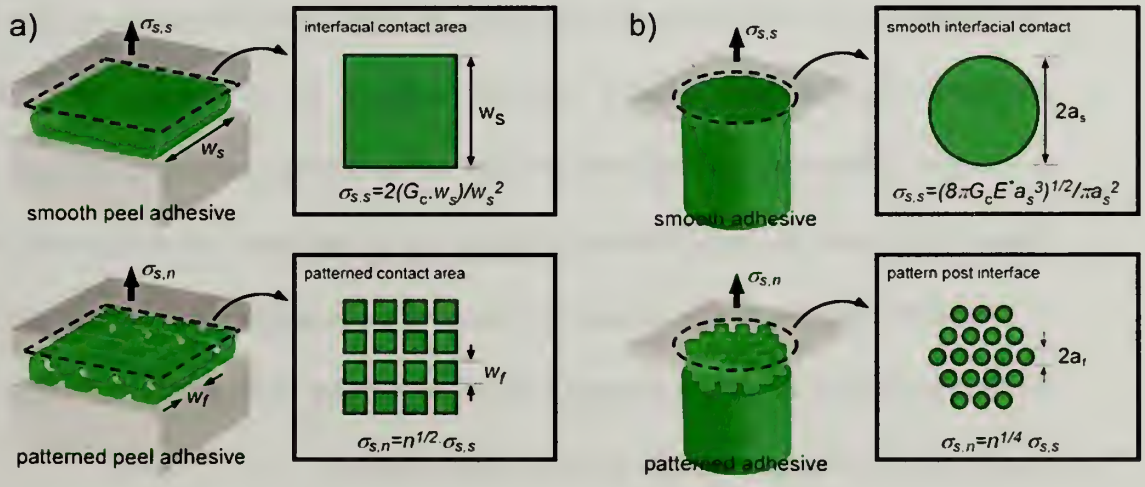

Figure 1.4 – Examples demonstrating the principle of contact splitting for a) peel geometry and b) cylindrical punch geometry. For both examples, separation strength of the patterned adhesive, $\sigma_{s,n}$ increases with the total number of split-up contacts, n which illustrate that the enhancement in strength is associated with the increase in contact line, as opposed to contact area. Figure reproduced from Chan *et al.*[1]

Similar scaling relationships for other contact geometries such as flat punch and hemispherical contacts can be similarly established. For flat punch contact (Fig. 1.4b,

top image), the separation force and strength for a smooth cylinder, $P_{s,s}$ and $\sigma_{s,s}$, respectively are:[3]

$$P_{s,s} = \left(8\pi E^* G_c a_s^{\,3}\right)^{1/2} \tag{1.13}$$

$$\sigma_{s,s} = \frac{\left(8\pi E^* G_c a_s^{\,3}\right)^{1/2}}{\pi a_s^{\,2}} \tag{1.14}$$

Based on the same arguments presented for the peel geometry, it is easy to show that the separation strength for n array of flat punch contacts, $\sigma_{s,n}$ is enhanced relative to the smooth (Fig. 1.4b, bottom image):

$$\sigma_{s,n} = n^{1/4} \cdot \sigma_{s,s} \tag{1.15}$$

Regardless of the specific contact geometry, the scaling relationships suggest that a patterned interface can enhance adhesion relative to its smooth, non-patterned counterpart. However, the important assumption for contact splitting is that the energy release rate associated with initiation separation at the perimeter of each pattern feature to be greater than the energy release rate required for propagation.[1] Hence, increasing the number density of pattern features leads to an increase in the number of independent crack initiation sites provided by each contact perimeter.

Additionally, contact splitting stipulates that, 1) coupling between individual contacts does not occur or is minimized, and 2) the individual contacts are all loaded simulataneously. This second assumption of simulataneous is commonly referred in literature as equal load sharing.[12] If one or both of these conditions are not met, then, there will be a reduction in efficiency for enhancement by the patterns. In other words, the true enhancement, as reflected by n, will be lower than the theoretical n value.

1.3.2 Effects of Fibrillar Aspect Ratio

In the above discussion of contact splitting, we have largely ignored the aspect ratio (i.e. the ratio of fibril length versus fibril diameter of a setae) of the pattern features. In other words, the enhancement by contact splitting only assumes interfacial contributions by increasing the total contact line. Aspect ratio comes into play weakly in that taller features increase the efficiency of the pattern in maximizing the condition of equal load sharing. However, the high and defined aspect ratios of many natural fibrillar attachment devices (~20 for terminal fibrils of the gecko) suggest that their geometry provides a specific function.

One attribute of high-aspect features is that it offers a practical solution to adaption to natural terrain (i.e. surface roughness). As a fibrillar interface is a more compliant surface, it is better able to adapt and conform to rough surfaces; hence, it can maximize contact. In addition to increasing interfacial contact, a fibrillar interface can provide greater separation strength. Chung and Chaudhury conjectured that the fibrillar microstructure enhances the adhesive strength of the interface compared to a smooth interface as more energy is dissipated for the fibrillar interface during separation.[13] This enhancement in adhesion energy can be explained if we consider a peeling experiment for the two elastic systems: a smooth adhesive versus a fibrillar adhesive. Since the material is continuous, as we peel the smooth adhesive away from the interface, the applied energy needed to drive the separation (or crack advancement) is stored in the material. The material directly ahead of the crack tip is pulled into tension and as the crack advances, the stored elastic energy is released back into the material to help drive the crack forward until the adhesive completely separates. The mechanism of

separation is different for the fibrillar interface; as a fibril unloads, the elastic energy stored within the fibril cannot be easily transferred to a neighboring fibril as they are not in intimate contact. Much of the stored energy does not contribute to advancing the crack and is lost. Compared with the smooth adhesive, more energy must be supplied in order to completely separate the fibrillar adhesive and results in significantly greater applied adhesion energy. Hence, this mechanism of energy dissipation provides motivation for designing a fibrillar interface with high-aspect features.

1.4 Previous Work on Patterned Adhesives

Inspired by the amazing adhesive ability of the gecko, researchers have attempted to mimic the gecko microstructure and fabricate a reusable, dry adhesive. Independent efforts by Glassmaker *et al.*[14, 15], Geim *et al.*[16] as well as others[12, 17-19] have successfully fabricated dense arrays of flexible polymer pillars or plate-like fibrils to create the so-called "gecko tape" (Fig. 1.5).

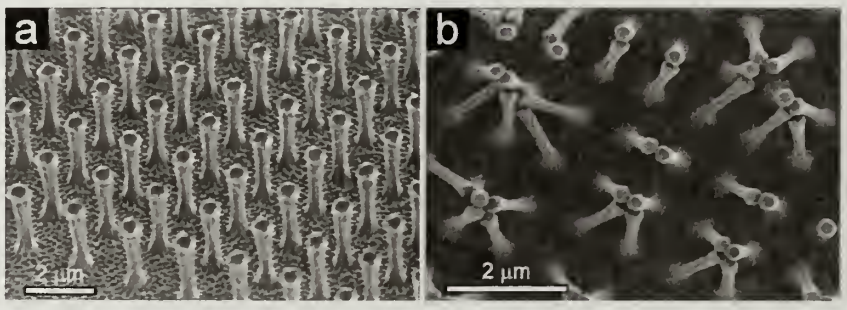

Figure 1.5 – Example of a "gecko tape". a) This tape consists of an array of polymer fibrillar structures. b) The adhesive properties depend on the total number of contacts of the fibrils, however, the adhesive properties reduces upon "condensation" of the fibrils. Figures reproduced from Geim *et al.*[16]

While these synthetic fibrillar adhesive have comparable dimensions (submicron length scale) with their natural counterpart, whether they demonstrate enhancement

remains inconclusive. It appears that the adhesive properties of the "gecko tape" depend on 1) the number of fibrils that are attached to the interface (which is difficult to quantify) and 2) the loading history of the adhesive. However, the durability of these "gecko tapes" is limited as the adhesive properties degrade gradually over multiple attachment-detachment cycles which the researchers attribute to the permanent lateral collapse of the highly flexible microstructures.

Although it seems desirable to create an adhesive that mimics the fibrillar microstructure of the gecko, other patterns have been used to generate adhesion enhancement. One of the earliest adhesion studies on synthetic patterned interfaces is the work by Kendall on composite films.[20] In his work, Kendall illustrated the effects of bending stiffness contrast (either differences in elastic moduli or geometric stiffness) on the fracture toughness (applied adhesion energy) of the composite film (Fig. 1.6) as the film peels away from the surface.

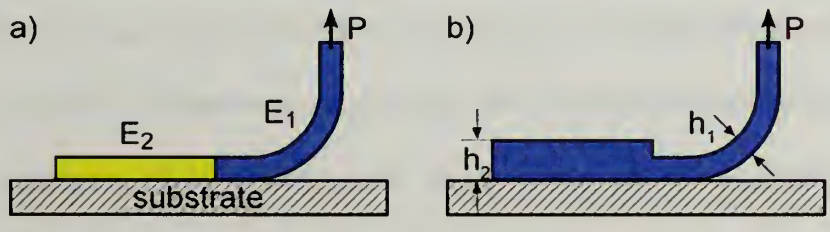

Figure 1.6 – The two forms of peel geometry explored by Kendall[20] that demonstrates effects of changes in bending stiffness on the adhesion energy. The bending stiffness of the overall peel film can be varied by a) changing the elastic modulus or b) changing the film thickness.

The presence of alternating compliant and stiff regions enhances fracture toughness in two ways. First, the composite films demonstrate an increase in the applied adhesion energy. Since the stiff medium has a higher bending stiffness, the region resists the mechanical deformation and therefore retards the propagation of the crack.

As a result, additional elastic energy must be applied in order to overcome the resistance from the stiff medium. Second, the presence of the compliant-stiff interfaces results in the modulation of the crack propagation velocity. The presence of the interfaces that separates the stiff and compliant regions functions as "speed bumps', the crack decelerates as it encounters the stiff interface and accelerates when it meets the compliant interface. In essence, the interface separating the stiff and compliant regions is serving to discrupt the crack propagation process. As we show in Chapter 2, a similar mechanism of control can be achieved with surface chemical patterns where there is a periodic change in the adhesion energy as opposed to a change in elastic constants.

More recent work by Chaudhury and co-workers reports a 25-fold increase in the W_{adh} relative to an non-patterned interface of the same material by patterning a crosslinked poly(dimethyl siloxane) (PDMS) thin film with arrays of lines or squares and measuring the adhesion in a peel test geometry.[13, 21] As illustrated by Fig. 1.7, the patterns differ markedly with the gecko's fibrillar microstructure as the aspect ratios in these patterns are quite low. The researchers argue that the increase in W_{adh} is similar to the mechanism in the gecko, as the crack propagates, the presence of discontinuities (the gaps that separate the adhesive pads) that decorate the adhesive leads to the irreversible dissipation of the stored elastic energy immediately behind the crack tip. Furthermore, the authors suggest that the discontinuities act as obstacles for the crack; crack propagation is arrested upon encountering the void region and must re-initiate in order to continue propagation. A multitude of such re-initiation events ultimately leads to the dissipation of elastic energy.

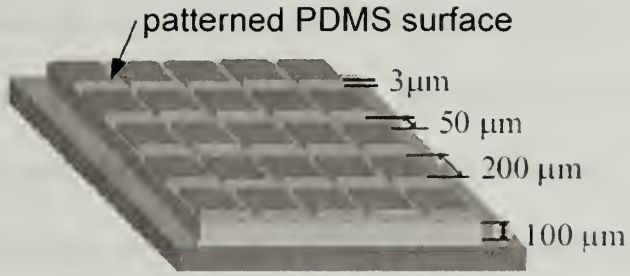

Figure 1.7 – A thin PDMS film that is patterned with shallow incisions. Figure reproduced from Ghatak *et al.*[21]

1.5 Length-scale Dependence in Adhesion

What are the important materials' parameters that can be used to optimize the design for the patterned adhesives? From a materials engineering perspective, how do we intelligently design patterns to provide control of adhesion and release, and more importantly, with properties that are maintained over the course of multiple uses?

One design principle in relating materials' properties to length scale in adhesion can be understood by adapting an example presented by Shull and coworkers.[22] Consider the adhesion between a flat cylindrical punch of radius, a and a soft, elastic adhesive with elastic modulus, E (Fig. 1.8).

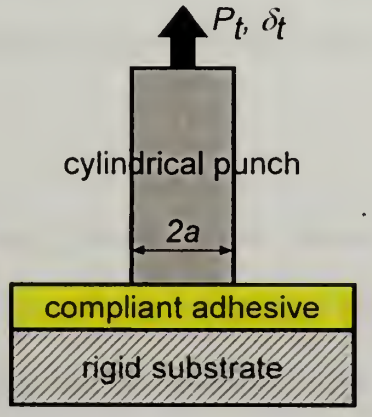

Figure 1.8 – General geometry of an adhesion test between a cylindrical flat punch and a compliant adhesive.

As the punch retracts from the adhesive, the adhesion energy of the adhesive-punch interface provides the resistance for separation, and a defined load, P_t or deformation, δ_t must be applied in order to cause separation. Since the adhesive is much more compliant than the punch and the substrate, the deformation is confined within the adhesive layer. The average strain, ε is approximately,

$$\varepsilon_t = \frac{\delta_t}{a} \tag{1.16}$$

and the tensile load is:

$$P_t \approx \pi a^2 E \varepsilon \approx \pi a E \delta_t \tag{1.17}$$

The mechanical strain energy, U_{def} is defined as the total energy required to form and separate the interface. U_{def} is represented by the integral of the load-displacement curve.

$$U_{def} = \int P_t \cdot d\delta_t \approx \frac{P_t^2}{2\pi a E} \tag{1.18}$$

Separation occurs when the mechanical strain energy reaches a critical separation load or displacement, i.e. when the critical adhesion energy is reached ($U_{adh}=\pi a^2 G_c$), which leads to the following relationship at separation:

$$\frac{G_c}{E} \approx \frac{1}{2} a \varepsilon^2 \tag{1.18}$$

Through this simple energy balance approach, Shull is able to show that adhesive interactions become important when the length scale of an interface, a, is commensurate with a critical material-defined length scale a^* defined by the ratio of G_c/E.

Crosby and coworkers have used similar approaches to relate pattern length scales to adhesion and demonstrate experimentally how the presence of low-aspect ratio posts can tune the adhesion for a crosslinked PDMS-glass interface.[4] They explain the role of post dimensions in controlling adhesion as the interfacial contact geometry between the PDMS post and glass probe changes as the post radius is varied. By simultaneously varying the post radius and post density, they are able to tune the maximum tensile force at separation, $P_{max,t}$ and W_{adh} from 20% to 400% relative to a smooth PDMS interface (Fig. 1.9).

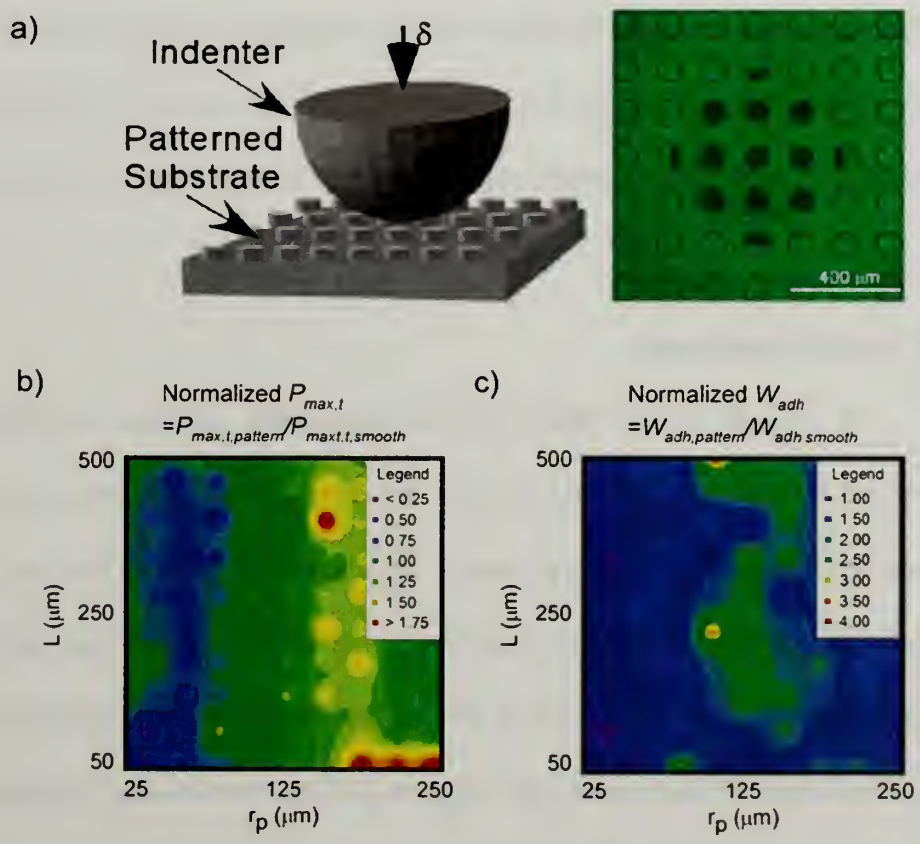

Figure 1.9 – Adhesion of low-aspect ratio post structures. Contour maps of the adhesion descriptors as a function of post spacing, L and post radius, r_p of b) normalized $P_{max,t}$ and c) normalized W_{adh}, both descriptors are normalized relative to a smooth PDMS interface. Figure reproduced from Crosby *et al.*[4]

Similar to the scaling relationship presented by Shull, Crosby and co-workers define a critical post radius related to the ratio of G_c/E, upon which the contact geometry changes from a stable interface (whereby additional energy must be supplied to propagate the crack) to an unstable interface (where the adhesive has sufficient stored elastic energy to drive the crack forward) and the interfacial contact separates abruptly.

As we have discussed above, there are many contributions to the enhanced control of adhesion. As such, we emphasize our research mainly in understanding the how interfacial contact geometry, such as contact line, plays a critical role. In addressing this aspect, our main goal for this research is to identify the relevant length-scales in the design of patterned adhesives. Specifically, what are relationships between materials' properties and pattern length scales that control polymer adhesion?

1.6 Thesis Organization

In Chapter 2, we show that non-topographic patterns, specifically, surface-chemical patterns can be used to tailor the adhesion of a commercial silicone-based elastomer. The surface-chemical patterns are characterized by an interface consisting of a periodic variation in surface chemistry – i.e. a covalent and non-covalent bonding with the elastomer. We demonstrate that the primary mechanism of control is associated with the control of the contact line, as opposed to the contact area, during separation.

In Chapter 3, we focus on developing a new approach to patterning polymer surfaces based on surface wrinkling. Compared with highly-defined patterns prepared with photolithography, a wrinkle surface is characterized as a surface with a Gaussian distribution of pattern dimensions. As we demonstrate throughout Chapter 3, our

surface wrinkling approach allows for the patterning of large areas in a rapid and efficient manner without using photolithography. Our wrinkling approach is based on the swelling of a laterally confined elastomer. Hence, we take advantage of the polymers' propensity to swell in a favorable solvent to help drive wrinkle formation. This approach is unique as we are one of the few groups that rely on swelling and lateral confinement to drive wrinkle formation. Our understanding of the wrinkling process allows for the control of both the orientation and dimensions of the wrinkle patterns; furthermore, the control has lead to the discovery of two new wrinkling morphologies. An additional contribution is that we are able to directly generate functional devices with our wrinkled surfaces without further processing. Specifically, we illustrate that our wrinkled polymers can be used in applications such as optics or patterned adhesion. Chapter 3 focuses on designing optical devices based on the wrinkled polymers while Chapter 4 describes the design of wrinkles for patterned adhesives.

In Chapter 4, we fabricate an alternative patterned or "smart" adhesive that uses wrinkles as patterns to control adhesion. Again, we demonstrate the ease and efficiency in generating a "smart" adhesive based on surface wrinkling. More importantly, we are able to show enhanced control of adhesion provided by the geometry of the surface wrinkles. Similar to our understanding of adhesion control described in Chapter 2, both the mechanism of enhancement and control are based on changes in the contact line provided by the wrinkled interface.

CHAPTER TWO

ADHESION OF PATTERNED REACTIVE INTERFACES

2.1 Introduction

Nature has demonstrated that a powerful design strategy for tuning adhesion lies in the development of microscale-patterned structures at an interface.[6, 23] Inspired by these natural attachment systems (i.e. – gecko and jumping spider), researchers have adopted similar strategies in controlling polymer adhesion.[4, 5, 12, 14-16, 20, 24-26] In a majority of these systems, the structured polymer interfaces are topographically patterned with micro- and nano-scale surface post-like structures. Recent work by Crosby and co-workers has demonstrated that the post-like structures tune adhesion by controlling the stability of the interfacial separation event, which is defined by the lateral dimensions of the post, a.[4, 5] Adhesion is optimized when a approaches a critical length scale, a^*, which defines the change in the local mode of separation from initiation-driven to propagation-dominated. The length scale, a^* is a material-defined parameter that is related to the ratio of critical energy release rate, G_c and elastic modulus, E.

The material-defined length scale, a^*, is insightful in providing a practical guideline in pattern design as it suggests that the optimal pattern dimension is defined by the ratio of G_c/E. As the design criterion is defined solely by the local materials' properties, the types of structured surfaces are not limited to surface relief-type interfaces. For example, we can consider a surface-chemical pattern, which is a patterned surface defined by a periodic variation in surface chemical properties.

Surface-chemical patterns provide several benefits in controlling adhesion compared with topographic patterns. First, unlike post structures, issues associated with pattern collapse are avoided. In the example of the synthetic "gecko tape", the adhesive properties of the interface degrade as a result of "condensation" of the fibrillar structures.[14, 16, 25, 26] Over the course of multiple attachment-detachment cycles, the condensation process results in a decrease in adhesive strength. Second, as the patterns are chemical in nature, virtually no surface topology exists. Creating controlled surface topology requires molding or vertical deposition which is typically more process intensive than two-dimensional patterning. In instances where large variations in surface topography are undesirable or impractical to implement but adhesion control is still necessary, such as for tissue engineering, surface-patterns are ideal patterned interfaces for cell culture.[27, 28] Third, surface-chemical patterns can be optically transparent. With surface relief patterns, due to the scattering contrast of the micro-scale post structures, the textured surface becomes visually opaque. In applications where visual clarity is desired (i.e. windshields), surface-chemical patterns facilitate this requirement while still providing adhesion control.

While natural attachment devices such as the gecko and jumping spider rely remarkably well on topographic patterns that provide the benefits of reversibility (non-covalent interactions) and self-cleaning properties; these interactions cannot withstand the environmental conditions found in many applications. Examples include: 1) under the hood of an automobile, where resistance to extreme temperature variations, harsh solvents and mechanical stresses is critical to reliability or 2) as a surgical adhesive, where specific interactions are necessary to ensure good interfacial adhesion between

the adhesive and tissues. Hence, wet-dispensed adhesives (as opposed to PSAs) rely on irreversible chemical bonds for structural bonding and sealing. Since adhesives are typically applied as a macroscopic continuum relative to the length-scale represented by a^*, the effect of pattern density is not well established. The effect of coupling biologically inspired pattern control principles with irreversible, "industrial strength" synthetic interactions are unknown.

In this chapter, we explore the influence of surface-chemical patterns on the adhesion of soft, elastomeric interfaces in a peel geometry (Fig. 2.1). Specifically, the microscale patterns consist of periodic variations of two silanes interacting with a commercial silicone-based elastomer – a reactive silane that covalently bonds to the elastomer and an inert silane that is weakly adhered to the elastomer.

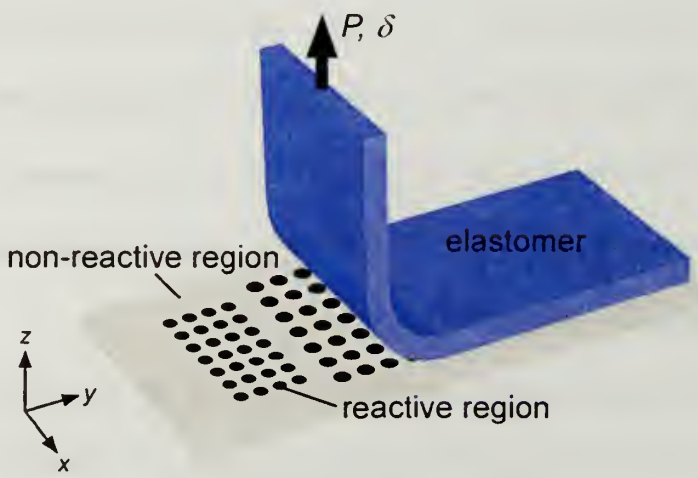

Figure 2.1 – Schematic of the peeling of the elastomer from the patterned-reactive interface.

To explore the interaction of chemical patterns with the soft elastomer, we focus on three types of pattern geometry with pattern dimensions on the micro-scale (circles, triangles and lines). We demonstrate that the reactive silane regions determine the

adhesive properties of the patterned interfaces. More importantly, the mechanism of adhesion is determined by the spatial distribution of the reactive silanes. In the following sections, we describe our experimental approach, an overview of the results, and a discussion of the mechanisms of adhesion for the surface-chemical patterned interfaces.

2.2 Experimental Approach

2.2.1 Pattern Fabrication

We prepare surface-chemical patterns on glass substrates using a combination of conventional UV photolithography and selective silane chemistry.[29, 30] Selective regions of the substrate are coated with 3-aminopropyl triethoxy silane (r-SAM). The amine is the reactive species that can form covalent bonds with the epoxide groups available in the epoxy-functionalized polydimethyl siloxane elastomer (e-PDMS). The remainder of the glass surface is coated with *n*-octyl trichloro silane (i-SAM) which is chemically inert with the elastomer. To explore the effects of pattern dimensions, we use a combinatorial approach where a single glass substrate consists of a library of 10 patterns of different dimensions (Fig. 2.2a). In addition, to explore the effects of pattern shapes, we prepare three types of pattern surfaces that include libraries of circles, triangles and lines (Fig. 2.2c, d, e). The dimensions for all the patterns explored in this work are summarized in Table 2.1.

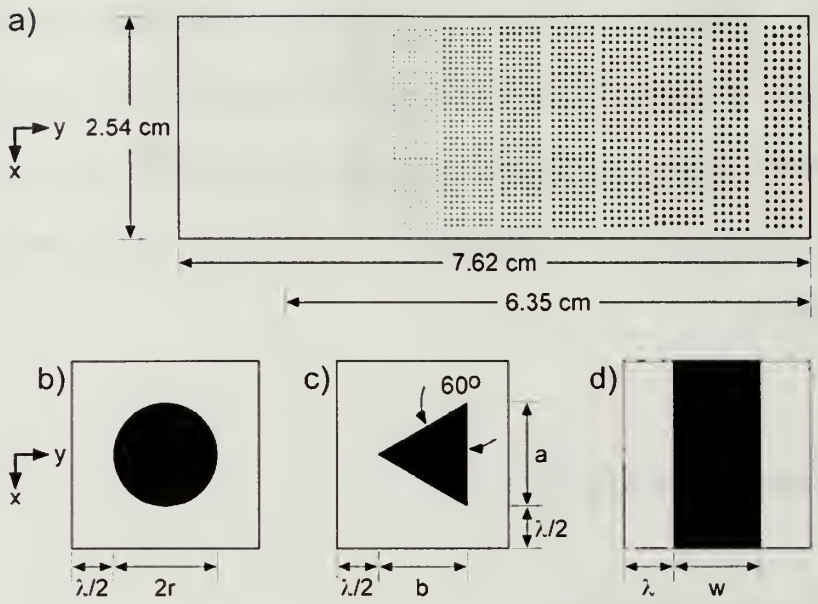

Figure 2.2 – Overall dimensions of a combinatorial library of patterns for a single peel sample. a) A single peel sample (consisting of a glass slide) consists of 10 separate pattern density (different pattern size but same spacing). The three different types of pattern shapes explored in this work include b) circles, c) triangles and d) lines. The *y*-direction represents the peel direction. The dimensions of the 3 patterns correspond to the values listed in Table 2.1.

Sample Name	C_1	C_2	C_3	T_1	T_2	L_1	L_2
Pattern geometry ■ = r-SAM □ = i-SAM	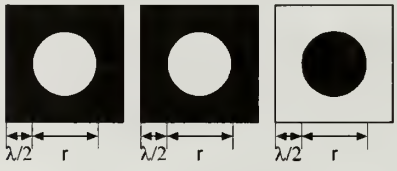						
Dimensions	λ (μm)			λ (μm)		λ (μm)	
	250	500	500	250	500	250	500
	r (μm)			b (μm)		w (μm)	
increasing r-SAM density ↓	250	250	25	1370	69	268	244
	225	225	50	1116	142	240	214
	200	200	75	907	219	212	184
	175	175	100	732	300	182	154
	150	150	125	582	386	153	124
	125	125	150	452	477	122	96
	100	100	175	338	574	92	69
	75	75	200	239	677	62	44
	50	50	225	150	786	34	22
	25	25	250	71	903	11	7

Table 2.1 – Summary of pattern shapes and dimensions explored.

The surface-chemical patterns are prepared by sequential vapor-phase deposition of two silane self-assembled monolayers (Gelest Inc., Morrisville, PA) onto a glass substrate prepared by conventional photolithography. The patterning procedure is summarized in Fig. 2.3. We begin by coating i-SAM onto a 7.6 cm by 2.5 cm glass substrate by vapor phase deposition (Fig. 2.3a-g). Next, a photoresist layer (Rohm & Hass SPR220, supplied by Microchem Corp., Newton, MA) is spun-coat over the entire i-SAM monolayer surface. The photoresist is patterned by UV exposure (OAI, λ = 365 nm, intensity = 20 MW/cm^2, OAI, San Jose, CA) through a photomask (Pageworks, Cambridge, MA) and then developed, which exposes the underlying i-SAM layer. Subsequent UV/Ozone oxidation chemically cleaves the exposed i-SAM regions.[29] Thorough rinsing with toluene removes the cleaved silanes as well as the photoresist layer. Next, r-SAM is patterned over the exposed glass substrate surface (Fig. 2.3h-i). Through vapor phase deposition, the r-SAM reacts with the exposed, bare glass surface and completes the surface-chemical patterning process to generate periodic regions of i-SAM and r-SAM. Finally, the surface is rinsed thoroughly with toluene to remove unreacted r-SAM silanes. The fidelity of the patterns is qualitatively evaluated by condensation of water onto the surface-chemical patterned surfaces and the patterned surfaces are used without further treatment.

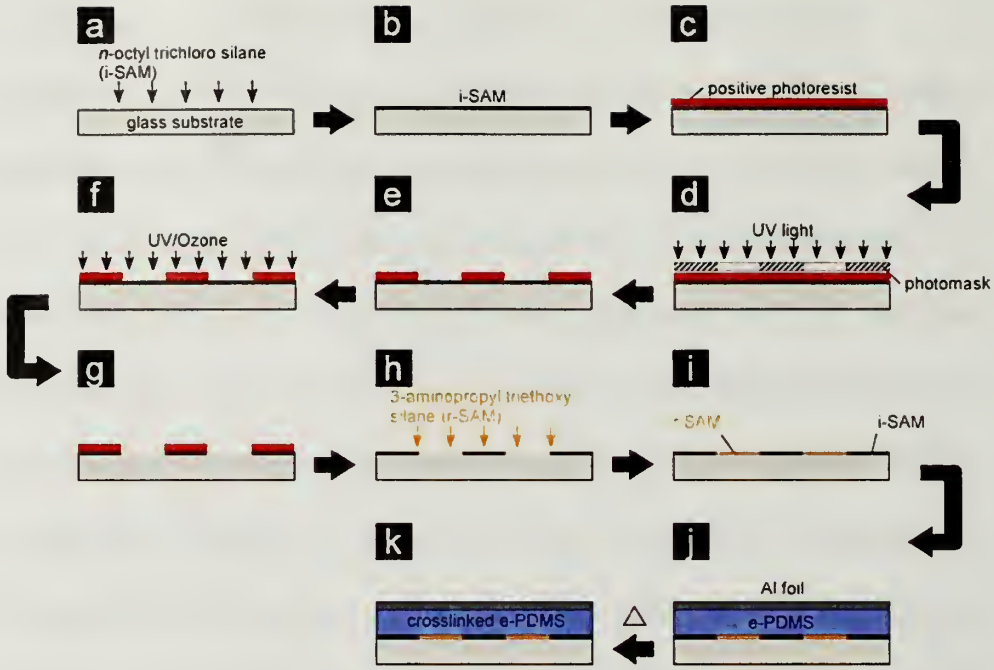

Figure 2.3 – Procedure for fabricating the surface-chemical patterns. a-b) The entire glass substrate is coated with *n*-octyl trichloro silane (i-SAM) by vapor phase deposition. c) The i-SAM surface is then covered by a spun-cast photoresist layer. d-e) Upon UV exposure through a photomask and subsequent development, selective regions of the i-SAM surface becomes exposed. f) UV/ozone treatment of the exposed i-SAM chemically cleaves the silane from the glass surface. g) Rinsing with toluene removes the cleaved i-SAM and the remaining resist layer. h) The bare glass regions is coated with 3-aminopropyl triethoxy silane (r-SAM) by vapor phase deposition. i) This yields the surface-chemical patterns of alternating i-SAM and r-SAM regions. j-k) Reaction and cross-linking of the epoxy-modified polydimethyl siloxane (e-PDMS). The e-PDMS mixture is poured over the patterns and then heat cured at 150°C for 30 min. Copper wire spacers are used to maintain the thickness of the elastomer. An aluminum foil backing layer is used to increase the stiffness of the elastomer.

2.2.2 Materials

We use films of e-PDMS elastomer as the model adhesive in our peel experiments. The e-PDMS (Dow Corning Corporation, Midland, MI) is prepared by mixing 65 wt % dimethylvinylsiloxy-terminated PDMS, 25 wt % vinyl functional (2 wt %) silicate resin, 0.2 wt % Karstedt's platinum catalyst complex dispersed in PDMS,

and 10 wt % telechelic PDMS oligmer multifunctional in silicon hydride groups that was prefunctionalized by partial substitution of the silicon hydride with epoxy groups.

To obtain the elastomer films for peel tests, the e-PDMS mixture is deposited onto the patterned surface and then doctored with a leveling blade to ensure uniform film thickness (thickness = 0.90 mm). A superstrate backing layer consisting of aluminum foil (thickness = 0.15 mm) is placed on top of the e-PDMS layer, while spacer blocks of copper wire are used to maintain the e-PDMS film thickness. The samples are then heated at 150°C for 30 min. The heating cycle cures the e-PDMS while at the same time allows for the chemical bonding of the epoxy groups of the e-PDMS with the r-SAM layer.

2.2.3 Adhesion Experiments

We measure the adhesion of the patterned interfaces using 90° peel tests. Prior to the test, the sides of elastomer are trimmed to obtain a center peel strip with a width of 2.2 cm. This trimming is intended to eliminate edge effects that arise due to the changes in stiffness as a result in changes in the film thickness near the edges of the film. The peel tests are conducted with an Instron tensile mechanical tester (MTS Sintech 5/G, MTS Systems Corporation, Eden Prairie, Minnesota). To begin the peel test, the glass substrate is secured onto a frictionless moving stage (MTS 90 Degree Peel Fixture). A short section of the aluminum-backed elastomer is bent backwards 90° and allows for the attachment to the upper grip of the mechanical tester. The peel angle is maintained throughout the test by a pulley system that ensures the moving stage moves in unison with the upper grip. The specimen is then separated by retracting the

upper grip at a constant crosshead velocity of 42 μm/s. The data collection rate is approximately 1 data point/s, which is sufficient to observe the pattern interaction with the elastomer.

Representative load, P – displacement, δ curves for the non-patterned and patterned peel tests experimens are illustrated in Fig. 2.4 and 2.5, respectively. Following the initial sudden increase in peel force due to the initiation of a crack, the peel force reaches a steady-state value that is associated with the propagation of the crack. We quantify an average peel force, P_m by averaging the steady-state values over the entire crack propagation period. For the nonpatterned peel data, the entire surface consists of a homogenous coverage of r-SAM layer; therefore, the steady-state peel force remains constant. Post inspection of the glass substrate reveals a thin layer of the elastomer remains on the surface suggesting that the separation process occurs through the cohesive fracture of the elastomer near the silane-elastomer interface. Similarly, for the patterned surface, we observe cohesive fracture of the elastomer in the r-SAM regions while the i-SAM regions failed adhesively. From these results, along with knowledge of the geometry of the elastomer, we can quantify a lower limit of the critical energy release rate, G_c of the interface. In the peel test geometry, G_c is related to the peel force, the adhesive width, w and the peel angle, θ by the Kaelble equation.[31] Here, we go through the derivation of this peel equation.

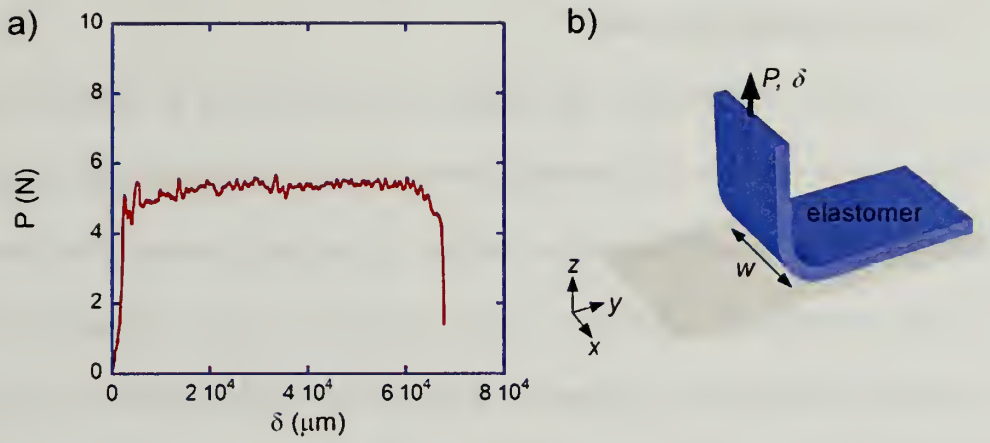

Figure 2.4 – Result of the peel test. a) The force, P vs. displacement, δ curve of a homogeneous surface of 3-amino triethoxypropyl silane (r-SAM). The average peel force P_m is quantified by averaging the steady-state values over the entire crack propagation period. b) This average peel force is the product of the critical adhesion energy, G_c and the contact line, w as defined by the Kaelble equation.[31]

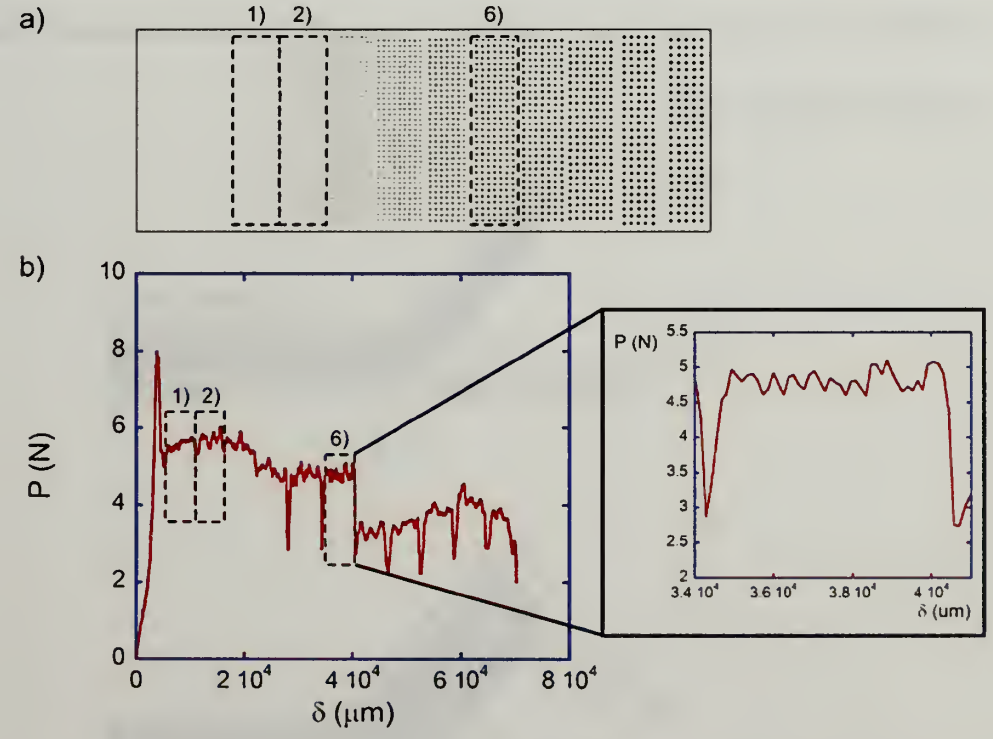

Figure 2.5 – Results of a combinatorial library. a) Each cell within the library is a separate peel test. b) The force vs. displacement curve of a representative library. The result for each test cell is easily distinguished. The inset highlights the response for a single pattern density. The non-patterned region that separates the patterned surfaces is identified by the sharp decrease in force.

2.2.4 The Kaelble Equation[31]

Figure 2.6 illustrates the general peel geometry of an adhesive peeling away from a rigid substrate. As described previously, the purpose of the test is to measure the strength of the adhesive-substrate interface by applying a tensile force on the adhesive to cause separation. However, during separation of the deformable adhesive, the compliance of the layer continually increases since more and more of the adhesive is deformed by uniaxial extension. As a result, this separation force is not a true measure of the interfacial strength, but rather, a convolution of the bulk deformation of the adhesive along with the interfacial deformation, i.e. the interfacial strength. To minimize the bulk deformation of the adhesive, a rigid backing layer is typically adhered to the top of the adhesive and this composite layer is deformed in unison during the peel test (Fig. 2.6a).

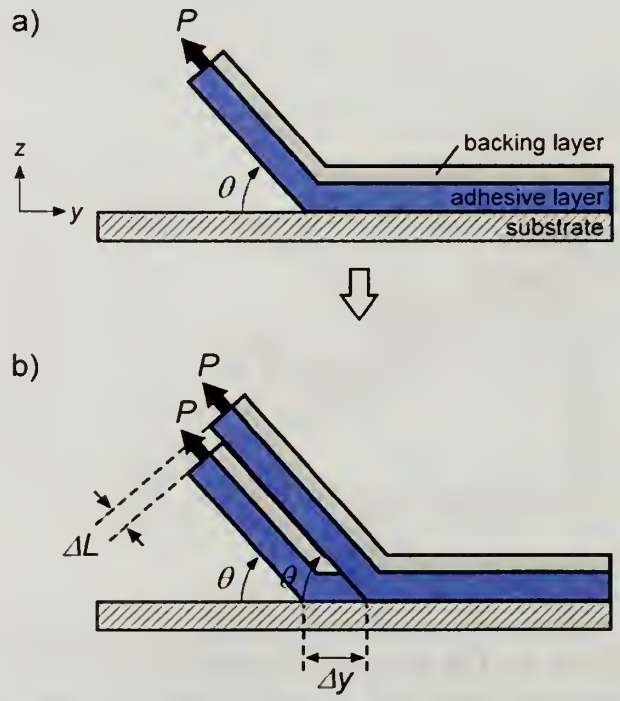

Figure 2.6 – Schematic of the peel geometry used to derive the Kaelble equation.[31]

The Kaelble equation is derived specifically for this geometry by determining the energy required to separate the adhesive from the substrate (Fig. 2.6b).[31] To peel the adhesive by a given displacement, Δy, the applied peel force and deformation are P and ΔL, respectively. The total energy of deformation, U is defined as:

$$U = P \cdot \Delta L \tag{2.1}$$

The extension of the adhesive, ΔL is related to the displacement by:

$$\Delta L = (1 - \cos\theta) \cdot \Delta y \tag{2.2}$$

Substituting Eqn. (2.2) into (2.1), we obtain the following result:

$$U = P \cdot (1 - \cos\theta) \cdot \Delta y \tag{2.3}$$

From the definition of critical adhesion energy, G_c is determined by the incremental amount of energy, dU required to advanced a crack an incremental unit area, dA, in other words:

$$G_c = \left.\frac{dU}{dA}\right|_P = \frac{1}{w}\left.\frac{dU}{d\Delta y}\right|_P \tag{2.4}$$

The incremental area change, dA is defined as:

$$dA = w \cdot d\Delta y \tag{2.5}$$

where w is the width of the adhesive. Therefore, G_c is determined by evaluating Eqn. (2.3) using (2.4), which gives us the Kaelble equation:[31]

$$\begin{aligned} G_c &= \frac{1}{w}\frac{d}{d\Delta y}\left(P \cdot (1 - \cos\theta) \cdot \Delta y\right) \\ &= \frac{P}{w} \cdot (1 - \cos\theta) \end{aligned} \tag{2.6}$$

The Kaelble equation allows us to easily relate the geometry of the test (peel angle, θ and width of the adhesive, w) and peel force, P to the materials' property of the adhesive (critical adhesion energy, G_c).

2.2.5 The Normal Stress

The critical question we need to first address is the validity of the Kaelble equation and more importantly, the peel test in quantifying the adhesion for our surface-chemical patterns. Therefore, we need to first identify what the peel force of the test is measuring – i.e. is the peel force a direct measure of the interfacial strength directly at the crack front or ahead of the crack due to the complex state of stress distribution of the test.

Irrespective of the peel angle, there is a combination of normal and shear stresses that develop within the adhesive layer during debonding. As a consequence, the measured peel force, P is a combination from these two contributions. During a peel experiment, we are essentially applying a bending moment to the adhesive-backing composite layer. Hence, the normal and shear stresses experienced by the adhesive can be determined by applying the condition of local equilibrium to summing up the forces and bending moments of the deformed element. For a detailed analysis of the normal and shear stress functions, we refer the reader to the original work of Kaelble.[11] Here, we simply provide the final result to show how the normal stress distributes at and near the deformed region, i.e. near the crack tip. The final normal stress function is:

$$\sigma = \sigma_o e^{\beta y} \cdot \left(\cos \beta y + K \sin \beta y\right) \tag{2.7}$$

where K is essentially a contant related to the peel angle and the stress concentration factor, β is related to the materials' properties and geometry (the thickness of the adhesive and backing layers, $t_{adhesive}$ and $t_{backing}$, respectively) for the adhesive and backing layers:

$$\beta = \left(3 \frac{E_{adhesive}}{E_{backing}} \frac{1}{t_{adhesive} t_{backing} w^2} \right)^{1/4} \tag{2.8}$$

For a 90° peel, $K = 1$, based on the dimensions and approximate Young's modulus of the backing and adhesive layers (w = 2.2 cm, $t_{backing} \approx 0.15$ mm, $E_{backing} \approx 70$ GPa and $t_{backing} \approx 0.9$ mm , $E_{adhesive} \approx 1.5$ MPa), we determine $\beta \approx 0.31$ m^{-1}. The normal stress distribution for our material is presented in Fig. 2.7.

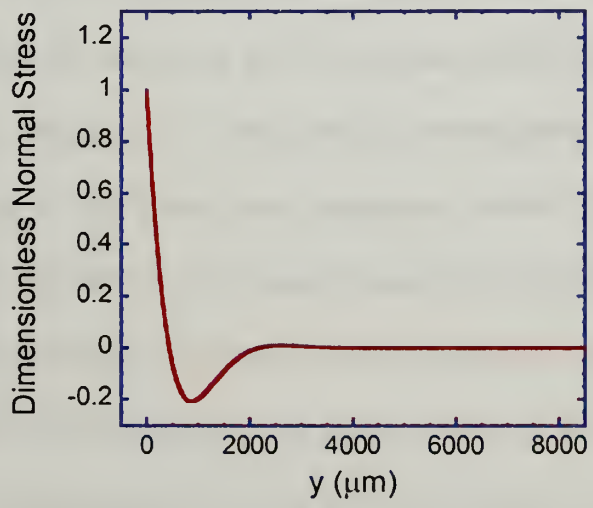

Figure 2.7 – The theoretical normal stress distribution of our elastomer during a 90° peel. The plot illustrates that the tensile stress ("+" stress value) is confined primarily at the crack tip (y=0).

The plot demonstrates that due to the bending of the adhesive layer, there is a region of compression ("-" normal stress) immediately ahead of the crack front (where we have set y=0 to be the crack tip). Additionally, this compression region is dependent on the

peel angle (as reflected by K) as well as the materials constants of layer dimensions and elastic modulus (as reflected by β). To concentrate the deformation at the crack tip, the value of β should be maximized. One strategy to maximize β is to decrease the flexural stiffness of the backing layer; by reducing the thickness of the layer and/or its elastic modulus. However, the main purpose of the plot is to demonstrate that the tensile forces is primarily confined at the crack tip and that the peel force is directly measuring the amount of energy required for separation between the adhesive and the substrate.

2.2.6 The Kaelble Equation[31] for 90° Peel

For our peel geometry ($\theta = 90^{\circ}$), G_c reduces to P/w. As G_c is a materials-defined parameter and therefore; independent of interfacial contact, the descriptor is especially insightful in quantifying adhesion for all the surface-chemical patterns explored in this work. For the homogeneous i-SAM surface, we are unable to quantify the peel force as we consistently obtain an average force value that is below the resolution of the instrument. Therefore, the upper-bound for G_c for the i-SAM interface is defined as the resolution of our instrument: 4.5 J/m^2. For the r-SAM interface, we measure G_c equal to 242.0 J/m^2. This is a lower bound since cohesive failure in the e-PDMS is observed visually. These values of G_c, along with the elastic modulus of e-PDMS, $E^* \sim 1.5$ MPa, define the material length-scales, $a^* = G_c/E$, that are approximately 0.2 mm for the r-SAM interface and 5.0 μm for the i-SAM. Accordingly, our pattern dimensions (Table 2.1) are designed to be commensurate with these material length scales. Furthermore, our film thickness is sufficiently thick such that the dissipation process is confined to the interface of the elastomer and chemical pattern surface.

To quantify adhesion for the combinatorial library of surface-chemical patterns, we define a discrete value of P_m by averaging the steady-state peel force over the length of the specific pattern for each pattern within the combinatorial library. In addition to P_m, we use the materials-defined adhesion descriptor G_c to elucidate the effects of surface density of the r-SAM species.

2.3 Results

The adhesion of binary-silane interfaces has been studied previously.[32, 33] However, the previously explored binary-silane interfaces are non-patterned surfaces that consist of random distribution of silane groups. Hence, the role of periodic surface chemistry on adhesion remains unexplored. In this work, the surface-chemical patterns represent model systems to study the impact of periodic variation in interfacial bond strength on the overall adhesive properties. To compare the pattern surfaces, we evaluate the patterns independent of the pattern shapes and dimensions by quantifying the surface density of chemically bonded r-SAM species. In relating P_m to r-SAM surface density, the line fraction is the appropriate parameter since the peel force is directly proportional to the width of the adhesive. We can define the line fraction by considering the pattern as an array of unit cells, each cell consisting of a single pattern feature (Fig. 2.8). The line fraction is defined as the ratio of the local line width of the r-SAM region, $w(y)$ versus the total width of the unit cell, W. Therefore, the average line fraction of the r-SAM region, f_r is defined by integration along L of the local line fraction, $w(y)/W$ and then normalizing by L. The integration limit, L, is defined by the y-

axis limit of the unit cell. The average line fraction, f_r as defined by Eqn. 2.9 is equivalent to area fraction, ϕ_r of the pattern. The average peel force results for the peel tests are presented in Fig. 2.9.

$$f_r = \frac{\int_0^L \frac{w(y)\cdot dy}{W}}{\int_0^L dy} \tag{2.9}$$

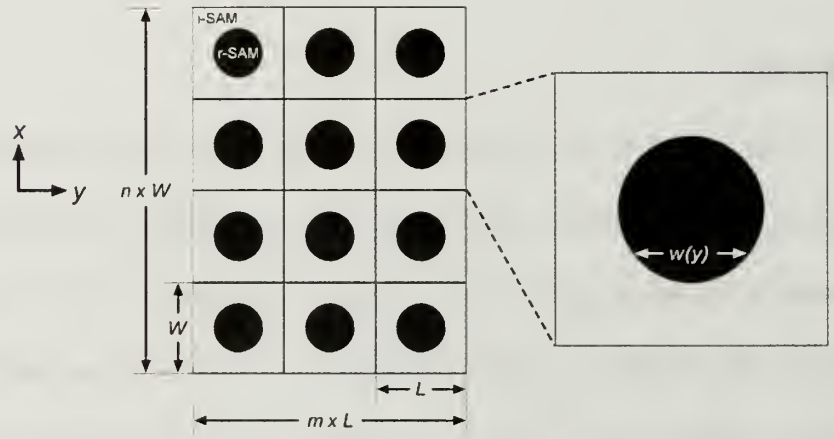

Figure 2.8 – Example of a pattern surface consisting of circular patches of r-SAM in a matrix of i-SAM. The pattern consists of *n* rows and *m* columns of unit cells of dimensions *W* x *L*. If we consider the peel direction along the *y*-axis, the line fraction is defined as *w(y)/w*.

Given our material system and the patterns explored, we are able to tune P_m from 20% to 115% compared with P_m for the non-patterned r-SAM surface. While these results demonstrate the tuning of adhesion with well-defined patterns of surface-chemistry, they also suggest that all three classes of patterns respond differently – i.e. mechanisms beyond the straightforward contribution of surface density of the reactive silane.

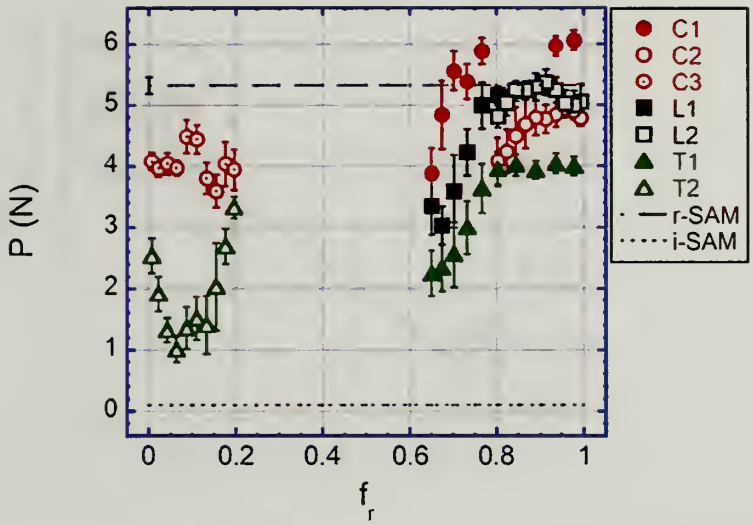

Figure 2.9 - Plot summarizing the peel test results for all the materials explored. Each set of symbols (i.e. C2) represents a combinatorial library consisting of 10 test patterns with the same pattern shape but different pattern dimensions as evidenced by the variation in average line fraction, f_r. The plot summarizes P_m as a function of f_r for all the surface-chemical patterns. To identify the effects of surface coverage on adhesion, we evaluate the patterns in terms of an average line fraction of r-SAM. As a comparison, P_m for the nonpatterned reactive (r-SAM) and inert (i-SAM) silane surfaces are also presented. As we are unable to quantify P_m for the i-SAM surface, we estimate the value as the lower resolution of the peel test instrument which is ~0.1 N.

In order to identify a universal behavior, we use G_c to quantify the adhesion for all the pattern surfaces as a function of area fraction of the reactive regions. Fig. 2.10 summarizes these results in terms of normalized G_c, where the energy release rate values are normalized by the values for the non-patterned r-SAM interface ($G_{c,pattern}/G_{c,r\text{-}SAM}$).

The results demonstrate that the response is not universal for all the patterns and suggest that the adhesion is not a consequence of the changes in the surface density, ϕ_r (or in our case, this area fraction, ϕ_r, is equivalent to the average line fraction, f_r). As we discuss in the following section, pattern geometry plays a significant role in controlling adhesion and can be used as an effective parameter in interfacial design.

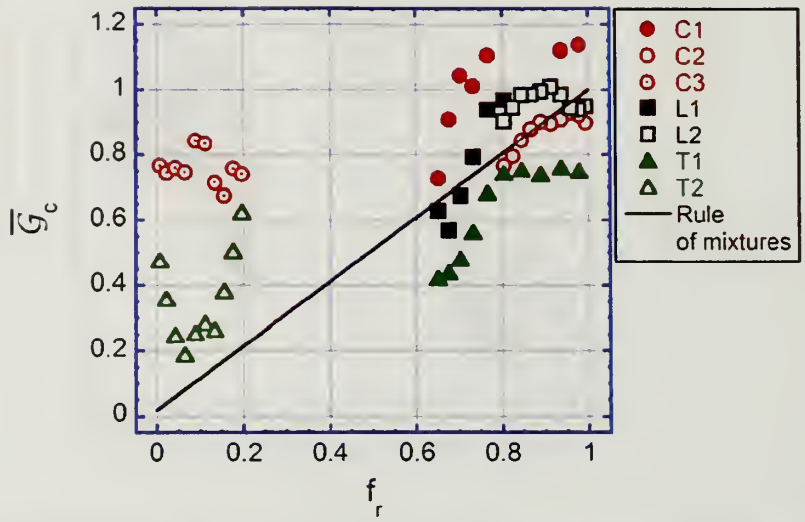

Figure 2.10 – Plot of adhesion energy, G_c versus line fraction, f_r. The adhesion energy is normalized by the adhesion energy of the r-SAM, G_c. The solid curve represents the prediction of Eqn. (2.12) where we assume G_c scales with the area fraction of the r-SAM and i-SAM.

2.4 Discussion

2.4.1 An "Effective" G_c

If regions in a patterned interface obeyed a simple rule of mixtures, the total peel force, P_m can be simply defined as the sum of the individual contributions from the r-SAM, P_r and i-SAM, P_i regions.

$$P_m = P_r + P_i \tag{2.10}$$

Based on Eqn. 2.6, we can use the measured energy release rates for the r-SAM, G_r and i-SAM, G_i surfaces and the known average line widths for these respective regions, w_r and w_i to yield the following expression for the effective G_c for the patterned interface:

$$G_c = \frac{P_m}{w} = \frac{w_r G_r + w_i G_i}{w} \tag{2.11}$$

Defining w_r/w as the average line fraction (Eqn. (2.9)) and normalizing by G_r, we obtain the normalized energy release rate for a binary surface chemical pattern.

$$\overline{G}_c = \frac{G_i}{G_r} + \left(1 - \frac{G_i}{G_r}\right) \cdot f_r \tag{2.12}$$

Eqn. 2.12 predicts that an increase in the average line fraction of the reactive silane simply leads to a proportional enhancement in the adhesion energy. In essence, this equation is insensitive to pattern geometry as it considers the surface as a non-specified distribution of r-SAM and i-SAM silane groups with the response from neighboring regions being uncoupled. Therefore, any deviation of adhesion energy from the prediction by Eqn. 2.12 implies that the pattern geometry play an important role in tuning adhesion.

Based on the results shown in Fig. 2.10, almost all the patterns demonstrate an enhancement in adhesion compared with the rule of mixture prediction. More importantly, the adhesion is maximized well below maximum f_r (= 1). With the circular patterns of C1, reaches unity at $f_r \sim 0.7$. In fact, the maximum adhesion energy for this pattern library is approximately 115% greater compared with a smooth, non-patterned reactive interface. Other patterns demonstrate similar optimization of adhesion energy well below maximum line fraction; however, the circular patterns provide the greatest enhancement. In the following sections, we describe the two possible contributions to enhancement and also identify the primary mechanism of enhancement.

2.4.2 Control of Adhesion by Viscoelastic Rate Effects

One possible mechanism of adhesion is the tuning of adhesion by changing the local separation rate of the interface. Viscoelastic systems offer additional adhesion

mechanisms compared with their elastic counterparts in that their adhesive properties are history and rate dependent. As most polymers demonstrate some degree of viscoelastic behavior, the tuning of adhesion by changes in the rate-response must always be considered.

During separation, a crack of length, a develops at the adhesive-substrate interface. The rate at which a changes with time, t defines the crack velocity ($v=da/dt$). For polymer adhesives that demonstrate near-interfacial (i.e. at or near the crack tip) viscoelastic behavior, the critical adhesion energy, G_c is sensitive to the crack velocity. Empirically, G_c scales with v by the following relationship (assuming that the region of deformation is confined near the crack tip, i.e. – ignoring bulk contributions):

$$G_c = G_o \cdot \left(1 + \left(\frac{v}{v^*}\right)^n\right) \tag{2.13}$$

where v^* is the characteristic crack velocity related to the viscoelastic properties of the adhesive and n for polymers is ~0.6. Examples of this rate-dependent response are demonstrated for acrylate-based elastomers as shown in Fig. 2.11.

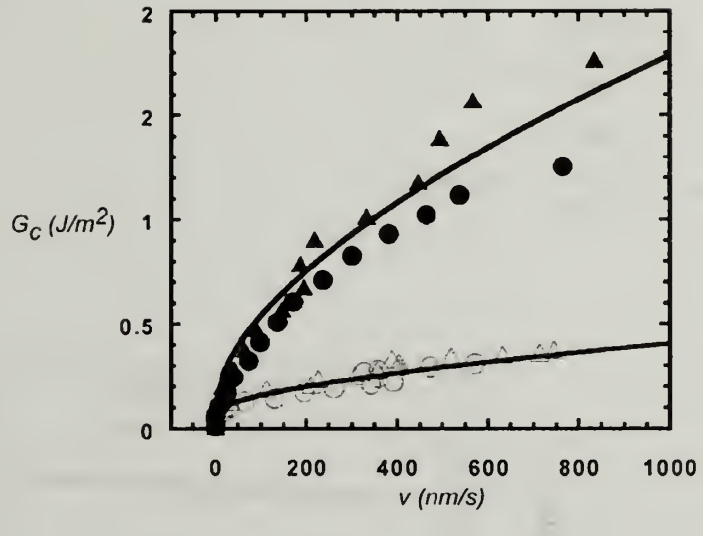

Figure 2.11 – Critical adhesion energy vs. crack velocity for P*n*BA elastomers separating from different polymer interfaces. Figure reproduced from Shull.[22]

To determine the rate-dependent mechanical properties of our e-PDMS elastomer, we measure the material's mechanical response using dynamic mechanical analysis over the frequency, ω range of 0.01 to 10 Hz (Fig. 2.12). This frequency range is chosen as it corresponds to the testing rates between the elastomer and the surface patterns. Specifically, ω can be estimated by relating the crack velocity (assumed to be equivalent to the cross-head velocity) to the dimension of the surface chemical patterns (Table. 2.1).

$$\omega_{max} = \frac{\text{testing velocity}}{\text{pattern length scale}} \tag{2.14}$$

Based on the smallest and largest pattern dimensions, we estimate the maximum, ω_{max} and minimum, ω_{min} testing frequencies to be:

$$\omega_{max} = \frac{42\,\mu m/s}{7\,\mu m} = 6\,Hz$$

$$\omega_{min} = \frac{42\,\mu m/s}{1370\,\mu m} = 0.03\,Hz$$

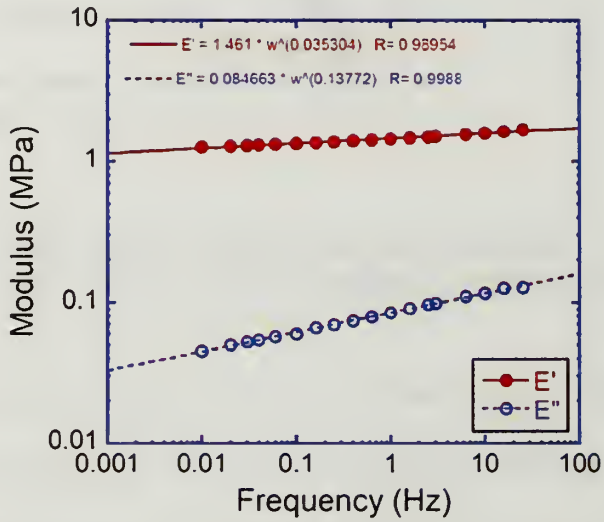

Figure 2.12 – Dynamic mechanical analysis (DMA) of the e-PDMS. The result shows that with the test frequency from 0.01 to 10 Hz, the material behaves elastically.

Based on the DMA test within the frequency range of 0.01 to 10 Hz, we measure the storage modulus, $E' \sim \omega^{0.04}$ and the loss modulus, $E'' \sim \omega^{0.14}$. We can make two comments based on this result. First, since the storage modulus is an order of magnitude greater than the loss modulus, the mechanical response behaves predominatly in an elasic manner within this frequency range. Second, both the storage and loss modulus show a weak rate dependence, hence, the rate-dependent change in mechanical properties is negligible. Therefore, the DMA results demonstrate that rate-dependent change in adhesion is not a plausible mechanism of enhancement.

2.4.3 Control of Adhesion by Contact Line Resistance

With the exception of the triangular pattern library of T1, all pattern libraries demonstrate an enhancement in adhesion energy relative to the prediction of Eqn. (2.12). This enhancement is related to the lengthening of the contact line due to contact line pinning. With a homogeneous non-patterned interface, the contact line is equivalent to the width of the adhesive. By incorporating periodic regions of surface chemical contrast, the contact line profile increases as a function of the surface chemistry contrast and the perimeter of the pattern region. To understand this mechanism for the pattern libraries of C3 and T2, we consider these surfaces as homogeneous i-SAM surfaces with the r-SAM species occupying discrete regions of the interface. As illustrated in Fig. 2.13, the separation process can be described as the opening of a crack, where the contact line defines the crack front during the peel experiment. Prior to interacting with the discrete patterns, the width of the contact line corresponds to the width of the adhesive (Fig. 2.13a-i, 2.13b-i).

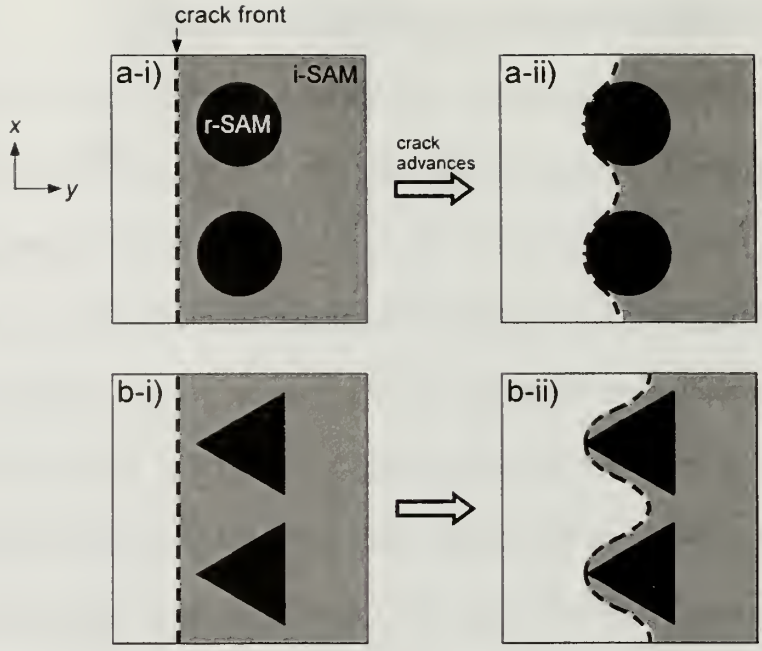

Figure 2.13 – Illustration of the contact line resistance for the discrete r-SAM patterns of C3 and T2. As the crack front advances, the contact line becomes "pinned" by the discrete r-SAM triangular regions. As a result, additional energy must be supplied in order to drive the crack forward which leads to an increase in adhesion energy for the interfaces. The grey shaded area is the interface that remains in intimate contact.

Once the crack front approaches discrete r-SAM patterns, the presence of the r-SAM regions "pins" the contact line (Figure 2.13a-ii, 2.13b-ii). This leads to the deformed, lengthened profile of the contact line, which increases the resistance for the crack to propagate. As a result, additional energy must be supplied to drive the crack forward. The enhancement is more significant for C3 compared with T2, which we believe is associated with the stress concentrating geometry presented by the aligned triangles. In other words, the circular geometry blunts the contact line more effectively compared to the triangular patterns. Hence, a r-SAM circular geometry (with the same area as the triangle) should provide greater efficacy in pinning the contact line compared to the r-SAM triangular geometry. This mechanism is analogous to the Cook-

Gordon mechanism of crack blunting in laminate composite materials.[34] A similar mechanism of adhesion enhancement has been previously observed by Chung and Chaudhury for topographically patterned adhesives.[13] Since the crack is forced to deflect laterally, additional energy must be applied in order to "re-initiate" the separation process. As this mechanism exists for all the patterns, we observe an enhancement in adhesion for our materials. Although our results show a modest enhancement, based on the results by Chung and Chaudhury,[13] we expect more enhancement can be achieved with an optimized geometry for the patterned interface.

Similar mechanism of contact line pinning is demonstrated for the remaining patterns of C1, C2, L1, L2 and T1. For these systems, the homogeneous phase of the interface is the reactive r-SAM and patterned with discrete non-reactive i-SAM. Once again, the presence of the r-SAM matrix effectively "pins" the contact line, which leads to an enhancement of adhesion (Fig. 2.14). The exception is the triangular pattern T1. The adhesion energies for all the patterns within this library fall below the values predicted by Eqn. (2.12). We explain this decrease in the T1 patterns by comparing the crack propagation process between the circular (C1 or C2) and triangular patterns (T1) (Figure 2.14). Prior to the approaching the i-SAM patterns as defined by point A, the crack fronts for both patterns are identical (Fig. 2.14a-ii, 2.14b-ii). Upon interacting with the i-SAM patterns, the contact line widens due to the previously described "pinning" effect. Similar to the r-SAM patterns, this mechanism of adhesion should persist through the entire i-SAM patterns. However, unique to the i-SAM patterns is the control of the contact line stability as crack front interacts with the pattern region (from point A to B).

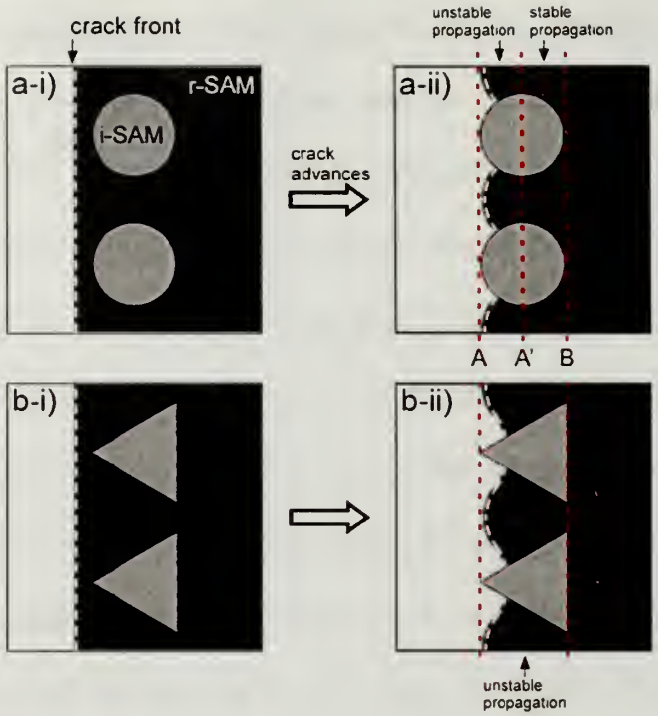

Figure 2.14 - Illustration of contact line resistance for the discrete i-SAM patterns. Again, prior to interaction with the i-SAM pattern, the contact line is linear. However, upon interaction with the pattern, the contact line becomes sinusoidal as it is pinned by the r-SAM matrix regions. a-ii) For the circles of i-SAM, the crack propagates initially in an unstable manner from path A to A' since the interfacial contact of the r-SAM regions is continually decreasing. However, from path A' to B, the interfacial contact of the r-SAM gradually increases which leads to the crack to propagate in a stable manner. b-ii) For the triangular pattern, the interfacial contact continues to decrease for the entire path from A to B. Therefore, the crack self propagates in an unstable manner within this entire region.

Specifically, the r-SAM region between adjacent i-SAM patterns defines the contact line stability. For the triangular pattern, as the crack front travels from A to B, the interfacial width of the r-SAM region, i.e. the stronger interface, continues to decrease. Hence, an excess of elastic energy is available for the propagation of the crack. From a fracture mechanics standpoint, this crack separation process is defined as an unstable propagation since $dG/d\delta \leq 0$. Similarly, the i-SAM circular pattern gives

rise to the same mechanism of unstable crack propagation during the points A to A'. However, as the crack travels from A' to B, the interfacial area of the r-SAM region increases for the circular patterns; therefore, additional energy must be supplied in order to maintain the propagation of the crack. This region is defined as a stable crack propagation region since $dG/d\delta \geq 0$. Therefore, the primary distinction between the two patterns in tuning adhesion is attributed to the symmetry of the shapes. Due to the orientation and symmetry of the triangular pattern with the crack propagation direction, the crack propagation is always unstable; whereas with the circular patterns, the sequence of unstable-stable crack propagation persists locally with every circular pattern. However, regardless of the pattern symmetry, our results illustrate the importance of defining the contact line in tuning adhesion, which has been shown by several research groups to be an important parameter in controlling interfacial separation.[5, 10] The distinction with our materials systems is that we demonstrate similar mechanism of enhancement with surface chemical patterns as opposed to surface relief patterns. Finally, the plateau in G_c for high f_r is attributed to the loss of efficiency of the pattern to lengthen the contact line. For our patterns, since we maintain the same feature spacing, the number density of the features decreases as the feature size increases (i.e. as f_r increases). Hence, the contact line does not increase significantly at high f_r.

2.5 Summary

In this work, we have demonstrated the impact of patterned reactive sites on controlling adhesion and provide simple examples of how the distribution of reactive groups can greatly influence the development of interfacial strength. The lessons learned offer many exciting avenues to develop design guidelines for optimizing interfacial strength. Specifically, we demonstrate the role of surface-chemical patterns in tuning the adhesion of soft elastomers. The results of the adhesion tests illustrate the importance of pattern length-scale – i.e. pattern dimensions commensurate with material defined length scale of G_c/E, play an important role in tuning adhesion. In all of our material systems and patterned surfaces, the changes in adhesion with f_r cannot be simply described as a random mixture of reactive-nonreactive silanes. Rather, the control of adhesion is connected with the spatial distribution of the reactive silane regions. We observe an enhancement in adhesion in almost all the pattern surfaces. The mechanism of enhancement is associated with the increase in the contact line during separation. Due to the presence of the reactive surfaces, the contact line becomes "pinned" in the r-SAM regions. As a result, additional energy must be supplied in order to continue propagating the crack. Another mechanism of adhesion that is present in the discrete i-SAM patterns involves the local control of crack propagation stability. Due to the continual decrease in the r-SAM interfacial area between adjacent i-SAM triangles, the crack propagates in an unstable manner as there is sufficient elastic energy to cause the crack to "self-propagate". Hence, this leads to a decrease in the adhesion energy for all the i-SAM triangular patterns. With the circular, or symmetric, patterns, we observe two stages of crack propagation, the crack initially propagates in an unstable manner

and then by stable crack propagation. We expect that the sequence of unstable to stable crack propagation observed in the circular pattern can be reproduced in the triangular pattern by generating a mirrored image of the pattern – i.e. diamond patterns. Although the e-PDMS material used for this study is essentially frequency independent at room temperature, the impact of viscoelastic contributions on the effect of patterned reactive interfaces is an interesting focus for future research.

2.6 Acknowledgements

We like to thank Dow Corning Corporation for financial support in the form of a one time donation. We are especially grateful to the following Dow Corning scientists: Dr. Shaun Ahn for initiating the project and assistance in design of experiment, Dr. K. A. Weir for helpful suggestions for surface chemical patterning and Dr. P. C. Van Dort for providing the e-PDMS.

CHAPTER THREE

PATTERN GENERATION BY SURFACE WRINKLING

3.1 Introduction

In the previous chapter, we have demonstrated that a properly designed surface-chemical pattern can tune the adhesion of a commercial elastomer. We used a combination of photolithography and sequential surface chemistry to fabricate the reactive patterns. While conventional photolithography can successfully transfer micro-scale patterns onto a polymer surface, this top-down approach is limited in the ability to pattern large surfaces as the photolithography can only pattern a limited area in a single exposure step. Additionally, this type of patterning is much too process intensive since it requires multiple steps. For our "smart" adhesive to be commercially viabile; the fabrication process has to demonstrate scaleability.

In this chapter, we explore an alternative patterning technique based on surface wrinkling that is a truly scalable and highly efficient process. The specific strategy to creating a "smart" adhesive is described in the next chapter. Here, we focus on understanding the mechanism of surface wrinkling and develping a robust approach to patterning a variety of polymers by surface wrinkling. This understanding enables the control of the surface wrinkle geometry, the pattern dimensions, their orientation as well as different wrinkling morphologies that includes two new morphologies that has not been observed previously.

3.1.1 Examples of Wrinkling

Surface buckling or wrinkling is a classical phenomenon that is observed in a variety of materials systems. We see wrinkles all around us in nature. Examples of natural wrinkles include wrinkles on the human skin (Fig. 3.1a), the folds and pleats of the brain as well as the Char-pei dog.

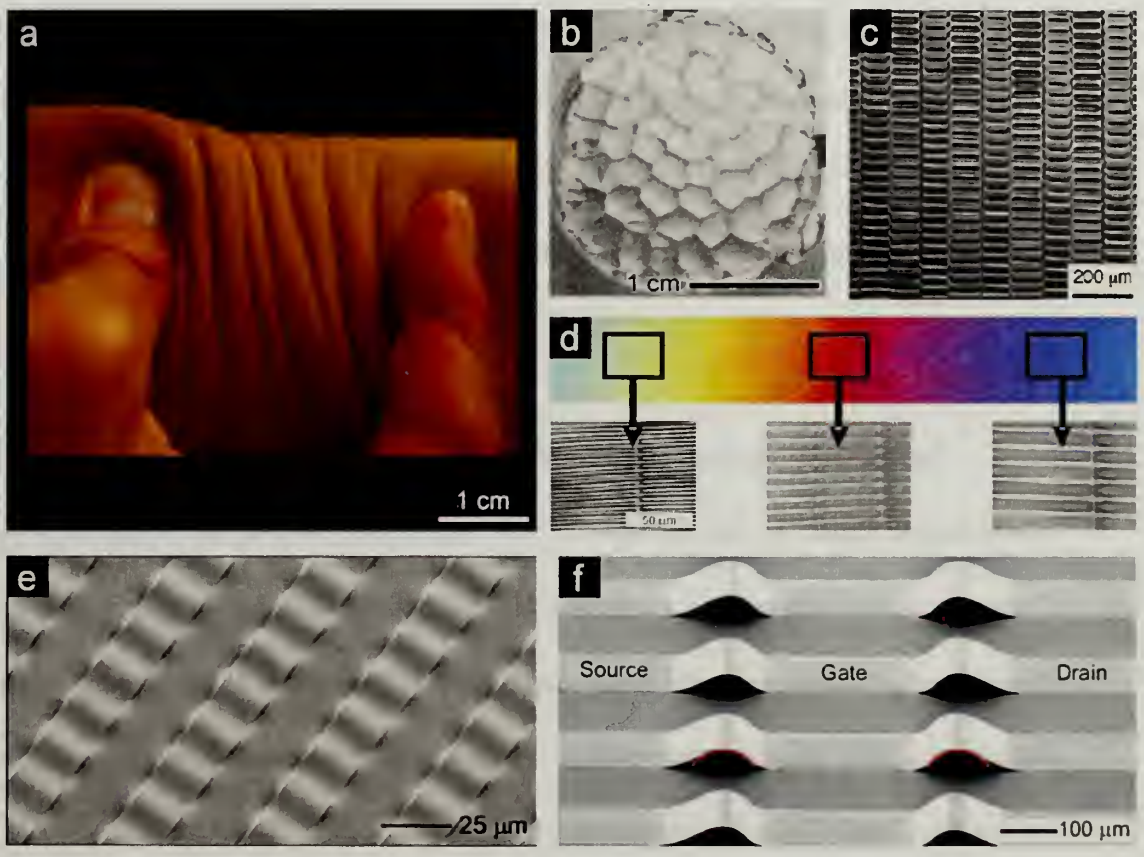

Figure 3.1 – Examples of surface wrinkles. a) Skin wrinkling, courtesy of EPC. b) Wrinkling of soft, polymer gel by swelling.[35] c) Wrinkling of gold thin film supported by a patterned elastomer, the driving force is by thermal expansion mismatch.[36] d) A wrinkling-based metrology used to measure the elastic modulus of thin film, in this case, a polystyrene thin film.[37] Flexible electronic devices made of wrinkled e) Silicon[38] and f) GaAs semiconductor strips[39].

Similarly, surface wrinkles can be generated in a variety of synthetic materials that include: 1) soft gels placed under geometric confinement that are swollen[35] or

dried[40] (Fig. 3.1b), 2) thermally or mechically stressed metallic[36, 41] (Fig. 3.1c, e & f), polymeric[37, 42] (Fig. 3.1d), and silicate[43, 44] thin films supported on elastomeric substrates, as well as 3) dried thin films prepared by sol-gel method.[45, 46] As we discuss in this chapter, since development of the pattern is dependent on the mechanical properties of the material and its stress state, the patterns can be quite complex and consist of a dominant periodicity. More importantly, as surface wrinkling represents a type of elastic instability, the pattern formation occurs spontaneously and can develop over very large areas. This makes surface wrinkling a very attractive "self-assembled" patterning alternative compared with lithography.

3.1.2 Euler Buckling

The general requirement for surface wrinkle formation is the development of a compressive stress. In the example of the human skin, wrinkling occurs as a result of "squeezing" or compressing a region of the skin. Local bending of the skin occurs at a critical compressive force and leads to the development of wrinkles perpendicular to the direction of the applied compression. To understand the mechanism of wrinkling, we revisit the classic Euler buckling problem.

Developed in the 18th century by Leonhard Euler, the problem considers the stability of a column under axial loading (Fig. 3.2a). When a load, P, is applied to the column, the column deforms with a displacement, δ. The force-displacement curve is represented in Fig. 3.2b.

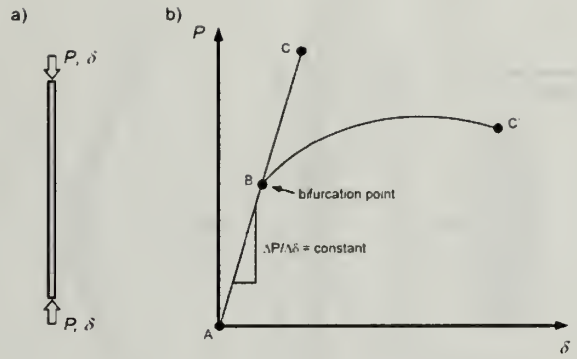

Figure 3.2 – The Euler column. a) Deformation of a column under axial loading, *P*. b) The force-displacement (*P*-δ) curve for the axial deformation of the column.

In the initial stages of the deformation (line AB), the curve scales linearly with a constant stiffness as defined by its slope ($=\Delta P/\Delta\delta$). However, as the deformation becomes greater, the material reaches a bifurcation point (Point B). At this point, the material has 2 possible means of deformation, it can, 1) continue its present course and deform in an axial manner (path BC) or 2) undergo a buckling instability characterized by off-axis deflection (path BC'). Both paths are possible means of deformation, however, path BC' is preferred since it is energetic more favorable. Hence, beyond the bifurcation point B (which also defines the bifurcation load), the column spontaneously deform by buckling, in other words, an elastic instability develops. We now briefly go through a simplified version of beam theory to predict the critical load for buckling and the characteristic length-scale of deformation as a function of material's properties.

In the Euler buckling problem, the column is assumed to have the following characteristics (Fig. 3.3):[47] 1) it is perfectly straight with length, L, 2) the applied axial load, P is axially applied (i.e. along the neutral axis of the column), 3) no transverse load is applied and 4) the material is assumed to be isotropic and free of initial stress. At a critical load, the column buckles with a characteristic deflection.

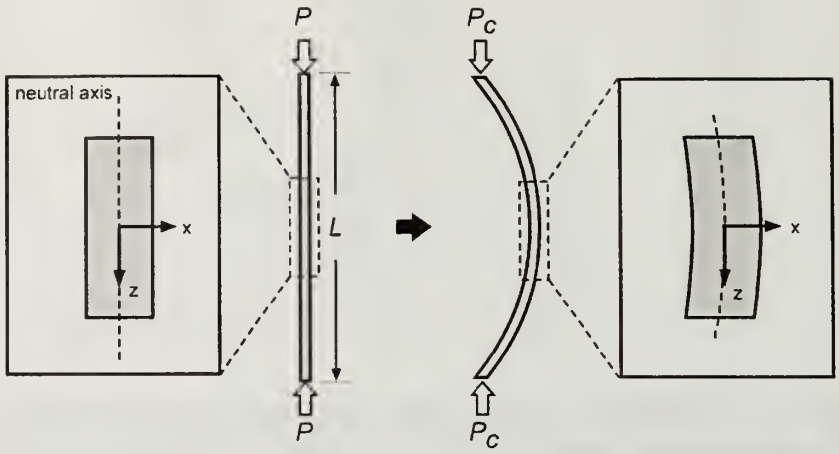

Figure 3.3 – The deflection of the Euler column upon axial load.

The buckling is a result of the bending of the column, i.e. the applied load introduces a bending moment, M_x. This applied bending moment is described as:

$$M_x = -P \cdot dx \tag{3.1}$$

where the "-" is associated with the sign conventional for a compressive force. The bending moment can also be determined by considering a representative element of the column (Fig 3.4) and integrating the axial stress, $\sigma_z=P/A$ over the cross-sectional area, A.

$$M_x = \int_A dx \cdot \sigma_z \cdot dA \tag{3.2}$$

Using the linear constitutive equation for an elastic solid (i.e. Hooke's law), we can define the axial stress:

$$\sigma_z = E \cdot \varepsilon_z \tag{3.3}$$

where ε_z is the axial strain. We can describe the axial strain by relating the deflection of the representative column to its radius of curvature about its neutral axis, R as represented in Fig. 3.4.

$$\varepsilon_z = \frac{ds - ds_o}{ds_o} = \frac{(R + dx)\cdot\theta - R\cdot\theta}{R\cdot\theta} = \frac{dx}{R} \tag{3.4}$$

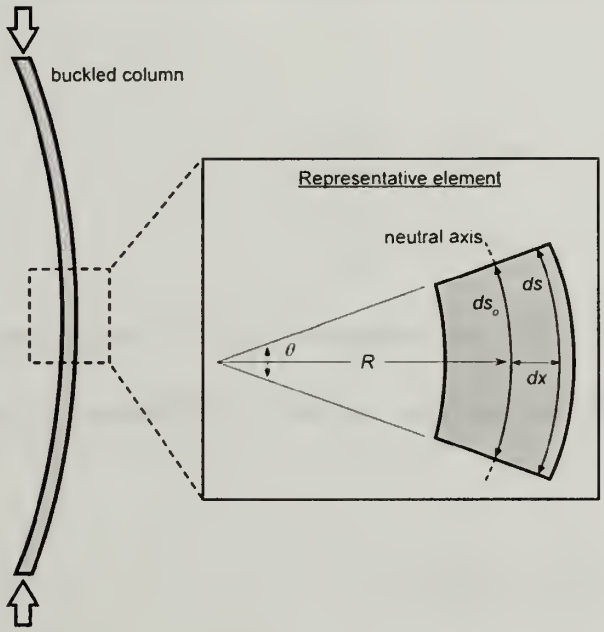

Figure 3.4 – Representative Euler element relating the axial displacement of the column, *ds*, to the radius of curvature, *R*.

Substiting Eqn. (3.3) and (3.4) into (3.2), we obtain the following expression for the bending moment.

$$M_x = \int_A \frac{E}{R}\cdot dx^2 \cdot dA = \frac{EI}{R} = EI\cdot\frac{d^2x}{dy^2} \tag{3.5}$$

where I is the moment of inertia:

$$I = \int_A dx^2 \cdot dA \tag{3.6}$$

Equating Eqn. (3.1) and (3.5), we obtain the following expression:

$$EI\cdot\frac{\partial^2 x}{\partial z^2} + P\cdot dx = 0 \tag{3.7}$$

Due to its eccentricity, we can establish 2 boundary conditions for each end of the column. At each end, we consider that both the deflection and radius of curvature are zero:

$$\begin{aligned} z = 0: \quad & dx = 0, \quad \frac{\partial^2 x}{\partial z^2} = 0 \\ z = L: \quad & dx = 0, \quad \frac{\partial^2 x}{\partial z^2} = 0 \end{aligned} \tag{3.8}$$

Since we have 4 B.C., the solution to Eqn. (3.7) should have 4 constants. Therefore, to account for the four constant, we need to differentiate the equation twice to obtain the following:

$$EI \cdot \frac{\partial^4 x}{\partial z^4} + P \cdot \frac{\partial^2 x}{\partial z^2} = 0 \tag{3.9}$$

where we have assumed that *EI* to be a constant. The general solution to Eqn. (3.9) is:

$$x(z) = A \cdot cos(kz) + B \cdot sin(kz) + Cz + D \tag{3.10}$$

Based on the boundary conditions, we find that:

$$\begin{aligned} & A = C = D = 0 \\ & B \cdot sin(kz) = 0 \end{aligned} \tag{3.11}$$

A nontrivial solution requires that $B \neq 0$. Therefore, the exact solution for an Euler column of length, *L* requires that:

$$\begin{aligned} & sin(kL) = 0 \\ & \Rightarrow kL = n\pi \qquad (n = 1, 2, 3, ...) \end{aligned} \tag{3.12}$$

where *n* describes the mode of the buckled column and *k* is,

$$k = \sqrt{\frac{P}{EI}} \tag{3.13}$$

A more useful length-scale descriptor (and one that we use to describe wrinkled surfaces) is buckle wavelength, λ. For a given mode, n, the column buckles with a corresponding wavelength, λ (Fig. 3.5).

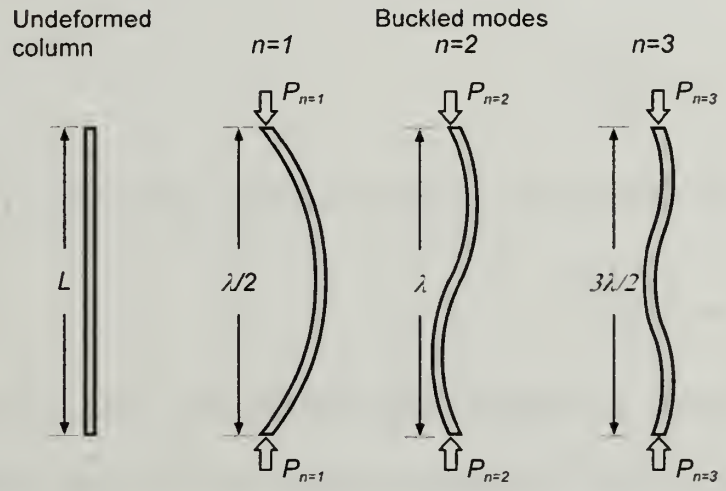

Figure 3.5 – The buckled modes for an Euler column illustrating the first 3 modes and the corresponding compressive force, P_n required for the associated modes.

For the lowest mode (n=1), $\lambda=L/2$, for the second mode (n=2), $\lambda=L$ and so forth. The length-scale λ is actually described by the parameter k since it also represents the reciprocal space length-scale,

$$k = \frac{2\pi}{\lambda} \tag{3.14}$$

Therefore, the relationship between L, n to λ is:

$$\lambda = \frac{2L}{n} \tag{3.15}$$

The specific mode that a column buckles depends on the material's property (E and L) and the applied load. Hence, for each mode, n, there is a critical compressive force, P_n that must be applied. We can predict P_n by substituting Eqn. (3.14) and (3.15) into (3.13).

$$P_n = \frac{n^2 \pi^2 EI}{L^2} \tag{3.16}$$

Assuming the column to be a cylinder of radius, a, then the critical force for buckling is:

$$P_n = \frac{n^2 \pi^3 E a^4}{2L^2} \tag{3.17}$$

Hence, the minimum force needed for buckling a cylinder is (n=1):

$$P_{n=1} = \frac{\pi^3 E a^4}{2L^2} \tag{3.18}$$

One final note in regards to Euler buckling, Eqn. (3.17) can be directly solved by integration of Eqn. (3.7) without assuming that the solution must satisfy the 4th order derivative.

3.1.3 Surface Wrinkling

Surface wrinkling is essentially a two-dimensional analog to Euler buckling. The simplest representation of surface wrinkling is the buckling of a plate or shell. This problem of buckled plates has been well studied during the first half of the 20th century,[48-50] and the interest was motivated primarily by the popularity of thin-walled metallic plates as structural components in aircraft design. Hence, due to the applications of these materials, the primary goal is the development of a failure criterion (critical stress to cause buckling) for the materials with a given plate geometry. As we discuss throughout this chapter, our goal is different in that we are interested in using the instability to generate interesting surface patterns for functional applications.

Specific to surface wrinkling is that the plate is supported by a medium; hence, we must also consider the deformation of this supporting medium. However, the problem is quite similar to the previous buckling of columns and shells, and more importantly, the length-scale of the deflection (such as the wavelength) is still dependent on the material's properties. Recent work by many research groups suggests that surface wrinkling presents a new approach in generating structured materials in technological applications such as optics[42] or electronics[38, 39]. In fabricating surface wrinkles for these applications, a well-developed approach involves buckling a thin film supported on an elastic foundation.[36, 37, 41, 42, 51] Essential to this approach is the presence of a moduli-mismatch surface, i.e. a film adhered to an elastic foundation with different elastic modulus constants. The wrinkling process is described by the following example (Fig. 3.6).

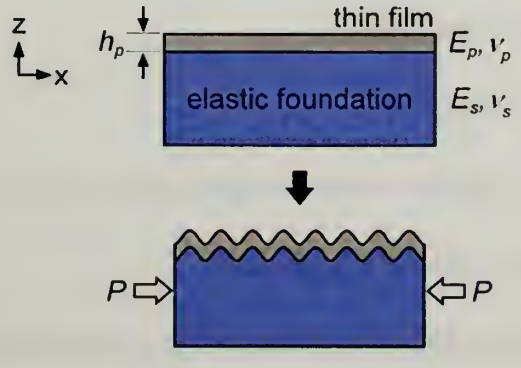

Figure 3.6 – A common approach to forming surface wrinkles by buckling a thin film that is supported with an elastomer.

As we discuss in detail below, the thickness of the film, h_p is related to the wavelength of the wrinkles. Generally, to develop wrinkles on the micron length-scale, the film thickness must be on the order of 1 μm or below. To begin, the thin film is

adhered onto the surface of the elastomer. Adhesion between the two materials is very important to ensure compressive stress transfer in the next step. Then, a uniaxial compressive stress is applied to the elastomer. Since the film is well-adhered to the elastomer, the compressive stress is transferred to the thin film and casues wrinkles to develop on the film surface. Both the dimensions and the critical stress of wrinkle formation (as a function of materials' properties) have been predicted by linear stability analysis (i.e. by a combination of perturbation and energy analysis) and the interested reader can refer to many texts on plate stability.[52, 53] Here, we briefly go through an energy-based stability theory developed by Groenewold.[54]

In Groenewold's theory, he considers the wrinkling of a rigid plate supported by a softer, elastic foundation (Fig. 3.6). He begins by assuming that the plate wrinkles to form aligned one-dimensional wrinkles in response to a net uniaxial compressive force that develops in the composite material. Therefore, the displacement, $w(x)$, of the plate in the z-direction is described as:

$$w(x) = w_o \cdot cos(kx) \tag{3.19}$$

where w_o is the amplitude of the wrinkle surface. The wavenumber, k is related to the wavelength of the wrinkles, λ by $k = 2\pi/\lambda$.

The plate is assumed to deform entirely by bending without stretching laterally. Thus, the bending energy of the plate (per unit area), $\overline{U}_p$ is a function of its thickness h_p, Young's modulus, E_p and Poisson's ratio, ν_p:

$$\overline{U}_p = \frac{1}{48}\frac{E_p}{\left(1-\nu_p^{\,2}\right)} h_p^{\,3} w_o^{\,2} k^4 \tag{3.20}$$

Since the plate is well-adhered to the soft, elastic foundation, any deformation of the plate leads to the deformation of the medium as well. To form a wrinkle with amplitude w_o, the corresponding deformation energy of the medium (per unit area), $\overline{U}_m$ is:

$$\overline{U}_m = \frac{E_m(1-\nu_m)}{2(1+\nu_m)(3-4\nu_m)} {w_o}^2 k \tag{3.21}$$

where E_m and ν_m correspond to the Young's modulus and Poisson's ratio of the medium, repectively.

Therefore, the total free energy (per unit area), $\overline{U}_T$ required to form a wrinkle is a sum contribution from the bending energy of the plate and the deformation energy of the medium.

$$\begin{aligned} \overline{U}_T &= \overline{U}_p + \overline{U}_m \\ &= \left({w_o}^2 k^2\right) \cdot \left(\frac{1}{48} \frac{E_p}{\left(1-{\nu_p}^2\right)} {h_p}^3 k^2 + \frac{E_m(1-\nu_m)}{2(1+\nu_m)(3-4\nu_m)} \frac{1}{k} \right) \end{aligned} \tag{3.22}$$

Minimization of the total free energy results in wrinkles with an optimal wavelength. In other words, λ is determined when:

$$\begin{aligned} \frac{\partial}{\partial k} \overline{U}_T &= 0 \\ &= \frac{1}{24} \frac{E_p}{\left(1-{\nu_p}^2\right)} {h_p}^3 k - \frac{E_m(1-\nu_m)}{2(1+\nu_m)(3-4\nu_m)} \frac{1}{k^2} \end{aligned} \tag{3.23}$$

Simplification of Eqn. (3.23) leads to the final expression relating wrinkle wavelength to the materials' properties of the composite bilayer.

$$\lambda = 2\pi h_p \left(\frac{1}{12} \frac{E_p}{E_m} \frac{(1+\nu_m)(3-4\nu_m)}{\left(1-{\nu_p}^2\right)(1-\nu_m)} \right)^{1/3} \tag{3.24}$$

Assuming that the soft, elastic medium is an ideal, incompressible elastomer, i.e. ν_m=0.5, Eqn. (3.24) simplifies to the following equation.

$$\lambda = 2\pi h_p \left(\frac{1}{4\left(1-\nu_p^{\,2}\right)} \frac{E_p}{E_m} \right)^{1/3} \tag{3.25}$$

Eqn. (3.25) is quite useful as it predicts that the wavelength of the wrinkles is directly proportional to thickness of the plate and scales weakly with the elastic-moduli ratio, E_p/E_m, between the plate and the medium. Furthermore, the theory can accurately predict the wavelength dependence for different variations of composite bilayer systems wrinkled by various external stimuli such as due to thermal expansion mismatch or by a mechanical compression.

3.1.4 Wrinkle Patterns generated by Osmotic Stress

As discussed previously, there are many approaches to generating surface wrinkles. Our approach is similar in principle with the previous approaches in that we also use a material consisting of a moduli-mismatch – i.e. skin layer supported by an elastomer. However, the silimarities end there since we use swelling as a driving force for wrinkle formation and incorporate photochemistry in our swelling agent. Compared with other approaches, our wrinkling methodology offers several unique attributes. First, we take advantage of polymers affinity to solvent as a stimulus to drive wrinkle formation. As almost all polymers are swellable, hence, our process is amenable to many polymer systems. Second, as we are using a solvent to drive wrinkling, we can generate wrinkles that are transient (using a volatile swelling agent) or permanent (the focus of our work using a photocurable swelling agent). Finally, the chemistry and

ultimately, the material properties (such as mechanical or optical) of the final wrinkled material can be tuned by incorporating additives (such as filler particles or nanoparticles) into the swelling agent. As we describe in this chapter, our approach facilitates the spontaneous formation, alignment and more importantly, morphological control of surface wrinkles on a polymer film surface through pre-defined regions of local moduli-mismatch combined with osmotic pressure.

3.2 Experimental Approach

3.2.1 General Wrinkling Process of Oxidized PDMS

We begin by creating a PDMS elastomer using commercially available Dow Corning™ Sylgard® 184 (Dow Corning, Midland, MI). Sylgard® 184 is a two-part kit consisting of a base and a curing agent. The two components are combined in a weight ratio of 10 to 1 base to curing agent and degassed with vacuum for ~40 min. The mixture is then poured onto a glass substrate and cured at 110°C for ~2 hrs. to form the PDMS elastomeric film.

The swelling agent used is a photocurable acrylate based formulation (Table 3.1). The formulation consists of 75 wt% *n*-butyl acrylate monomer (*n*BA, Sigma-Aldrich), 25 wt% ethylene glycol dimethacrylate crosslinker (EGDM, Sigma-Aldrich) relative to the combined weight of the monomer and crosslinker. The two reagents are filtered through an alumina column which consists of a plastic syringe packed with alumina and the syringe opening is capped with a 0.2 μm PTFE filter in order to keep the alumina sand in place. The purpose of this filtering procedure is to remove the

inhibitor that is present in the reagents. This step can be eliminated simply by increasing the concentration of the photoinitiators (~5 wt%). The filtered reagents are combined and added to the 2 commercial photoinitiators (Ciba® Irgacure® 183 & 819) from Ciba Speciality Chemicals. The concentrations for both initiators are kept at 1 wt% relative to the weight of the monomer and crosslinker mixture. The final *n*BA solution yields a clear yellow, low viscosity liquid and is used without further modification. Since the solution is photoactive, we minimize their exposure to light as much as possible. The solution vial is covered with aluminum foil to prevent light exposure during use. When not in use, the solution is kept in an un-lit refrigerator, but any dark cabinet should suffice.

*n*BA formulation			
Monomer	Crosslinker	Photoinitiators	
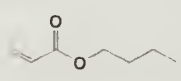	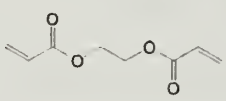	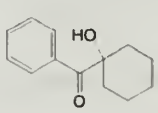	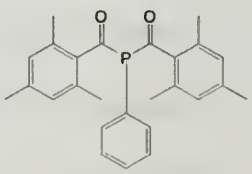
n-butyl acrylate (~75%)	ethylene glycol dimethacrylate (~25%)	Ciba® Irgacure® 183	Ciba® Irgacure® 819

Table 3.2 – The photocurable *n*BA swelling agent.

To generate a film with local moduli-mismatch regions, we UVO oxidize a PDMS elastomer selectively by masking regions with either a copper grid or a thin photoresist layer, which serves as a stencil mask to allow for selective oxidation. The top layer of the exposed regions of the elastomer is converted into a silicate thin film which becomes stiffer and less elastomeric compared with the unmodified PDMS. At this stage, no cracks develop on the silicate surface layer. The entire sample is then

coated with a photopolymerizable *n*BA monomer solution that swells the elastomer, but only causes the wrinkling patterns to form in the oxidized regions – where a local moduli-mismatch of the PDMS exists. Upon photopolymerization with UV, the aligned wrinkling pattern is stabilized and the poly(*n*-butyl acrylate) (P*n*BA) coating is removed to reveal a highly textured, oriented pattern on the PDMS surface (Fig. 3.7a). As revealed by the SEM micrograph, the aligned wrinkling pattern consists of grooves or cusps that form on the surface (Fig. 3.7b).

While the length of the grooves varies from 30 to 300 μm, the periodicity between neighboring grooves remains uniform at approximately 30 μm. To demonstrate scalability in our approach, we show that these self-assembled textured patterns can also be made to span large areas (Fig. 3.7c). For this sample, we oxidized a 20 cm^2 PDMS surface to produce wrinkling patterns that span the entire area. These patterns do not resemble the "spider-web" formation of Fig. 3.7a, but an intricate, intertwined, zipper-pattern develops in this case. Although no attempts were made to induce orientation, local registry of these zipper patterns (Fig. 3.7c inset) is observed. The mechanism responsible for local registry of the zipper patterns is yet to be determined definitively; however, the generation of the zipper pattern is very reproducible and is observed for multiple samples produced in the same manner.

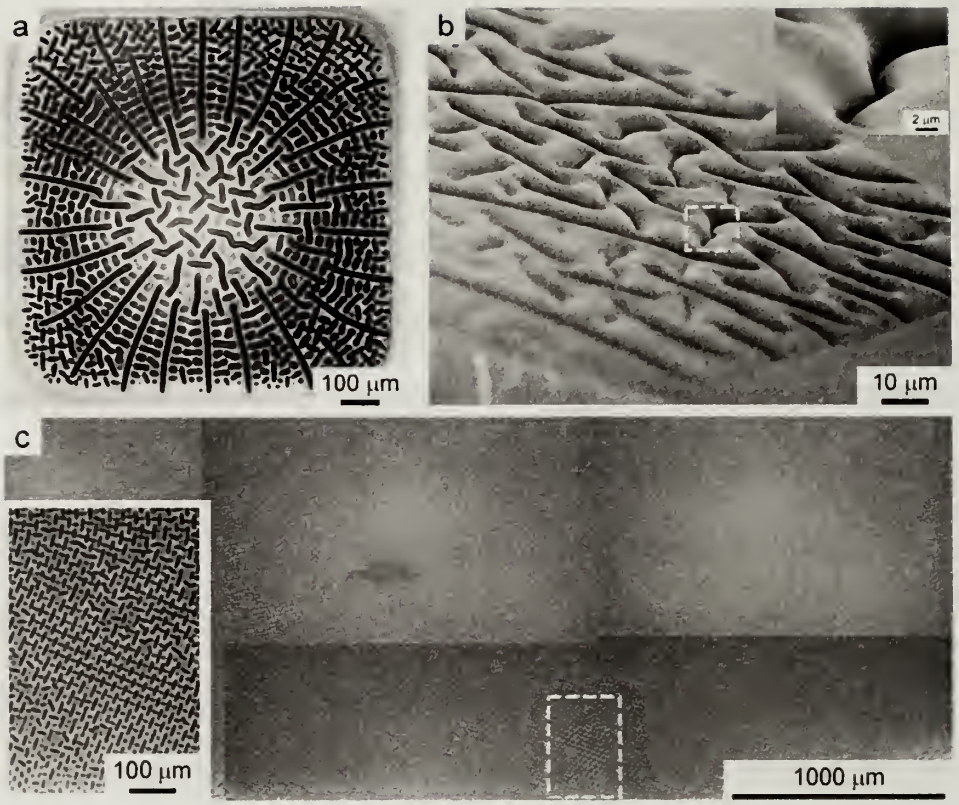

Figure 3.7 – The wrinkled PDMS-silicate film. a) Optical micrograph that illustrates the well-defined surface pattern. b) Secondary electron micrograph (SEM) of the surface wrinkles highlighting the surface topography. c) A composite micrograph stitched together by six separate optical micrographs to demonstrate the scaleablity of our approach. The actual wrinkled surface is a 75 mm x 25 mm area that is patterned in a single procedure. The inset shows that local regions of the surface are well-registered and shows the potential for self-ordering.

3.3 Results and Discussion

3.3.1 Mechanism of Wrinkling

For our process, the surface wrinkles in the following manner (Fig. 3.8). The UVO oxidation converts the top surface of the PDMS into a silicate thin film and creates the necessary local moduli difference in the material.[55] At this point, no surface wrinkles are observed. The PDMS surface is then coated with an *n*BA solution. The

PDMS layer directly beneath the silicate swells in the presence of the monomer solution. If the silicate layer is absent, the PDMS is free to expand and wrinkling is not observed. However, for regions where a rigid silicate layer is present (inset, Fig. 3.8), the expansion of the swollen PDMS becomes laterally confined. Consequently, the swollen PDMS layer experiences competing forces of osmotic pressure (acrylate monomer uptake) versus geometric confinement (as the silicate swells significantly less than the PDMS) and is forced into a complex state of stress. The specific stress distribution is defined by the convolution of the osmotic pressure and the boundary conditions imposed by the shape of the oxidized region. As the silicate layer is covalently bound to the PDMS top layer, strain compatibility boundary conditions must be satisfied at this interface (Fig. 3.8, inset 3B). At a critical degree of swelling, this imposed compressive stress at the silicate-PDMS interface causes both the PDMS and the silicate to buckle (Fig. 3.8, inset 3C). The buckling process, similar to the the buckling of thin rigid films, is essentially a variation of the classic Euler buckling of a rigid rod under compression except in our system the buckling of the PDMS top layer occurs two dimensionally. Besides serving as a swelling agent, the photocurable acrylate solution helps to stabilize the wrinkling patterns. Since the *n*BA solution diffuses into the PDMS prior to the photopolymerization step, the P*n*BA polymer chains interdigitate with the PDMS elastomer after the photopolymerization step. This interdigitation helps to stabilize the surface wrinkling patterns. In instances where it is desireable to generate transient wrinkles, i.e. dynamic wrinkled surface such as designing for a responsive surface; we can simply substitute the photocurable swelling

agent with a volatile swelling agent such as acetone or toluene. In this case, wrinkles develop upon swelling (similar as before) and disappear once the solvent evaporates.

Prior to photopolymerization, a glass superstrate is placed on top of the acrylate solution. Without removal of the glass superstrate, the wrinkling pattern is not observed as there is insufficent optical contrast to observe the patterns. Upon removal, the P*n*BA film fractures in a cohesive manner. The cohesive fracture follows the contour of the surface wrinkling structures due to the extreme mismatch in the near-interfacial moduli.

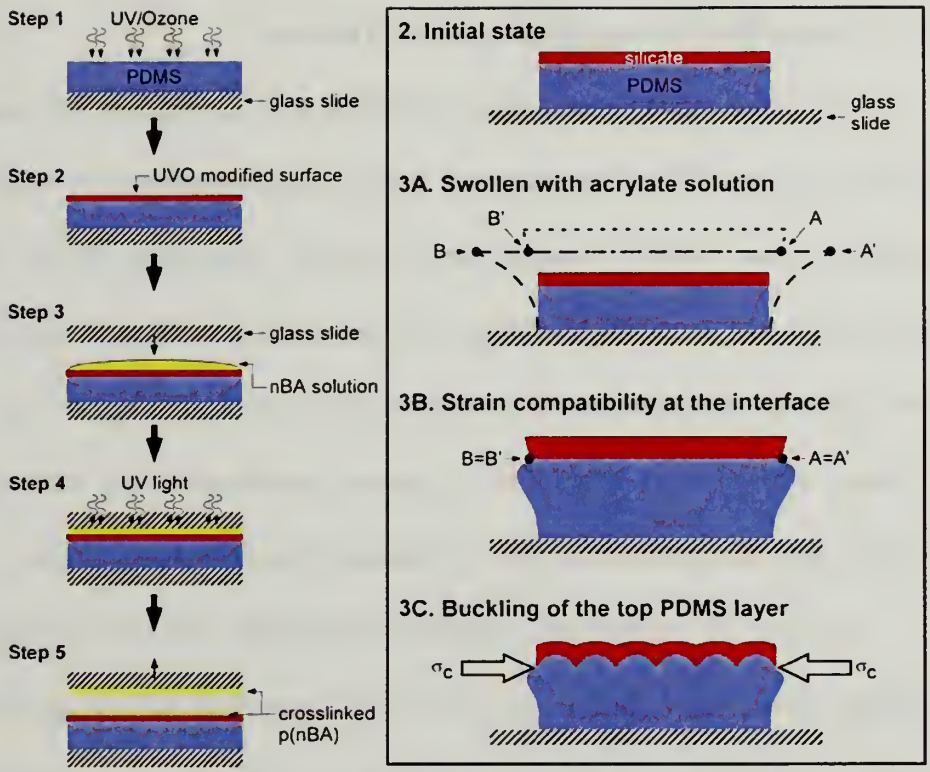

Figure 3.8 – Schematic for the wrinkling process. 1) A PDMS elastomer is oxidized by UV/Ozone. 2) This oxidation process converts the surface of the elastomer into a silicate thin film. 3) To wrinkle the PDMS, the photopolymerizable *n*BA solution is deposited onto the oxidized surface and then covered with a glass superstrate. Due to the presence of the silicate layer, the PDMS elastomer is confined from expanding laterally. As a result, a compressive stress develops at the silicate-PDMS interface, leading to the wrinkling of the PDMS. 4) To stabilize the wrinkles, the acrylate swelling agent is photopolymerized. However, at this stage, the wrinkles cannot be observed due to lack of optical contrast. 5) Finally, removal of the glass superstrate cohesively fractures the acrylate film to reveal the wrinkles. The inset describes the mechanism of wrinkling. The wrinkling process occurs during the swelling step. Normally, for an unconfined bulk elastomer, this simply causes a volumetric expansion. However, due to the presence of the silicate layer adhering to the PDMS surface, a lateral confinement develops at the silicate-PDMS interface which limits the expansion. This strain compatibility condition at the moduli-mismatch interface leads to the development of a compressive stress. In response to this compressive stress, wrinkling patterns develop on the surface of the PDMS. Since the silicate plate thickness is quite thin, the silicate plate is expected to wrinkle as well. due to a combination of swelling and lateral confinement.

3.3.2 Tuning the Wavelength of Surface Wrinkles

To demonstrate control of the wrinkling process, we tune the wavelength of the surface wrinkles. Experimentally, we control the wavelength by varying the UVO oxidation time, which changes the materials' properties of the silicate plate. Specifically, we use a single PDMS film and oxidize sections of the film (and mask other regions with aluminum foil) in increments of 15 min. up to 1 hr. to generate a wrinkled surface with a gradient in pattern wavelegnth. The subsequent steps of swelling and photopolymerization are identical as described previously.

As Fig. 3.9 summarizes, wrinkling wavelength increases as a function of UVO oxidation time. Based on Eqn. (3.25), for a 100 nm thick silicate layer with $\nu_p = 0.33$ and $E_p = 50$ GPa, $E_m = 1$ MPa, we obtain a $\lambda \sim 15$ μm, which is much lower than the experimentally observed wavelength of 27 μm. While this model accurately predicts the buckling wavelength for a bi-layer system consisting of a thin film on an elastic support, our system is more complicated than this. The wrinkling wavelength increases as a consequence of the greater stiffness of the combined dense silicate and intermediate layer, which increases the lateral confinement experienced by the swollen PDMS layer. With increasing oxidation time, the overall silicate layer thickness increases, thus indirectly causing an increase in the buckling wavelength. This is confirmed by our results in Fig. 3.9, where the wavelength of the pattern increases from 27 μm up to 75 μm as we vary oxidation time from 15 min. to 1 hr.

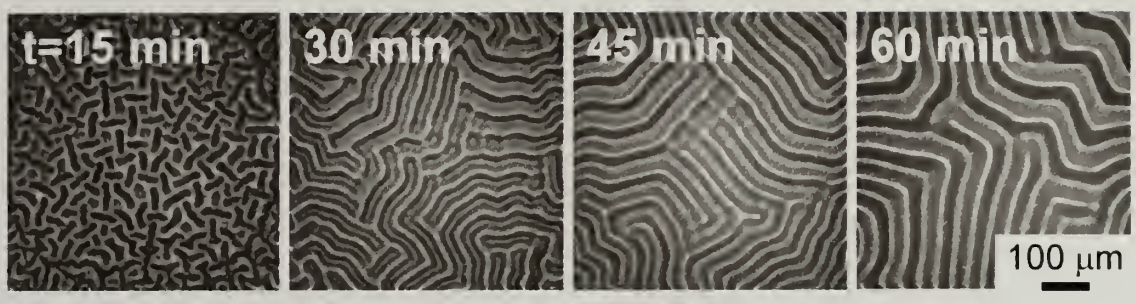

Figure 3.9 – Increase in wrinkle wavelength as a function of UVO oxidation time.

While UVO oxidation is a very convenient surface modification process for PDMS, the oxidation process does not create an ideal composite bilayer system. Previous work by Mirley and Koberstein has demonstrated that the active species responsible for the oxidation is ozone (O_3).[56] Hence, the purpose of the UV irradiation by the UVO cleaner is to convert O_2 into O_3 and explains the reason that the oxidation process is perfomed in atmospheric conditions as opposed to under vacuum. The complication arises as to the source of O_2; does the O_2 source come from the UVO chamber environment or within the PDMS which is also saturated with O_2? If the source of O_2 and hence O_3 is from the chamber, then, the process is a diffusion limited process since O_3 must diffuse into the PDMS. If it is the latter, where the source of O_2 is already present in the elastomer itself, then, the conversion process is limited by the UV light intensity as a function of depth. However, based on previous work, the process appears to be the former, where the UVO conversion is limited by the diffusion process.

Based on the above model for our silicate layer, we rework the buckling model developed by Groenewold to account for the fact the plate is now a composite plate.[54] Again, the total free energy is a sum contribution from the bending energies of the composite plate and the deformation energy of the medium. As a first approximation,

we can describe the total bending energy of the composite plate as a sum of the bending energy of each individual plate with Young's modulus, $E_{p,i}$ and plate thickess, $h_{p,i}$.

$$\begin{aligned}\overline{U}_b &= \frac{1}{48} w_o{}^2 k^4 \left(E_{p,0}{}^* h_{p,0}{}^3 + E_{p,1}{}^* hp,_1{}^3 + \ldots + E_{p,N}{}^* h_{p,N}{}^3 \right) \\ &= \frac{1}{48} w_o{}^2 k^4 \sum_{i=0}^{N} E_{p,i}{}^* h_{p,i}{}^3\end{aligned} \tag{3.26}$$

The deformation energy of the medium is the same as previously described in Eqn. (3.21) since we assume that the medium still deforms by w_o. Hence, minimization of the total free energy as a function of k leads to the modified wrinking scaling relationship.

$$\lambda = 2\pi \left(\frac{1}{12} \frac{(1+\nu_m)(3-4\nu_m)}{(1-\nu_m)E_m} \sum_{i=0}^{N} \frac{E_{p,i} h_{p,i}{}^3}{\left(1-\upsilon_{p,i}{}^2\right)} \right)^{1/3} \tag{3.27}$$

If the silicate plate is characterized as having a gradient in materials' properties, then we can simplify Eqn. (3.27). As a first order approximation, we define an effective modulus for the silicate film that depends on the percentage conversion, ϕ_i to silicate:

$$E_{p,i}{}^* = \phi_i \cdot E_p{}^* \tag{3.28}$$

Substitution of Eqn. (3.28) into (3.27), we obtain the following:

$$\lambda = 2\pi \left(\frac{1}{12} \frac{(1+\nu_m)(3-4\nu_m)}{(1-\nu_m)E_m} \sum_{i=0}^{N} \left(\phi_i \cdot E_p{}^*\right) \cdot \left(h_{p,i}\right)^3 \right)^{1/3} \tag{3.29}$$

To estimate the wavelength for our materials, we need a way to predict how the parameters of $E_{p,i}{}^*$ and h_i changes as a function of depth from the top surface. According to Efimenko *et al*,[55] the UVO process oxidizes the PDMS and converts the top surface into a dense silicate layer (50% conversion to silicate) with a thickness of 5 nm. The thickness of this top layer is virtually unchanged for oxidation times beyond 10 minutes, but beneath this dense layer, there is in an intermediate diffuse silicate layer

with a varying silica density. The thickness of the intermediate layer varies depending on the oxidation conditions and time. Beneath the diffuse layer is the neat PDMS where the UVO process has not chemically altered the composition. In other words, we can treat our silicate layer as a bilayer which simplies the summation of Eqn. (3.29) to the following:

$$\sum_{i=0}^{N}\left(\phi_i \cdot E_p^{*}\right)\cdot\left(h_{p,i}\right)^3 = \left(\phi_{top}\cdot {h_{top}}^3 + \phi_{inter}(t)\cdot h_{inter}(t)^3\right) \tag{3.30}$$

We take the results from the data for UVO conversion of PDMS from Efimenko *et al.* (Fig. 3.10) and extrapolate the parameters, ϕ_{top}, h_{top}, ϕ_{inter} and h_{inter}, which correspond to the silicate conversion parameter of the top layer, thickness of the top layer, silicate conversion parameter of the intermediate layer and thickness of the intermediate layer, respectively. Based on their results, we obtain the following:

$$\phi_{top} = 0.5 \tag{3.31}$$

$$\phi_{inter}(t) = 0.002\cdot t + 0.04 \tag{3.32}$$

$$h_{top} = 5nm \tag{3.33}$$

$$h_{inter}(t) = (0.36\cdot t + 13)nm \tag{3.34}$$

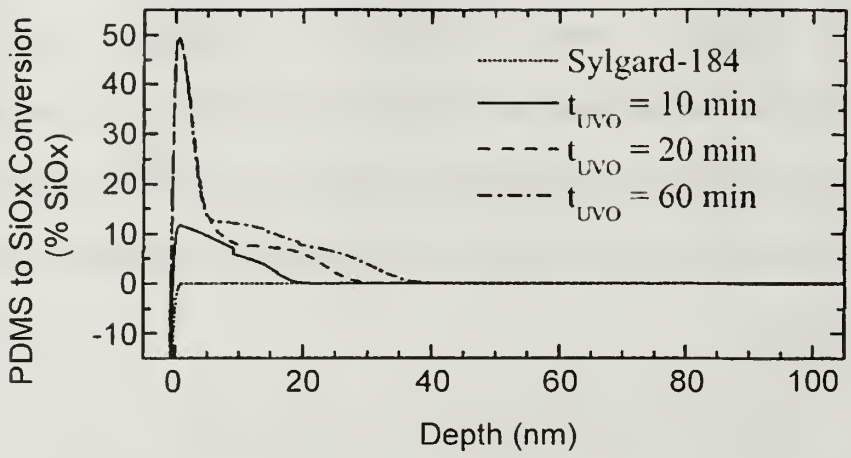

Figure 3.10 – UVO conversion of PDMS to silicate results from Efimenko *et al.*[55]

As the specific UVO conditions vary depending on the UVO light intensity as well as the distance from the light source to target, we can only assume that the results from Efimenko *et al.* are simply UVO conversion trends as a function of the oxidation time for the process. To account for the differences in the UVO conditions, we develop the final expression with a fitting constant that takes into considersation the differences in UVO oxidation. Specifically, the fitting constant, C attributes the differences only to the change in the intermediate layer thickness ($C = 21$).

$$\sum_{i=0}^{N}\left(\phi_i \cdot E_p^{\,*}\right)\cdot\left(h_{p,i}\right)^3 = \left(\phi_{top}\cdot h_{top}^{\,3} + \phi_{inter}(t)\cdot\left(C\cdot h_{inter}(t)\right)^3\right) \tag{3.35}$$

Substituting Eqn. (3.31), (3.32), (3.33), (3.34) and (3.35) into Eqn. (3.29), and assuming the following materials' constants for the silicate skin ($E_s^* \approx 10$ GPa) and PDMS ($E_m^* \approx 0.3$ MPa), we fit our experimental results to relate wrinkling wavelength to oxidation time (Fig. 3.11). One final note, Young's modulus for the PDMS is the elastic constant of the elastomer swollen with *n*BA.

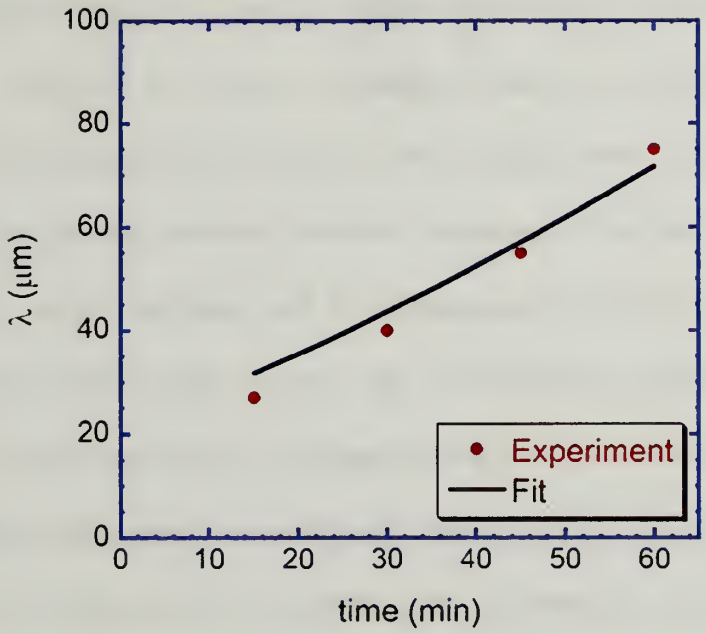

Figure 3.11 – Scaling relationship of buckling wavelength, λ vs. oxidation time. Although the UVO oxidation creates a multilayer silicate film with different elastic modulus and thickness values, we replaced them with an effective modulus, E_{eff}^{*} and total layer thickness, h_p. The solid curve represents a fitting function that we develop based on the experimental results from Efimenko *et al.*[55] for the UVO oxidation of PDMS films.

3.3.3 Aligning Surface Wrinkles

The orientation of the surface wrinkles is associated with the direction of the applied compressive stress. In the wrinkling of skin, wrinkles align perpendicular to the direction of the compression direction. Previously, several research groups have demonstrated that the formation of aligned or one-dimensional (1-D) wrinkles occurs with the application of a primary buckling stress.[37, 42] In all the previous examples that demonstrate this alignment, the approach taken requires either a topographic PDMS elastic foundation to define the primary stress or the specific application of a uniaxial compressive stress. For a patterned elatic support under biaxial compression, the boundary conditions defined by the physical edge of a topographic feature leads to the

development of a primary compressive stress. Consider the following example of a thin plate attached to a pattern elastomer (Fig. 3.12). Far from a pattern feature, the compressive stress applied to the elastomer is transferred to the top plate. Hence, this region forms the 2-D isotropic wrinkles. However, near the physical edge of a pattern feature, due to the discontinuity of the elastomer surface, the compressive stress perpendicular (x-direction) to the feature edge becomes discontinuous. Since the elastomer is a continuous medium parallel to the feature edge (y-direction), the stress is still continuous parallel to the edge. Hence, a topographic surface provides control of the primary compressive stress direction. This control has been demonstrated by Bowden *et al.* on the wrinkling of a gold thin film that is supported by a patterned PDMS elastomer.[36] Upon formation of the surface wrinkles using a biaxial compressive stress due to thermal-mismatch between the gold and PDMS, they observe that the wrinkles align normal to the edges of the pattern feature as depicted in Fig. 3.12.

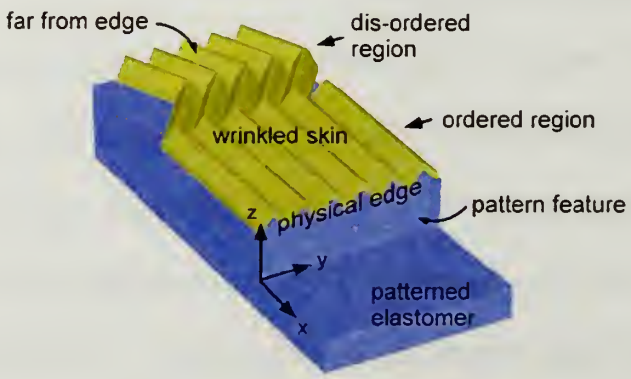

Figure 3.12 – Ordering of surface wrinkles at a physical edge of a patterned elastomer.

Our approach to generating aligned wrinkles is unique in that the PDMS elastomer is not a topographic surface nor do we apply a uniaxial mechanical

compressive stress. Rather, we generate specific regions moduli-mismatch regions on the PDMS surface which defines the primary buckling stress upon swelling by the acrylate monomer. The alternating moduli-mismatch regions are defined by oxidizing alternating striped regions of a PDMS film using a patterned positive photoresist as the stencil mask (Fig. 3.13).

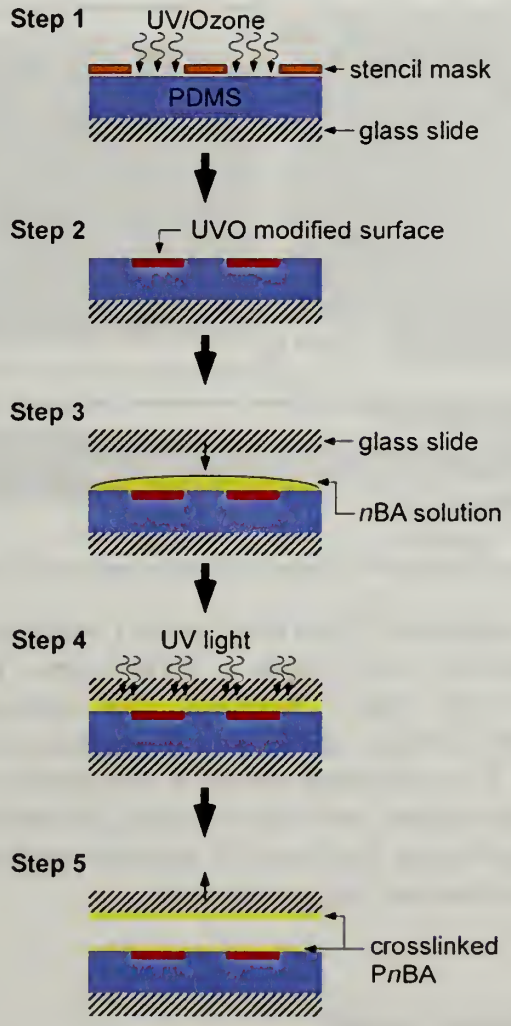

Figure 3.13 – The selective UVO oxidation procedure to forming the moduli-mismatch PDMS surface. The stencil mask used is a patterned photoresist. The subsequent oxidation, swelling and wrinkling steps are identical as before.

The results of Fig. 3.14 confirm our control over the alignment of the surface wrinkles. At the center of the "starburst" pattern, the surface wrinkles are randomly

oriented since the geometric constraint is not biased. By confining the formation of the surface buckles within the oxidized strip (Fig. 3.14b), alignment is clearly observed. Additionally, the orientation of the wrinkles persists over a finite length, ζ beyond which the wrinkles become disordered. This persistence length has been discussed theoretically by Groenewold and we again revisit the theory.

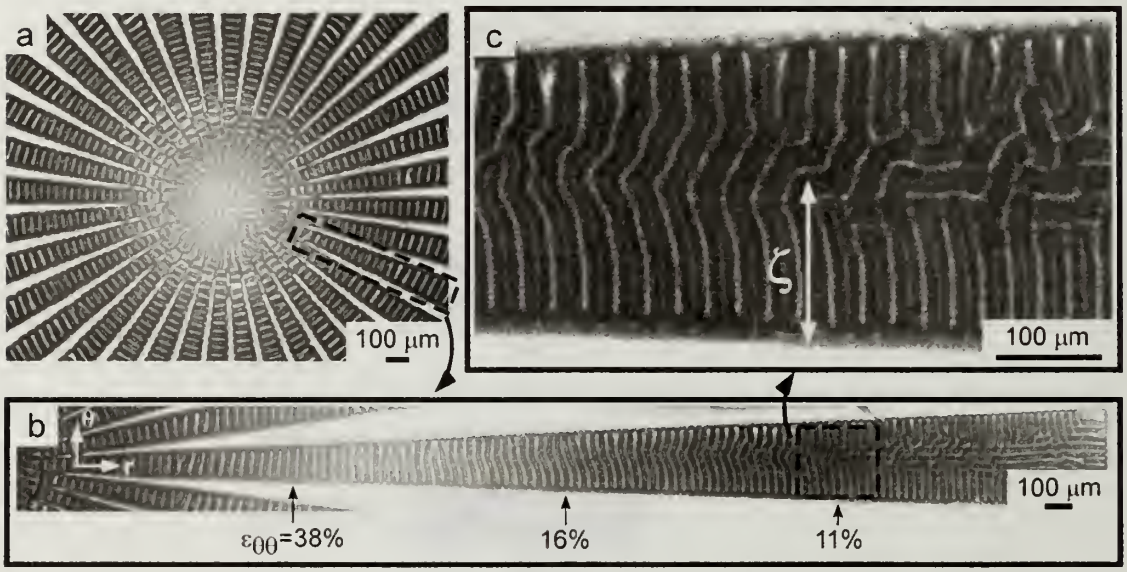

Figure 3.14 – Alignment of surface buckles using stripes of UVO lines. a) The "star-burst" pattern. b) Within a UVO stripe, the surface wrinkles orient perpendicular to the radial direction. The ordered wrinkles persist over a persistence length, ζ, which scales with the azimuthal strain, $\varepsilon_{\theta\theta}$ and the modulus mismatch ratio. The azimuthal strain is calculated by comparing the change in width of the stripe before and after exposing the PDMS to acrylate solution. The highlighted region shows the onset of disorder wrinkles. c) ζ is determined from this region where disorder begins to occur.

3.3.3.1 The Persistence Length

Groenewold's persistence length theory is a continuation of the wrinkling theory presented in Section 3.1.3.[54] In his theory, Groenewold considers only applying a uniaxial compressive stress to form aligned 1-D wrinkles with a characteristic wavelength, λ (Fig. 3.14). To account for the fact that 2-D random wrinkles develop as

a result of a biaxial compressive stress, he considers that the scenario is the equivalent to the assembly of multiple unit cell of 1-D wrinkles that are connected by defect regions. Next, Groenewold introduces a length-scale called the pereistence length, ζ. This correlation length is often used in other polymer fields such as the description of the Kuhn length of a polymer chain or the correlation length in mesogens in liquid crystals. Here, ζ is used to describe the distance over which the wrinkles are aligned, beyond which the alignment of the wrinkles are uncorrelated. Hence, the size of each unit cell is determined by the magnitude of the persistence length, specifically, the lateral dimension size is $\sim\zeta^2$.

In order to assemble or stitch multiple unit cells together to form a 2-D isotropic wrinkled surface, defects are generated where the unit cells meet (Fig. 3.15).

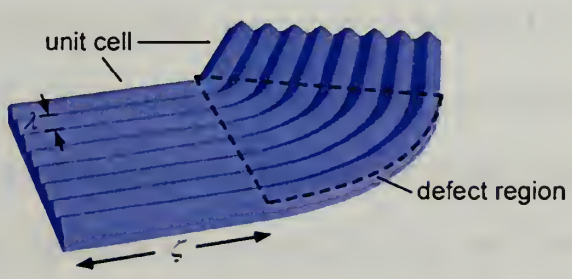

Figure 3.15 – Groenewold's persistence length theory model.

Again, from a free energy prespective, the generation of defects leads to a penalty since a portion of the total energy that was originally used to cause wrinkling is now expended to form defects. Hence, the final expression developed by Greocnewold that minimizes the total number of defects by predicting the persistence length, ζ is:

$$\zeta \approx \lambda \cdot \left(\frac{1}{2\varepsilon^2} + 2 \cdot \left(\frac{1}{4\left(1-\nu_p^{\,2}\right)} \frac{E_p}{E_m} \right)^{1/3} \right) \tag{3.36}$$

Using Eqn. (3.36), we predict the persistence length based on the azimuthal strain, $\varepsilon_{\theta\theta}$ ($\varepsilon=\varepsilon_{\theta\theta}$) of the local region and the modulus-mismatch ratio (E_p/E_m). Using an estimated strain of 11% (determined by the change in width prior to monomer swelling and after the wrinkle formation) and a calculated modulus-mistmatch ratio, we calculate ζ~170 μm, which is comparable to the measured value of 155 μm obtained from Fig. 3.14c.

3.4 Phase Transitions of Wrinkle Patterns

In all the previous work based the elastic foundation approach, only 2 types of buckling morphologies are generated. Aligned 1-D wrinkles are observed on application of a uniaxial compressive stress while the herringbone pattern (essentially the 2-D analog of the 1-D pattern) is observed is observed with a biaxial compressive stress. These morphologies are predicted by linear stability analysis for a semi-infinite, homogeneous plate. However, what is not considered is when boundary conditions play a significant role in the wrinkling process, i.e. when the lateral dimensions of the thin film become commensurate with the dimensions of the wrinkles. Since we can control the lateral dimensions of the silicate film simply by defining the specific oxidized regions, our wrinkling approach is well suited for understanding the effects of boundary conditions on the resultant wrinkle morphologies.

We employ the previously described wrinkling process (used to generate the aligned wrinkles) to produce alternative buckling morphologies (Fig. 3.16). The only change we have made to our wrinkling approach is to replace the previous rectangular shaped stencil mask patterns with axisymmetric patterns of hexagonal patterns,

specifically; we use transmission electron microscopy (TEM) grids as stencil masks. The procedure is summarized in Fig. 3.16a.

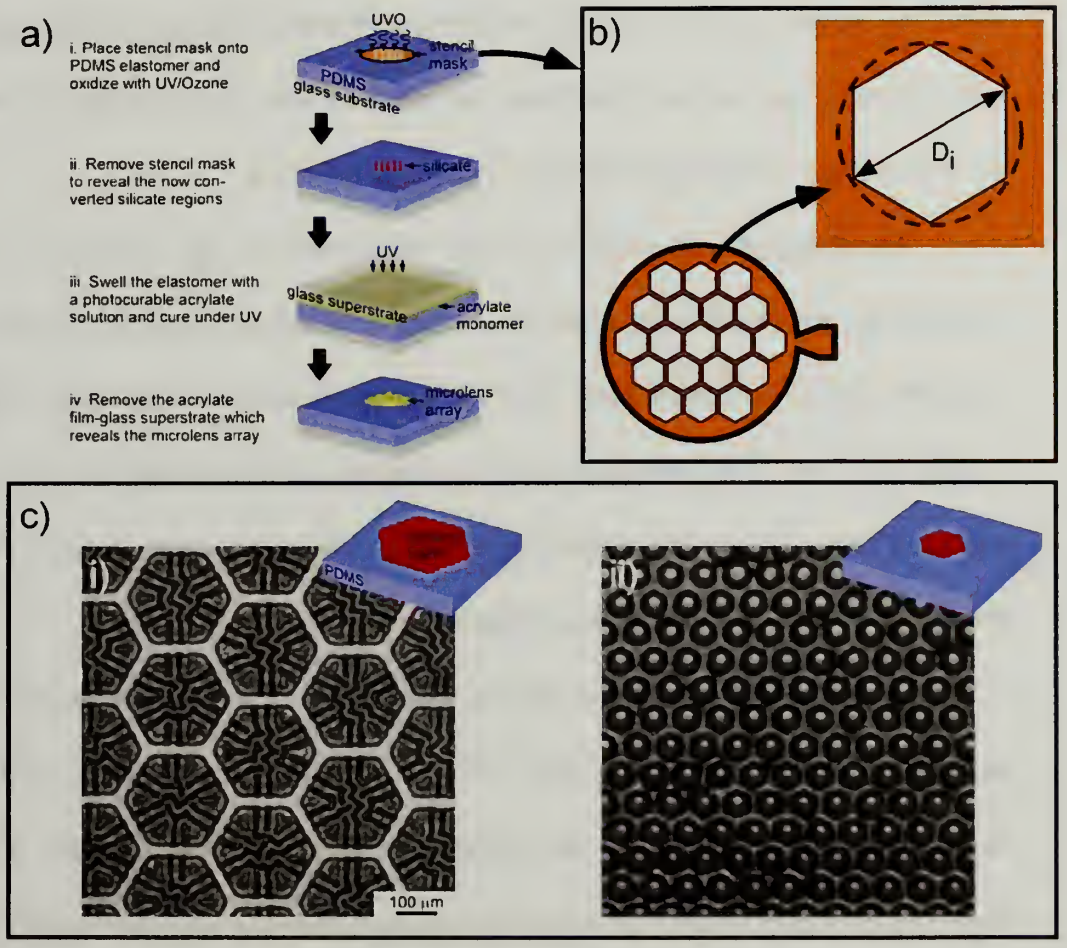

Figure 3.16 – General scheme for the fabricating the microlens arrays on planar PDMS surface based on our surface wrinkling approach.

The representative TEM grid that is used as the stencil mask is depicted in Fig. 3.16b. We describe the size of the hexagonal holes of the TEM grids by approximating them as circular openings of diameter, D_i. D_i is an important pattern feature size scale since the resultant wrinkling morphology depends on the lateral dimensions of the silicate-like plate (converted from the UVO process) as defined by D_i. The change in lateral dimensions of the silicate plate alters the morphology of the buckling patterns

and manifests due to the existence of new boundaries defined by the edges of the finite silicate plate. As an example, we demonstrate the effects of D_i on the resultant wrinkling morphology (Fig. 3.16c). For the same PDMS elastomer oxidized at the fixed oxidation time and swelling conditions but oxidized with stencil masks of two distinct D_i, the resultant wrinkling morphologies are quite different.

To investigate the effects of plate dimensions on the changes in wrinkling morphology, we create a combinatorial library of microlens arrays on a planar PDMS substrate where we systemically vary the oxidation time as well as the size of the oxidized regions. Both parameters serve to change the overall stiffness of the silicate layer and hence, dictate the morphology of the wrinkling structures formed. The results are presented in the following phase diagram.

Given the parameter space of plate diameter, D_i vs. oxidation time, we observe 3 distinctive wrinkle morpholgies (Fig. 3.17). At the largest diameter (D_i ~650 μm), the random 2-D isotropic wrinkles are generated (Fig. 3.17, IV). This result is expected since the boundary defined by the plate diameter does not influence significantly the formation of the wrinkles. Hence, away from the plate edges (specifically, at the center of the plate as shown in the micrographs in Fig. 3.17), 2-D isotropic wrinkles develop. As the plate diameter is reduced slightly (D_i ~300 and 200 μm), we see that the wrinkles align normal to the plate edge (Fig. 3.17, III). Interestingly, as we continue to decrease the plate diameter (D_i < 100 μm), two completely new wrinkling morphologies (which has not been previously reported) are observed. Both of these new morphologies are unique in that they are axi-symmetric patterns. The first axi-symmetric structure is the dimple morphology (Fig. 3.17, II) and the second structure is the microlens

morphology (Fig. 3.17, I). The microlens morphology is particular interesting for application in optics and we dicuss this application in detail in section 3.4.1. But first, we must understand how these phase transitions occur and the material's properties that determine these morphological changes.

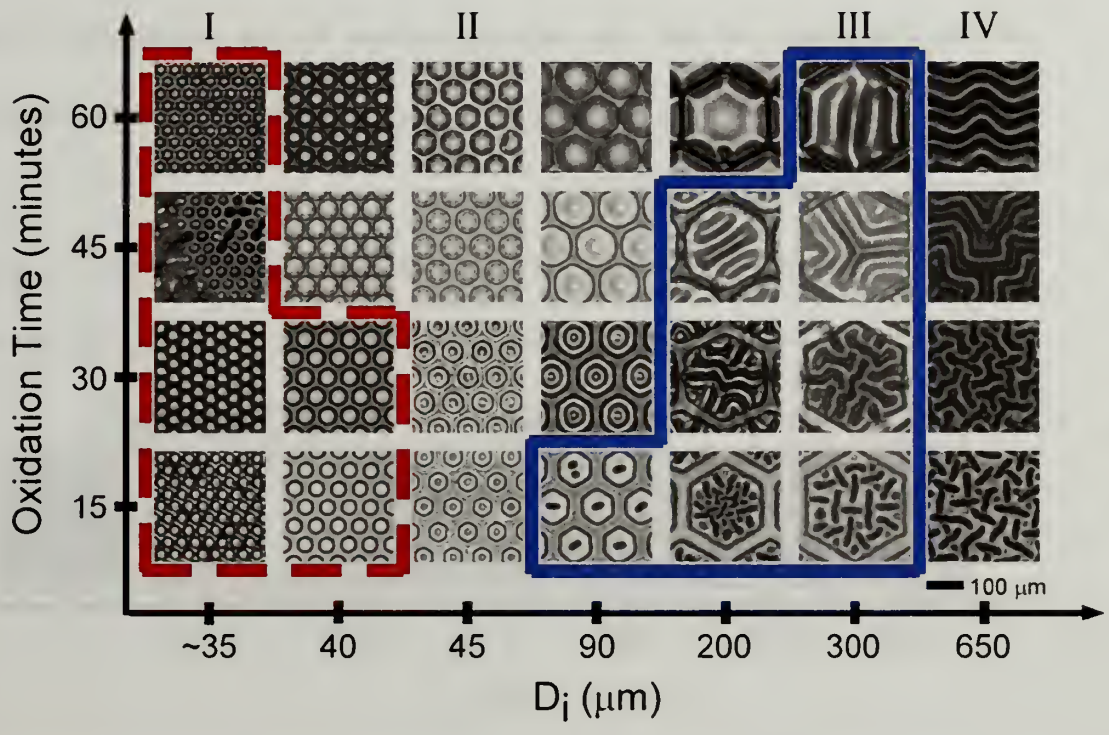

Figure 3.17 – Morphologies of the wrinkled structures observed. Using a combinatorial approach, we vary simultaneously the oxidation time and size of the oxidized region, D_i on a planar PDMS surface. For a nearly semi-infinite case, the random 2-D wrinkled patterns are formed (IV). At low levels of confinement, we again observe the formation of 2-D isotropic wrinkles (III). However, as we further decrease D_i, lateral confinement plays a significant role as the dimpled (II) and microlens (I) buckled structures are observed.

Prior to swelling by the acrylate monomer, the silicate plate has an initial plate diameter, D_i. Upon swelling, the silicate plate expands laterally to a final plate diameter, D, where $D=D_i*(1+\varepsilon)$. This length-scale is important in the control of since we help define this experimentally. Similarly, an important materials' length-scale is the

persistence length. As a first approximation, we can define the ratio of D/ζ as a dimensionless confinement parameter that can used to predict the phase transitions. We use Eqn. (3.32) to calculate ζ for the wrinkled patterns. We estimate the local strain, ε by comparing the differences in the lateral dimensions of the oxidized regions prior to the swelling stage and after the buckling process for our combinatorial library of oxidized patterns. Based on the estimation of ε and with our prior knowledge of we determine ζ values for the wrinkles.

As an example (Fig. 3.18), we use this confinement parameter to evaluate a single row of wrinkled structures within the phase diagram (i.e. row 2, Fig. 3.16).

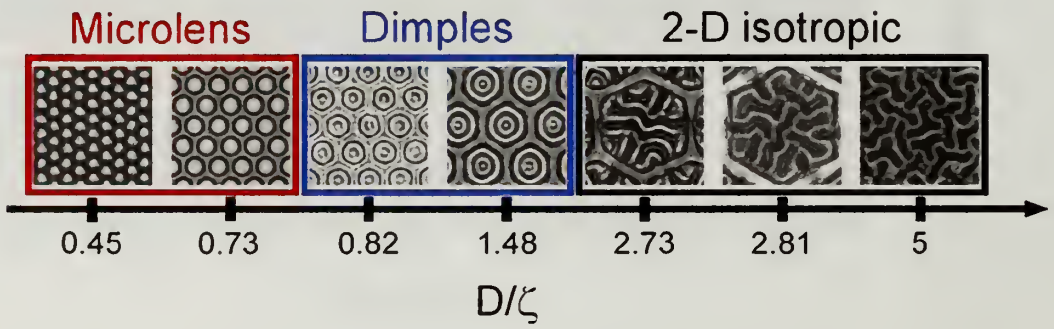

Figure 3.18 – Row 2 of the phase diagram in Fig. 3.17 illustrating the relationship of wrinkling phases as a function of confinement parameter, D/ζ.

In essence, the confinement parameter defines the commensuratibility between the experimental and material's length scales. We define the confinement parameter for row 2 of the phase diagram (from Fig. 3.17). When the $D/\zeta > 1$, the plate diameter is much larger than the persistence length of the wrinkle. Hence, 2-D isotropic wrinkles form since the plate boundaries do not influence significantly (except near the edges of the plate) the formation of the wrinkles. As we continue to reduce the plate diameter, i.e. to the point that the two length scales become commensurate ($D/\zeta \sim 1$), the phase transition

occurs where the wrinkles change from the 2-D isotropic to the dimple morphology. This new dimple morphology is significantly different from the previous 2-D isotropic morphology in that it is axi-symmetric. Qualitatively, the axi-symmetry is a result of satisfying the axi-symmetic compressive stress state defined by the silicate plate; the plate is significantly small such that the net compressive stress is a hoop stress that causes the silicate plate to compress axi-symmetrically inward. Again, we observe the axi-symmetry at the second phase transition, specifically, when the microlens morphology forms. The microlens morphology is a result of the highest confinement that we develop for our materials ($D/\zeta<1$); in essence, only a portion of the wrinkle can be accommodated within the confines of the silicate plate. Referring back to Euler buckling, both the dimple and microlens morphologies are axi-symmetic structures that are two-dimensional analogs to the one-dimensional Euler buckling modes. Similar to the Euler buckling of a column, the microlens pattern constitutes the lowest symmetric buckling mode, which is a half-wavelength. For the dimple pattern, we interpret the buckled structure as the next higher order symmetric buckling mode.

To further demonstrate that the wavelength of the dimples is a half-wavelength, we plot the relationship of λ/λ_o versus $D/2\lambda_o$ for all the patterns in Fig. 3.18. The parameter λ is the measured wavelength for the wrinkled structure of interest. We define λ_o as a material-defined quantity that is measured independently from the 2-D isotropic wrinkling patterns (Fig. 3.17, IV). For the 2-D isotropic patterns where confinement is minimal, λ approaches λ_o as expected, i.e. $\lambda/\lambda_o\sim1$. As we decrease the silicate plate diameter, again, we see that $\lambda/\lambda_o\sim1$. Only when the microlens morphology forms do we see that the relationship of λ/λ_o deviates from unity. Specifically, in

instances where the microlens morphology forms, λ/λ_o scales as $D/2\lambda_o$ as illustrated by the linear relationship in Fig. 3.19, which confirms their diameter is approximately a half-wavelength.

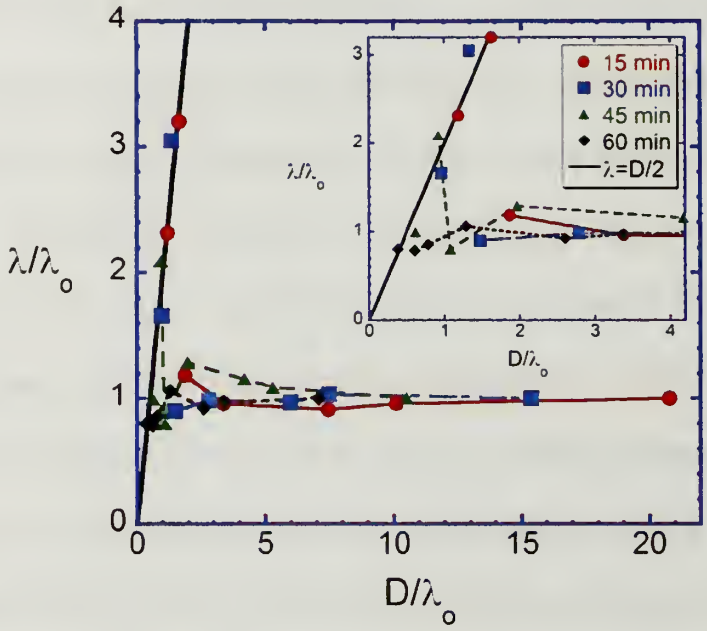

Figure 3.19 – Phase map summarizing the effects of silicate layer lateral confinement on the resultant wrinkled structures formed. The plot demonstrates the role of lateral confinement, as expressed by the ratio (D/λ_o), on the resultant wrinkled structures.

3.4.1 Buckled Microlens Array Pattern as an Optical Device

One of the interesting and unique features of our wrinkled materials is that they can be directly used as functional devices without further modification. Their application as a "smart" adhesive is discussed in Chapter 4. Additionally, the microlens structure is potentially useful as an optical device for imaging purposes. To demonstrate the lensing properties of our microlens, a projection experiment is performed on the planar microlens array (Fig. 3.20). First, the microlens array is positioned onto the sample stage of an optical microscope, illuminated with transmitted white light and

characterized under bright-field mode (Fig. 3.20a). Next, the microlens array is illuminated with white light from below through a projection template, which is simply a printed transparency with transparent letters of CRG (which stands for Crosby Research Group). Finally, the miniaturized letters are projected onto the focal plane of the microlens array and imaged through the objective lens of the microscope. As Figure 3.20b shows, we observe a hexagonal array of miniaturized CRG letters on the microlens arrays. This demonstration illustrates the capability of our microlens arrays to be employed as optical elements.

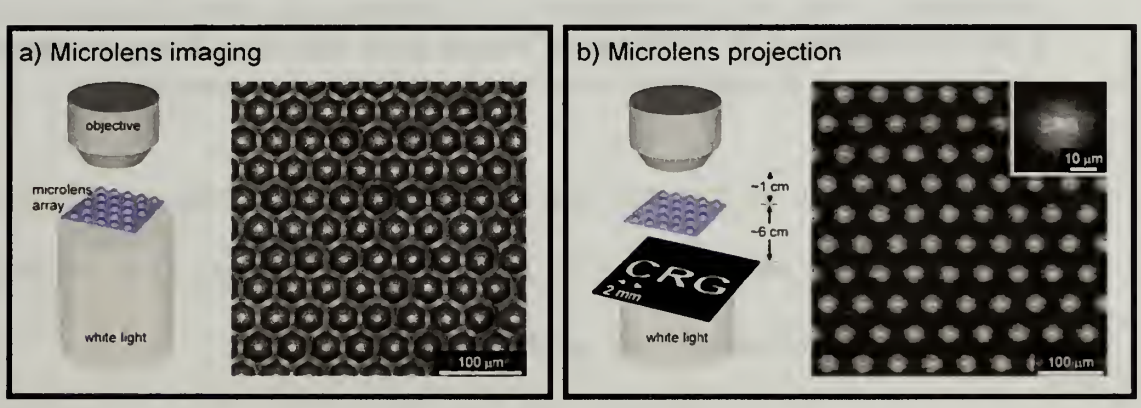

Figure 3.20 – The light projection experiment. a) Optical micrograph of the microlens array fabricated using our wrinkling process. The RMS roughness is measured by tapping mode AFM to be 2.15 nm. b) To demonstrate the lensing properties of our microlens arrays, we devise a microscope projection experiment where we project the letters CRG onto the focal plane of the microlens array. Miniaturized letters are observed on every microlens when imaged through the objective lens of the microscope.

The radius of curvature, R of a microlens controls many properties of the microlens array. We control R by adjusting either the silicate thickness or lateral dimensions of the silicate region. As Fig. 3.21 shows, R decreases with increasing oxidation time (i.e. silicate stiffness) while for a given oxidation time, R increases with D.

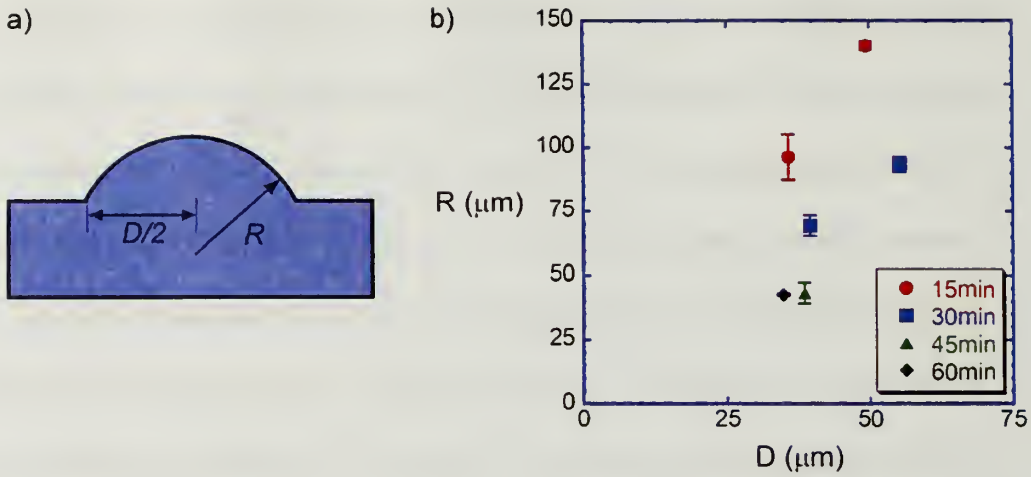

Figure 3.21 – Radius of curvature of the microlens. a) Schematic of the microlens morphology where we approaximate it as a spherical cap with radius of curvature, *R* and cap diameter, *D*. b) Effects of silicate plate diameter, *D* and oxidation time on the changes in the radius of curvature for the microlens morphology.

The change in R is due to a combination in the changes in the wrinkling amplitude and the plate diameter. We can predict the curvature of the microlens by assuming that the microlens forms as spherical cap (Fig. 3.22).

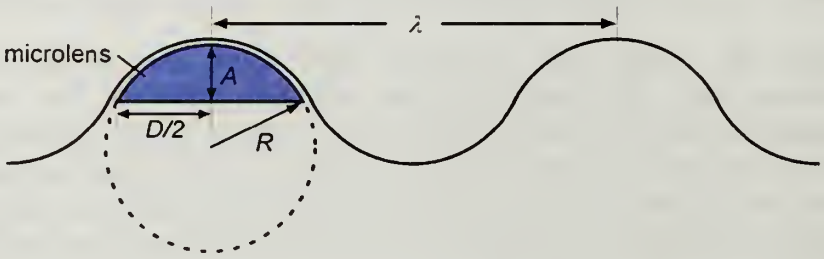

Figure 3.22 – Approximating the microlens as a spherical cap with a radius of curvature, *R*.

For this geometry, the radius of curvature, R is related to the amplitude of the wrinkle, A and the plate diameter, D by the Pythagorean theorem.

$$R = \frac{1}{2A} \cdot \left(A^2 + \left(\frac{D}{2} \right)^2 \right) \tag{3.33}$$

According to Cerda and Mahadevan, the amplitude of a wrinkled surface scales with the buckling wavelength and the compressive strain.[57]

$$A \propto \lambda_o \cdot \varepsilon^{1/2} \tag{3.34}$$

Based on the amplitude scaling relationship with buckling wavelength λ_o and strain ε, we develop an expression that relates R to λ_o, D and ε:

$$\frac{R}{\lambda_o} \approx \left(\frac{D}{\lambda_o}\right)^2 \left(\frac{1}{8\varepsilon^{1/2}} + \frac{\varepsilon^{1/2}}{2\left(D/\lambda_o\right)^2} \right) \tag{3.35}$$

Fig. 3.23 illustrates that we are able to predict the experimental results quite nicely by using a constant strain of ~5% (again, measured by the change in diameter prior to monomer swelling and after the wrinkle formation) for all the microlens samples. The results demonstrate our ability to control the curvature of the microlens structures through either the size of the oxidized region or the oxidation time of the PDMS substrate.

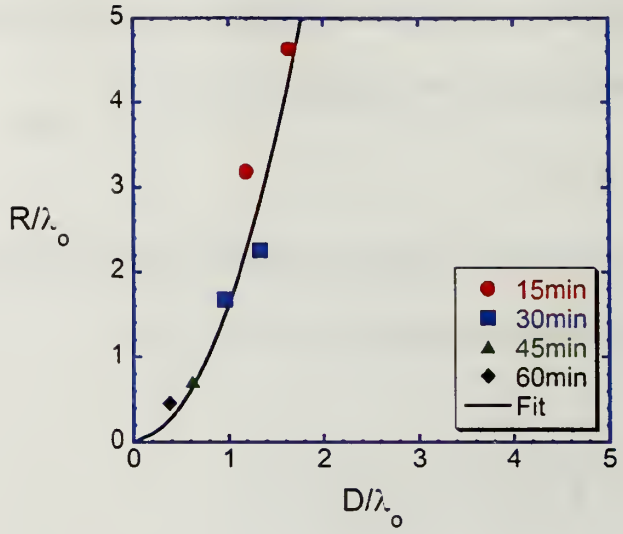

Figure 3.23 – The dimensionless radius of curvature vs. dimensionless silicate-plate diameter plot for wrinkling patterns that form the microlens morphology.

3.4.2 Compound Lens

The versatility of our approach allows for the fabrication of a compound lens whereby the microlens array decorates the surface of a PDMS hemisphere (Fig. 3.24). Unlike previous approaches to fabricating a compound lens, our process is quite simple and rapid as fewer fabrication steps are needed. Compared to conventional microfabrication patterning techniques, our approach facilitates patterning on non-planar substrates. Patterning non-planar surfaces is often a challenge with conventional microfabrication since most of the approaches are limited to patterning in 2-D. For example, in photolithography, the process is essentially a variation of photography – i.e. transfer of a 3-D pattern onto a 2-D surface. Hence, this inherent limitation prevents lithography to patterning materials in 3-D.

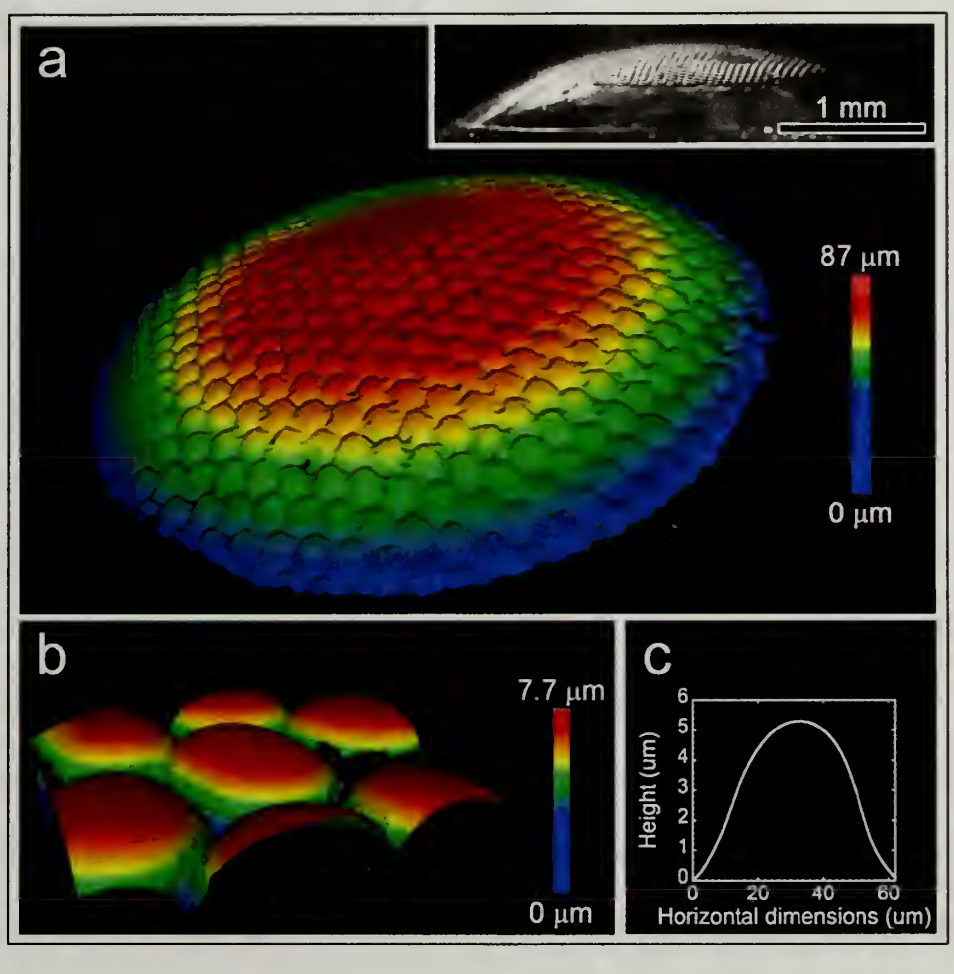

Figure 3.24 – Structure of the compound lens. a) Optical profile of the microlens structures on a PDMS hemisphere. The insert illustrates the overall dimensions of the compound lens. b) Magnified optical profile of microlens surface and c) surface profile of a single microlens measured using a stylus profiler. The dimensions of a microlens are approximately 5 µm in height and 60 µm in diameter.

To fabricate the compound lens, we begin by creating a PDMS hemisphere. Our approach to generating the hemisphere is unique in that we rely on surface tension between immiscible fluids to form the hemspherical surface – water and PDMS oligomer (Fig. 3.25a). Specifically, we begin by preparing and degassing the Sylgard 184 mixture (10:1 base to curing agent wt. ratio). Next, we deposit ~0.1 mL of the PDMS mixture onto a glass substrate, making sure that the PDMS droplet is circular.

The droplet spreads (grows in diameter to ~5 mm) due to the low surface tension between the PDMS-glass interface. Following this step, the glass substrate is placed into a sufficiently large water bath. Since PDMS is hydrophobic, the PDMS droplet wants to minimize its interaction with water. In other words, the droplet forms a minimal surface by forming a sphere; however, since the PDMS is weakly pinned to the glass substrate, a hemisphere forms instead. At this time, there may be air bubbles that form at the surface of the PDMS hemisphere. The bubbles are easily removed by taking a pair of sharp tweezers and picking them out of the PDMS droplet. We can then cure the PDMS by heating up the water bath by placing the bath in a 70°C oven for 4 hrs. Following this curing process, the hemisphere is taken out of the water bath and dried in an 110°C oven to remove the residual water. The crosslinked PDMS hemisphere is then used without further processing. This approach is based loosely on a similar approach developed by Whitesides and coworkers.[58] Our approach is simpler as we do not chemically modify the glass substrate with silanes. The advantage of using a silane surface is that the surface chemistry can pin the size of the PDMS droplet. Hence, by defining the diameter of the droplet with the silane along with controlling the droplet volume, the final curvature of the PDMS hemisphere can be easily adjusted. Alternatively, we are able to pin the PDMS droplet by first forming a crosslinked PDMS disk on the glass substrate and then subsequently forming the PDMS hemisphere on this disk (Fig. 2.25b). Other methods such as physical pinning of the PDMS droplet with a washer will also suffice.

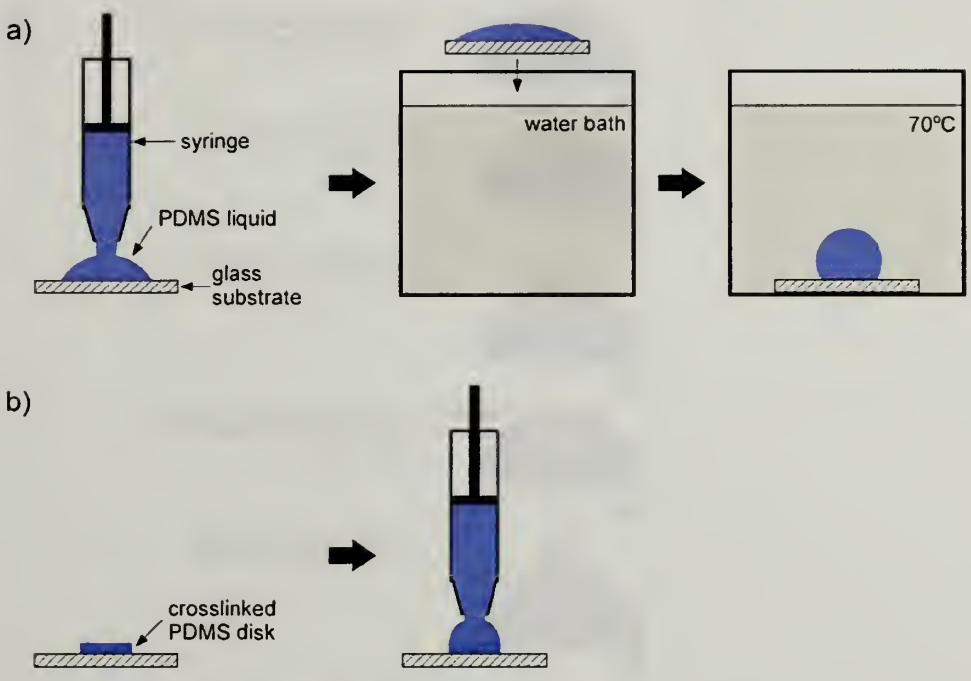

Figure 3.25 – Procedure for fabricating a PDMS hemisphere based on surface tension. This approach can be used to make PDMS hemisphere test probes for contact adhesion tests.

To develop the moduli-mismatch on the PDMS hemisphere surface, we again use a stencil mask to selectively UVO the surface. Due to the curvature of the hemisphere, it is difficult to use the TEM grid as a stencil mask. Instead, we transfer the hexagonal hole pattern of the TEM grid onto a positive photoresist (Shipley SPR 220, MicroChem Corp., Newton, MA) by UV photolithography and use this patterned resist as the stencil mask (Fig. 3.26).

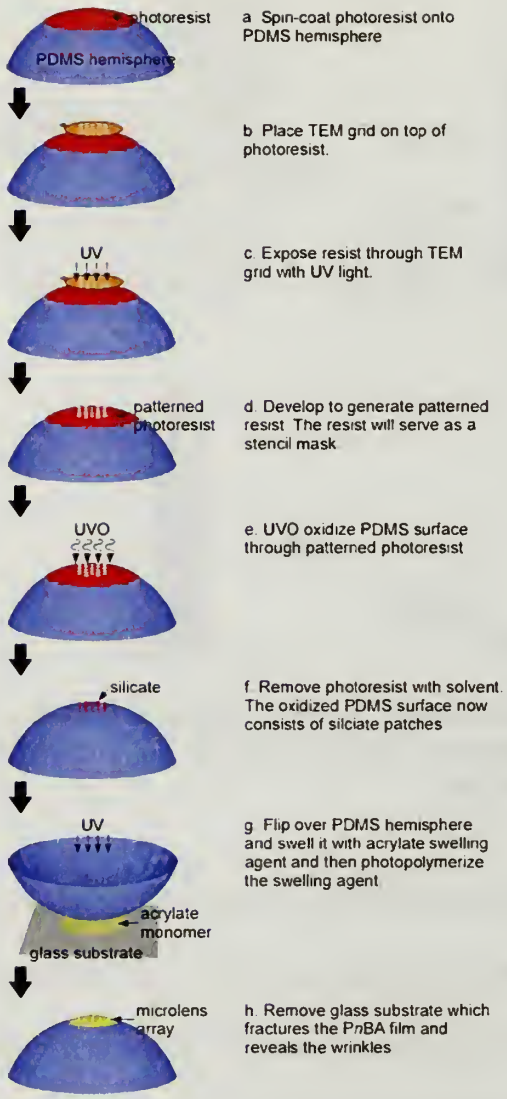

Figure 3.26 – Procedure for forming the compound lens.

The processing conditions for patterning the resist involves spin coating a thin layer of the resist solution onto the hemisphere surface (spin speed = 4000 rpm), pre-baking the resist at 95°C for 1 min. Following cooling of the resist, the TEM grid is placed on top of the resist and the entire assembly is irridated with UV (OAI, intensity = 20 MW/cm^2) for 45 s. The photoresist is then post-expose baked at 95°C for 60 s and developed for 2 min. in the SPR 220 developer (MF-319, tetramethyl ammonium

hydroxide) in order to strip away the exposed resist. Following patterning of the resist, the PDMS hemisphere is UVO oxidized and allowed to cool following oxidation. We then removed the remaining photoresist film by washing the PDMS surface with ethyl lactate (Sigma-Aldrich). Ethyl lactate is a solvent that dissolves the photoresist. If this solvent is not available, acetone or toluene can be substituted instead, these solvents simply require longer dissolution times. The subsequent swelling and wrinkling with the photocurable acrylate swelling agent is the same as described previously.

We use optical profilometry (Zygo NewView 6000, Mirau 50X objective, Zygo Corp., Middlefiled, CT) to confirm the successful patterning of the microlens array on the surface of the PDMS hemisphere (Fig. 3.24a, b). Additionally, we used stylus profilometry to further characterize the lenticular shape of a single microlens (Fig. 3.24c). For this system, the dimensions of the microlens are approximately 5 μm in height and 60 μm in width. However, as we illustrate with the planar microlens arrays, we can tune its radius of curvature simply by changing either or both the oxidation time and the lateral dimensions of the oxidized region.

3.5 Summary

In summary, surface wrinkling shares many similarities with the classic Euler buckling of a column. Similar to Euler buckling, surface wrinkling is a type of elastic instabiltity that leads to spontaneous formation of a characteristic buckled pattern of well-defined pattern length-scales. In general, wrinkling occurs as a result of the local bending of an interface. To develop the bending moment necessary for wrinkling, one

must create a stress difference or gradient within the material. Our approach to create local bending and thus, surface wrinkles is based on the swelling of a laterally-confined elastomer. Specifically, we UVO oxidize the surface of a PDMS elastomer to form a silicate-like skin layer. Upon swelling, a net compressive stress develops at the PDMS-silicate interface that drives wrinkle formation. The degree of lateral confinement is controlled by varying the stiffness of the silicate layer. We demonstrate experimentally that an increase in the silicate stiffness leads to an increase in the wrinkle wavelength. Besides tuning the wavelength, we provide a general strategy to generate oriented wrinkles. The orientation of the wrinkles is a result of the specific compressive stress state and we control the primary compressive stress direction through selective UVO treatment in order to create a surface with specified regions of moduli-mismatch. Due to the compressive stress discontinuity at the hard (oxidized PDMS)-soft (unmodified PDMS) boundary, the wrinkles orient normal to this boundary to form the aligned 1-D wrinkles. We find that the wrinkles align only over a finite distance which we define as the persistence length, ζ. By varying the degree of 1-D lateral confinement, we are able to experimentally determine the persistence length for our materials, which we find to be a function of the mechanical properties of the material.

Further confinement of the wrinkled region by limiting their growth in 2-D provides greater control over their formation to 3 distinct morphologies that includes 2-D isotropic wrinkles, dimples as well as microlenses. We demonstrate that the phase transitions between the 3 morpholgies are determined by the degree of lateral confinement as described by the confinement parameter, which is the ratio of the silicate plate diameter versus the persistence length (D/ζ). Low confinement ($D/\zeta > 1$)

leads to the formation of 2-D isotropic wrinkles. As we increase the extent of lateral confinement, the finite boundaries play a significant role in the wrinkle formation and leads to the generation of the dimple pattern ($D/\zeta \sim 1$) as well as the microlens structure ($D/\zeta < 1$). The versatility of our approach for microlens formation allows for the realization of a variety of functional devices on both planar and non-planar surfaces as demonstrated by the synthetic compound lens structures. Given our current material system, we are able to generate microlens structures on the micron length-scale. However, with the appropriate selection of materials, we believe that the general concept of lateral confinement of surface wrinkles can be extended to generating buckled structures on meso and nano length-scales.

Besides the application as an optical array, the well-defined patterns of the surface wrinkles can function as a patterned adhesive. In the next chapter, we explore how we can intelligently design a wrinkled patterned surface as a "smart" adhesive, i.e. an adhesive whose properties are determined by the dimensions of the patterns.

3.6 Acknowledgements

We thank Steve Koback, Amy McClung and Junstin Turner of Zygo Corporation for assistance and use of their optical profiler in characterizing the compound lens. We like to thank Andrew Smith for assisting in optical characterization of the microlens arrays and Jong-Young Lee for help with AFM measurements. We also acknowledge NSF-MRSEC Central Facilities for use of the SEM.

CHAPTER FOUR

SURFACE WRINKLES FOR SMART ADHESION

4.1 Introduction

Nature has demonstrated that surface patterns can be intelligently designed to control adhesion and release. For example, the attachment devices of geckos[8, 23] and some insects[59, 60] are decorated with fibrillar structures designed specifically for locomotion. Inspired by the fibrillar structures, there have been significant efforts in mimicking these structures[4, 12, 14, 16, 25, 61-63] to develop synthetic analogs as "smart" adhesives, i.e. where the geometry of the patterns can tailor the adhesion of the adhesive. However, there are two limitations in the current design of patterned adhesives. First, due to either materials selection or geometric design, their adhesive properties are not always reversible over the course of multiple attachment/detachment cycles.[14, 16, 25, 62] Second, as the current fabrication strategies are primarily based on lithographic or soft-lithographic approaches, there are issues related to the fabrication of these materials in an efficient and scaleable manner. These two issues must be addressed in order to successfully adopt these materials as "smart" adhesives.

In this chapter, we present an alternative design strategy for a reusable smart adhesive that uses surface wrinkles as patterns to control the adhesion of a poly(*n*-butyl acrylate) (P*n*BA) elastomer. The wrinkle patterning process is based on the swelling of a laterally confined polymer film. We demonstrate the ability to control the wrinkle dimensions as a simple approach to design a "smart" adhesive, where the control of adhesion is determined by the wavelength of the wrinkles based on a mechanism known

as contact splitting. Our materials design offers several advantages over previous approaches including: 1) enhanced control of adhesion provided by well-defined surface wrinkle patterns, 2) convenience and simplicity of the fabrication process without expensive lithography for patterning and 3) amenability to patterning a wide variety of polymer systems.

4.2 Experimental Approach

4.2.1 Fabrication of the Wrinkled Adhesive

Our wrinkled P*n*BA elastomer is fabricated using a "self-assembled" process based on surface wrinkling. As we have discussed in the previous chapter, the general prerequisite for surface wrinkling is the development of a critical compressive stress; hence, the formation of surface wrinkles has been observed for a variety of materials using different external stimuli. Similar to the previous chapter, we will use a combination of lateral confinement and osmotic pressure to generate the wrinkled adhesive. However, unlike our previous material, which is essentially a multi-layer composite of inorganic and polymeric materials, we will develop a more simplified all-polymer system. Specifically, we use a process that is loosely based on a wrinkling approach that was originally developed by Southern and Thomas[64] that is based on the swelling of a laterally-confined elastomer (Fig. 4.1a). The unique attribute in our approach is that we incorporate functionality to our swelling agent. In this work, we are essentially developing an interpenetrating elastomeric network (IPN) by our swelling and subsequent photopolymerization of the swelling agent. However, the potential for

additional functionality is unlimited. For example, we can take advantage of the diffusion profile to make a gradient IPN as a way to tune the mechanical and adhesive properties of the elastomer. Another possibility is to incorporate nanoparticles into the swelling agent to tune its optical properties as a simple method to make a graded refractive-index material, which is commonly used as anti-reflective surfaces.

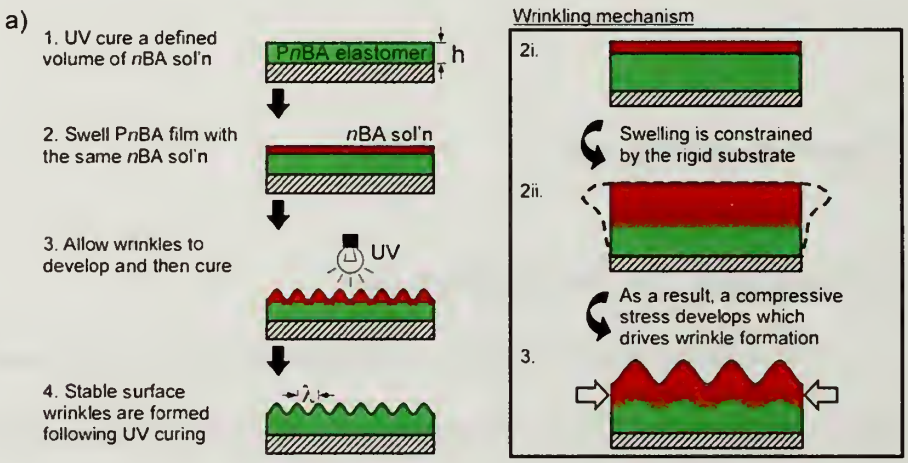

b)

*n*BA formulation		
Monomer	Crosslinker	Photoinitiators
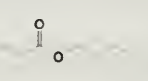	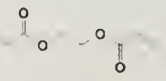	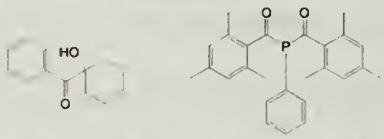
n-butyl acrylate (~98%)	ethylene glycol dimethacrylate (~2%)	Ciba® Irgacure® 183 / Ciba® Irgacure® 819

Figure 4.1 – Fabrication of the wrinkled P*n*BA adhesive. a) Experimental approach. b) The photocurable *n*BA formulation used.

4.2.1.1 P*n*BA Film Preparation

We begin by preparing a P*n*BA elastomeric film with defined film thickness, *h*. We use an *n*BA formulation that is similar to the one described in the previous chapter. The solution consists of 98 wt% *n*-butyl acrylate monomer (*n*BA), 2 wt% ethylene

glycol dimethacrylate crosslinker (EGDM) relative to the combined weight of the monomer and crosslinker. The two reagents are filtered through an alumina column which consists of a plastic syringe packed with alumina and the syringe opening is capped with a 0.2 μm PTFE filter in order to keep the alumina sand in place (and also to filter any dirt or dust particles present in the reagents). The main purpose of this filtering procedure is to remove the inhibitor that is present in the reagents. This step can be eliminated simply by increasing the concentration of the photoinitiators. The filtered reagents are combined and added to the 2 commercial photoinitiators (Ciba® Irgacure® 183 & 819) from Ciba Speciality Chemicals. The concentrations for both initiators are kept at 1 wt% relative to the weight of the monomer and crosslinker mixture. The final *n*BA solution yields a clear yellow, low viscosity liquid and is used without further modification. Since the solution is photoactive, we minimize their exposure to light as much as possible. The solution vial is covered with aluminum foil to prevent light exposure during use. When not in use, the solution is kept in an un-lit refrigerator, but any dark cabinet should suffice. To prepare the P*n*BA film, a controlled volume (from 0.1 and up to 0.2 mL) of the *n*BA solution is deposited onto a 2.5 cm x 2.5 cm glass coverslip. The solution is then cured by photopolymerizing the formulation with ultraviolet light (UV) using an OAI 500W DUV for 3 min. at an intensity ≈ 17 MW/cm^2 and a wavelength = 365 nm. As this film is immediately used as the wrinkling medium without further modification, hence, we do not know if the wrinkling process changes if we allow the film to sit for longer times. Typical with many cured materials, there is a fraction of linear chains or monomer (sol-fraction) that is present in the elastomer. The common procedure is to remove the sol-fraction by a simple sol-

extraction (i.e. swelling with toluene or any favorable solvent) or a more involved Soxlet extraction. Generally, a sol-extraction should suffice. The general procedure involves swelling the elastomer in an excess of filtered toluene (to remove dust) for 24 hrs, followed by extraction of the toluene solution and then replenishing with clean toluene. This procedure is repeated for a total of 3 times. For this work, we did not perform the sol-extraction since the process would lead to delamination of the film from the rigid glass substrate and prevent subsequent wrinkling by swelling.

4.2.1.2 Wrinkling of a Confined Layer by Swelling

Next, we swell the P*n*BA elastomer by depositing the same photocurable *n*BA solution onto the film surface. Specifically, we deposit ~0.1 mL of *n*BA solution onto the 2.5 cm x 2.5 cm freshly-prepared P*n*BA surface and swell the elastomer for a total of 3 min. The wrinkle formation occurs quite rapidly, in fact, wrinkles are already observed after ~1 min. of swelling.

The swelling occurs as a result of the competing interactions of swelling and lateral confinement. For an infinitely thick elastomer, the swelling simply leads to an overall dilation of the material. However, since the P*n*BA film is pinned to the rigid substrate, the lateral expansion of the polymer film is confined. This osmotic stress coupled with lateral confinement leads to the development of a net compressive force and the formation of an elastic instability, i.e. surface wrinkling.

Since an excess of the swelling agent remains on the film surface, we remove this excess after 2.5 min. of swelling by running a piece of Kim-wipe across the surface to absorb the excess. Following this brief swelling process, the wrinkled film is

irradiated with UV (OAI 500W DUV, intensity = 17 MW/cm^2) for 3 min., which photopolymerizes the swelling agent and stabilizes the surface wrinkles to form the wrinkled P*n*BA elastomer (Fig. 4.2). To fully cure the wrinkled P*n*BA, we perform an additional photocuring process. We irradiate the film with a high-intensity UV (UV Process Supply, Chicago, IL) for ~1 min. One important note is that the intensity of this UV lamp increases with time; at ~55s, the intensity is ~140 MW/cm^2. Following this final step, the wrinkled P*n*BA are used without further modification.

4.2.2 Morphological Characterization

To confirm the fabrication of a wrinkled P*n*BA surface, we again use the Zygo NewView 6000 3-D optical profiler, with a 50X Mirau objective, to characterize the surface topology (Zygo Corporation, Middlefield, CT). Fig. 4.2 represents the optical profile of the wrinkled P*n*BA surface.

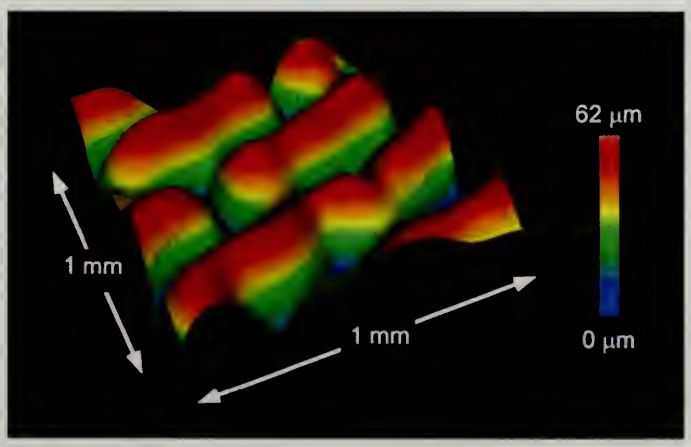

Figure 4.2 – Optical profile micrograph of the wrinkled P*n*BA.

For this sample, we evaporated a thin layer of Au/Pt onto the P*n*BA surface. The conditions for the evaporation procedure are similar to preparing a conductive sample

for SEM. Here, the purpose is to create a more reflective surface to improve the quality of the optical profile image since the uncoated P*n*BA samples are transparent.

We use bright-field optical microscopy to measure the thickness of the P*n*BA films (prior to swelling) and the wavelength of the wrinkles (after the wrinkling procedure). Specifically, P*n*BA film is measured by imaging its cross-section. A direct method in measuring the wavelength involves imaging the surface top-down with bright-field optical microscopy. Since it is necessary to obtain some statistics of the wavelength, a convenient approach is to use imaging software and take the Fast Fourier Transform (FFT) of the image. Alternatively, one can measure the wavelength over multiple wrinkles and obtain a statistical average. Another method involves measuring the wavelength by laser light diffraction, which is essentially another way of generating the reciprocal-space FFT image. For our materials, we measure the wavelength by taking a bright-field image and then taking statistical average by measuring multiple wrinkles. However, to ensure that we are measuring the wavelength correctly, i.e. measuring from peak to peak of the wrinkles, we actually use the micrographs taken from the contact adhesion tests (i.e. 1st micrograph in Fig. 4.4b where the probe is initially in contact with the wrinkled adhesive) to ensure correct measurements.

4.2.3 Tuning of Wrinkle Wavelength

The wavelength of the surface wrinkles is an important length-scale that provides adhesion control. Based on wrinkling theory for a soft, polymer gel, the wavelength, λ of the wrinkles is directly proportional to the film thickness, h, $\lambda \propto h$, since it is the only relevant length-scale. We validate this scaling in Fig. 4.3 and show

that λ is directly proportional to h. In addition, we demonstrate our ability to tune the wavelength of the wrinkle patterns. Here, h of the film can be easily defined by controlling the volume of *n*BA solution deposited onto the glass substrate.

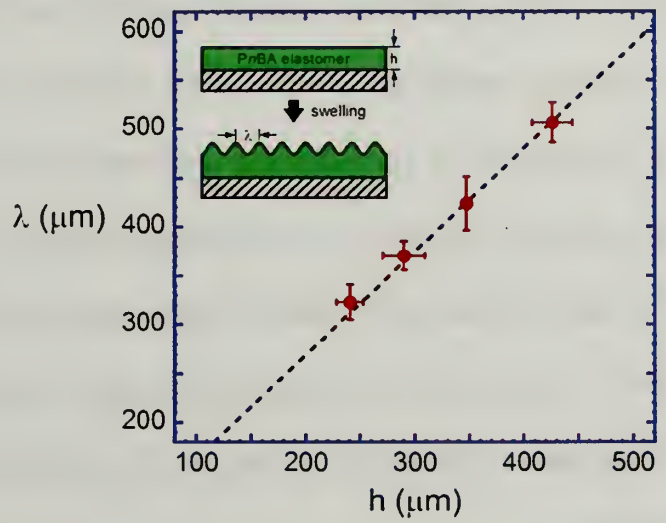

Figure 4.3 – Tuning of wrinkle wavelength, λ by controlling the initial thickness, h of the P*n*BA film. We define the film thickness experimentally by depositing controlled volume of the *n*BA sol'n onto the substrate to form the P*n*BA film. The dashed line illustrates the linear relationship between λ and h.

4.2.4 Contact Adhesion Test

Following fabrication of the wrinkled P*n*BA films, we quantify their adhesion using a custom-built contact adhesion test (CAT) instrument (Fig.4.4a). The CAT is an axi-symmetric probe-type test that measures the force, P, displacement, δ and interfacial contact area history, A by forming an interface (between the probe surface and the adhesive) and subsequently separating this interface. An example for the wrinkled P*n*BA is represented in Fig. 4.4b. Briefly, the test begins with forming the interface between the wrinkled adhesive and a flat-glass probe at a fixed displacement rate (~3 μm/s) controlled by a nanopositioner stepper motor. The adhesive is

continually compressed until it reaches a maximum compressive force, P_c, which corresponds to the establishment of a maximum interfacial contact area. Upon reaching P_c, the nanopositioner immediately reverses direction at the same displacement rate until complete interfacial separation occurs. To quantify the adhesion for our samples, we use two adhesion descriptors. The first is the separation strength, σ_s, which is the tensile force of separation, P_s normalized by the projected contact area, $A=\pi a_p^2$ that is defined by the flat probe of radius, a_p. The separation strength is a relevant descriptor of adhesion as it can be related to the materials' defined adhesion energy, G_c if the exact interfacial history can be defined. The second descriptor is the work of adhesion, W_{adh}. The work of adhesion is defined as the amount of energy dissipated required to form and fail the interface.

For P_c below a critical value, P_s depends upon P_c. This load-sensitive response observation is similar to the preload condition for fibrillar adhesives.[16, 25] Although this load dependence provides additional means to tailor adhesion and release, the advantages and mechanisms of this compressive load-dependent adhesion control is not discussed here. In this work, we focus on the adhesion of the wrinkled interface in the compressive load-independent regime.

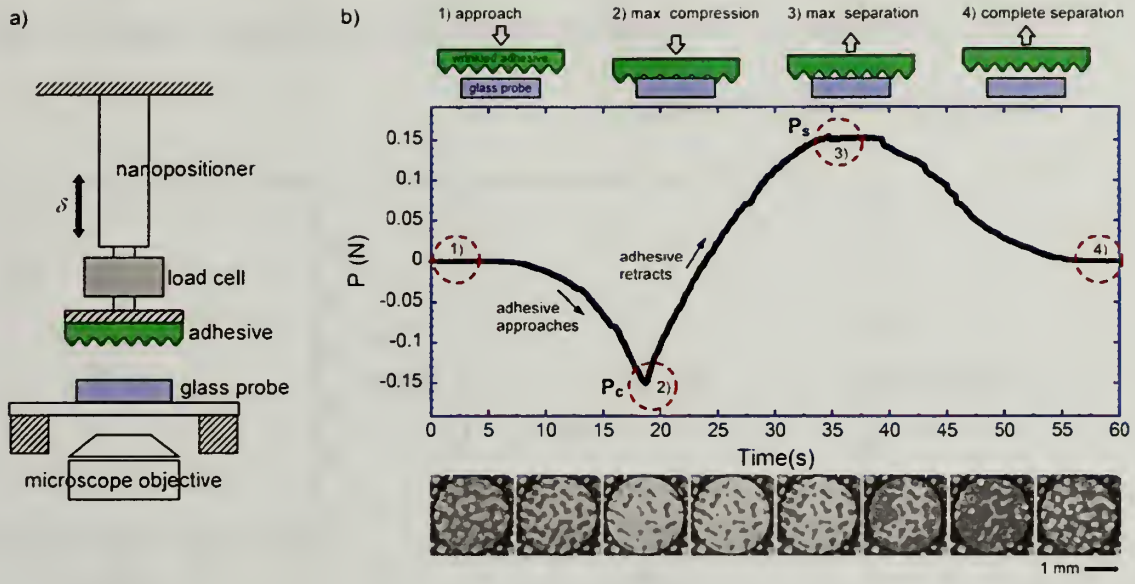

Figure 4.4 – The adhesion test used to measure adhesion of our materials. a) Contact adhesion test (CAT) used to measure the adhesion for the wrinkled P*n*BA adhesive as well as the smooth adhesive (that we use for comparison for the plots in Fig. 4.8). b) The force vs. time history for the contact adhesion testing of the wrinkled adhesive. The test begins with interface formation where the adhesive approaches the test probe and comes into contact. The adhesive is compressed until maximum compression (P_c,"-" force) is reached where complete interfacial contact is nearly established. Immediately following maximum compression, the adhesive retracts from the probe. Maximum separation force, P_s occurs when the highest tensile force ("+" force) is reached. The inset shows the side profile of the wrinkles at max. deformation illustrating that adjacent wrinkles do not self-adhere to increase true interfacial contact area. The test concludes when the adhesive and probe completely separate. The approach and retracting speeds are fixed at ~3 μm/s during the entire test. The optical micrographs illustrate the progression of interfacial contact between the wrinkled adhesive and the flat probe.

4.3 Results

A summary of σ_s and W_{adh} values obtained for our wrinkled P*n*BA is presented in Fig. 4.5a and b, respectively. The results demonstrate that the adhesion can be easily tailored by designing wrinkle patterns of specific wavelengths. Comparing the σ_s values between the wrinkled adhesive with the smallest wavelength ($\lambda \approx 325$ μm) to that of the

largest wavelength ($\lambda \approx 505$ μm), we show a three-fold increase in adhesion simply by changing the wrinkle wavelength.

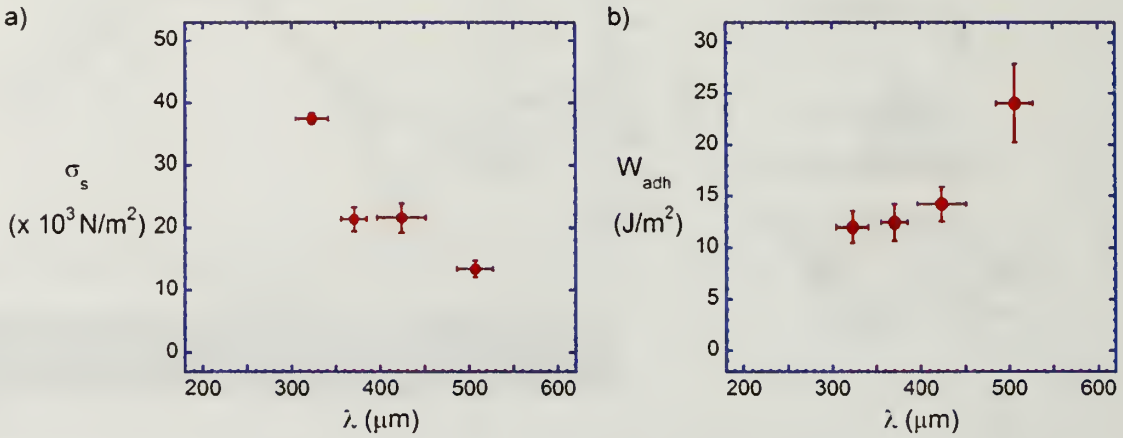

Figure 4.5 – Adhesion results from CAT. a) Strength and b) work of adhesion descriptors of the wrinkled P*n*BA as a function of the wrinkle wavelength.

4.3.1 Contributions to the Control of Adhesion

Using the previously described procedure, there are three possible contributions to the enhanced control of adhesion. The first contribution is related to the discretization of the interfacial contact. This mechanism, termed contact splitting, is determined by the pattern geometry and is discussed below. The second contribution is associated with changes in the P*n*BA material's properties. As our patterning approach involves swelling of the P*n*BA elastomer, the elastic modulus and adhesion energy may differ from the non-swollen P*n*BA. The third contribution is related to the thickness of the adhesive. For film thickness that are significantly smaller than its lateral dimensions, Crosby and co-workers have demonstrated that changes in the thickness of the adhesive can play a significant role in the separation mechanism and ultimately the adhesive

properties of the material.[65] As the wavelength of the wrinkles is controlled by the film thickness, the changes in thickness also contribute to the changes in adhesion.

4.3.2 Adhesion of Replicated Wrinkles

To isolate the effects of the wrinkle patterns, we make replicas of the wrinkled adhesives by micro-molding. The procedure is described below in Fig. 4.7. We begin by using the previously prepared elastic wrinkled P*n*BA films as the master templates. Daughter templates are constructed by depositing Norland Optical Adhesive 60 (NOA 60, Edmunds Optics, Barrington, NJ) optical liquid adhesive onto the master templates. The assembly is then irradiated by the high-intensity UV (UV Process Supply, Chicago, IL, max. intensity ~ 140 MW/cm^2) for ~1 min. which photocures the NOA 60 to form an optically transparent, rigid template. We remove this daughter template from the P*n*BA master and use it to mold the replicated P*n*BA by depositing the *n*BA formulation onto the template surface and then photopolymerized it by UV (UV Process Supply, max. intensity ~ 140 MW/cm^2) for ~1 min.

This procedure eliminates the adhesive contributions due to swelling and confinement effects due to thickness change since the materials' properties and thickness of the replicated P*n*BA are homogeneous. We again measure their adhesion using CAT and compare the adhesion between the replicated wrinkled P*n*BA against the smooth, non-wrinkled P*n*BA. The results are again presented as the separation strength, σ_s and work of adhesion, W_{adh} (Fig. 4.7).

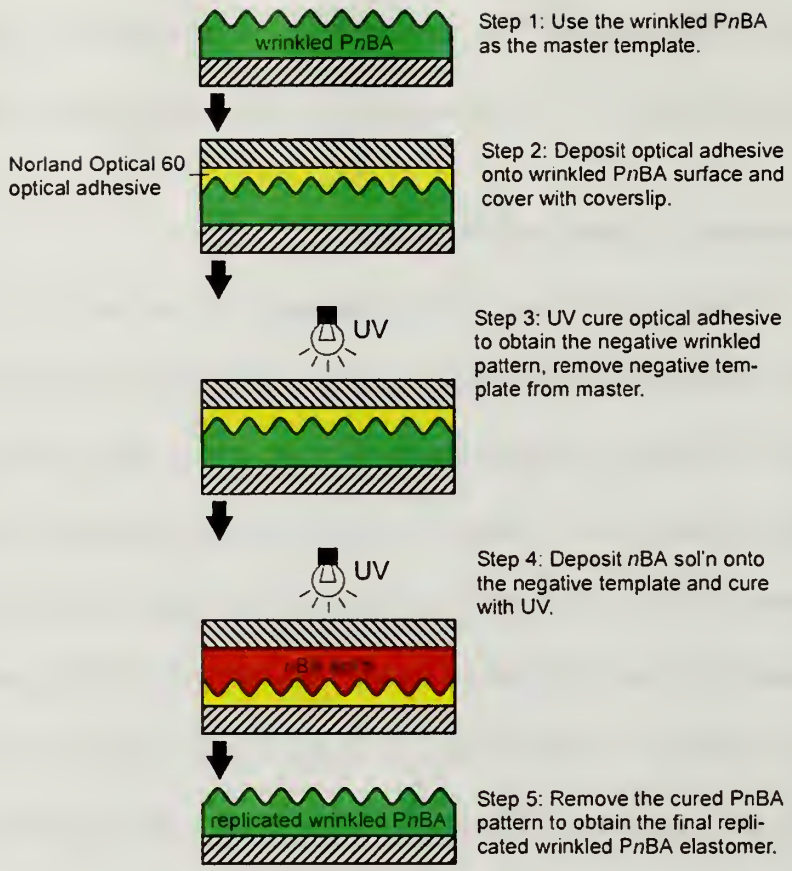

Figure 4.6 – Procedure for fabricating the replicated wrinkled P*n*BA adhesive.

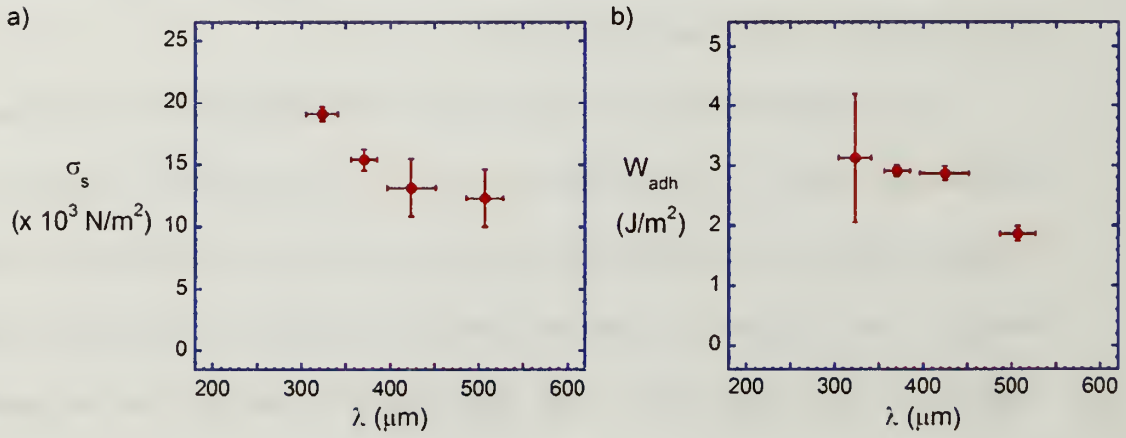

Figure 4.7 – Adhesion descriptors for the replicated wrinkled P*n*BA determined from CAT. a) Separation strength as a function of wrinkle wavelength. b) Work of adhesion as a function of wrinkle wavelength.

To determine the enhancement of adhesion by the wrinkle patterns, we compare the results from Fig. 4.7 with the adhesion of the smooth P*n*BA analog. The results are presented as normalized strength, $\overline{\sigma}_s$ and work of adhesion deseriptors, $\overline{W}_{adh}$ (Fig. 4.8).

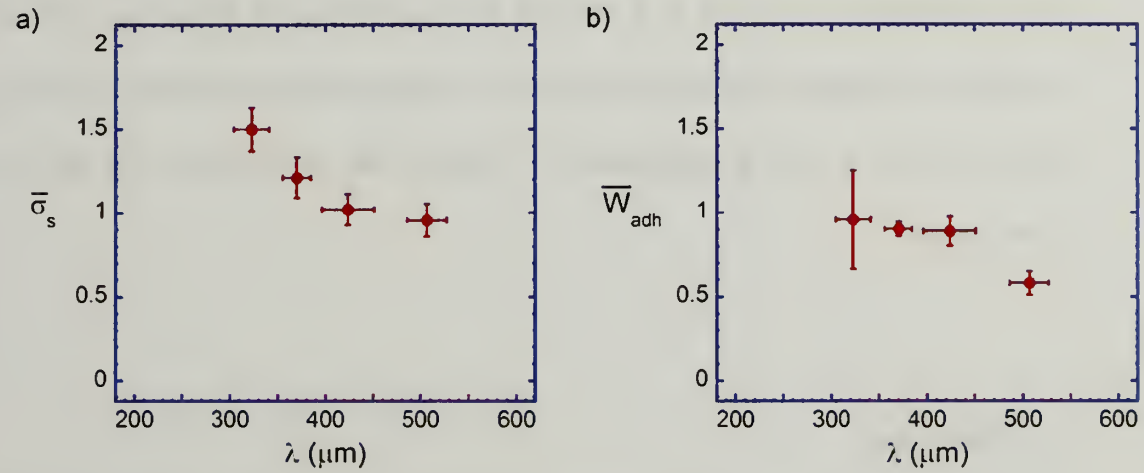

Figure 4.8 – Normalized adhesion descriptors. a) Normalized strength as a function of wrinkle wavelength. b) Normalized work of adhesion as a function of wrinkle wavelength. Both plots are determined by normalized the results from Fig. 4.7 with the results for the smooth P*n*BA.

We can make several comments based on these results. First, the wrinkle patterns do enhanee adhesion related to the non-wrinkled analog. In faet, for the wrinkled P*n*BA with the lowest wavelength, $\overline{\sigma}_s \approx 1.5$, indicating a 50% inerease in adhesion eompared with the non-wrinkled system. Seeond, for highest wavelength system, $\overline{\sigma}_s \approx 1$, in other words, no enhaneement oecurs. Third, the results indieate a trend and suggest that the enhancement in separation strength should seale inversely with wavelength. With regards to W_{adh}, there docs not appear to be any enhaneement at all rclative to the smooth for all wavelengths. An explanation for this result is associated with the important length-seale for the control of adhesion. As we diseuss in

the next section, while contact line is the important dimension of control for strength, contact area is the important dimension when considering separation energy (i.e. W_{adh}). Since the maximum contact area is reduced (in fact, area decreases as a function of increasing wrinkle wavelength) for a wrinkled surface relative to the smooth interface, this reduction in area leads to a decrease in W_{adh}. Hence, we focus our discussion on separation strength. In the following section, we discuss the mechanism of enhancement and develop a scaling relationship to define the contributions of the wrinkle wavelength.

4.4 Discussion

At one extreme, our wrinkled surface is analogous to a polymer film with a characteristic surface roughness. The effects of surface roughness on adhesion have been a constant theme for the past several decades. Previous work has shown that adhesion can be enhanced in some cases[66-68] and reduced in others[69, 70]. This control is directly related to the roughness length-scale as well as their height distribution, which leads to changes in the interfacial contact area. In other words, enhanced adhesion for rough surfaces has been linked to the enhancement in true interfacial area per projected area. In our materials, the maximum probe/adhesive interfacial area is fixed by the projected area defined by the rigid probe. Hence, the adhesive wrinkles do not form additional interfaces by folding upon each other as evidenced by the side profile of the contact history (Fig. 4.9).

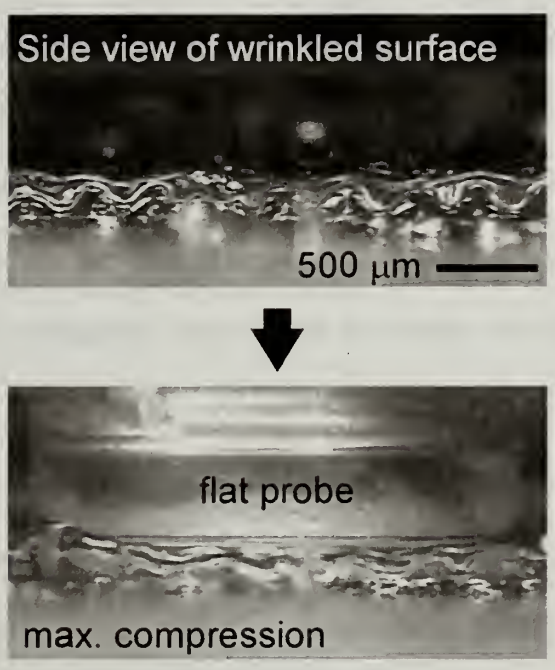

Figure 4.9 – Side profile of the wrinkles at maximum deformation. The profile illustrates that adjacent wrinkles do not self-adhere to increase true interfacial contact area.

This observation is consistent with previous predictions,[71, 72] and demonstrates that an increase in contact area is not a probable means of enhancement. Instead, the more relevant mechanism for our materials is not associated with an increase in contact area, but rather an increase in contact perimeter. The mechanism of enhancement by contact splitting has been described in Chapter 1. Similarly, our materials demonstrate a similar mechanism of enhancement where the geometry of the wrinkles contributes to the contact line splitting.

4.4.1 Contact Splitting by Surface Wrinkles

Similar to the fibrillar patterned surface of the gecko, it would seem counter-initiative to expect that surface wrinkles enhance adhesion since breaking up the contacts reduces the contact area. Although the contact area is reduced for a patterned

surface, its total contact line (defined by the sum contribution of the perimeter of each contact) can be increased provided the patterns are properly designed. This enhancement of increasing the total contact line with topographic patterns, referred as contact splitting, has been discussed in Chapter 1 and the mechanism was demonstrated by several research groups as the primary mechanism for the enhanced control of polymer adhesion.[4, 5, 10]

We can develop a simple scaling relationship that describes the contact splitting mechanism for our materials. For a smooth, non-patterned adhesive separating from a flat probe with radius, a_p, the maximum separation strength, $\sigma_{s,s}$ scales as:

$$\sigma_{s,s} = \frac{\left(8\pi E^* G_c a_p^{\,3}\right)^{1/2}}{\pi a_p^{\,2}} = \left(\frac{8E^* G_c}{\pi a_p}\right)^{1/2} \tag{4.1}$$

where the materials properties include the adhesion energy, G_c and the elastic constant, $E^* = E/(1-\nu^2)$ with E as the Young's modulus and ν as the Poisson's ratio. For a wrinkled interface where the multiple wrinkles are in contact with the test probe, i.e. $\lambda < a_p$, the separation process is illustrated in Fig. 4.10, where we use the scaling relationship developed by Groenewold[54] to approximate the geometry of each wrinkle as a cylinder with width, $\lambda/2$ and length,

$$\zeta = k_1 \cdot \lambda \tag{4.2}$$

The length, ζ is the persistence length for the wrinkle that we have discussed in Chapter 3. While we cannot quantatively define the proportionality constant, k_1 of our wrinkled P*n*BA, we can estimate this constant from the optical profile micrograph or from the bright field optical micrographs. Using the optical profile micrograph of Fig. 4.2, we estimate $k_1 \sim 1$.

For our wrinkled adhesives (inset, Fig. 4.10), local separation occurs by peeling along its edge or contact line, defined by its perimeter ($=\lambda+2\zeta$).

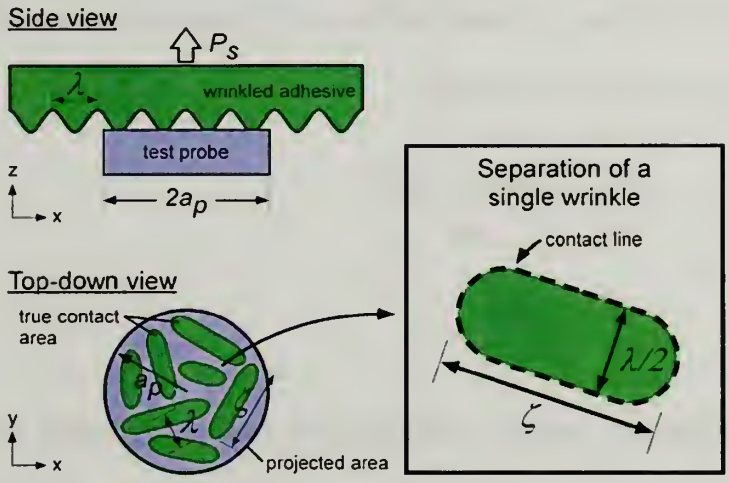

Figure 4.10 – Schematic of the interface during separation of the wrinkled adhesive from the flat probe. At P_s, only a selected portion of each wrinkle is in contact (side view). Hence, the true contact area consists of selected portions of the wrinkles in contact with the probe (top-down view). At separation, all the wrinkles separate simultaneously and the contribution from each wrinkle is determined by its contact line. As the inset illustrates, at separation, the contact line of a single wrinkle is defined by its perimeter, which is approximated as $\lambda+2\zeta$.

Therefore, the maximum separation force for a single wrinkle scales with the contact line (as defined by the perimeter of the wrinkle) and the adhesion energy of the interface:

$$P_{s,w} = G_c \cdot (\lambda + 2\zeta) \tag{4.3}$$

Since n wrinkles (each wrinkle area = $\zeta\lambda$) occupy within the project area (= πa_p^2) defined by the flat probe,

$$n = \frac{\pi a_p^{\,2}}{\zeta\lambda} \tag{4.4}$$

The total separation strength for n wrinkles ($\sigma_{s,n}$) simultaneously separating away from the probe surface is:

$$\sigma_{s,n} = n \cdot \left(\frac{G_c \cdot (\lambda + 2\zeta)}{\pi a_p^{\,2}} \right) \tag{4.5}$$

Substitution of Eqn. (4.2) and (4.4) into (4.5) leads to the separation strength scaling as a function of wrinkle wavelength.

$$\begin{aligned} \sigma_{s,n} &= \frac{\pi a_p^{\,2}}{\zeta \lambda} \cdot \left(\frac{G_c \cdot (\lambda + 2\zeta)}{\pi a_p^{\,2}} \right) \\ &= \left(\frac{1}{k_1} + 2 \right) \cdot \frac{G_c}{\lambda} \end{aligned} \tag{4.6}$$

By normalizing $\sigma_{s,n}$ with $\sigma_{s,s}$, we obtain the final dimensionless strength descriptor, $\bar{\sigma}_s$:

$$\bar{\sigma}_s = \left(1 + \frac{1}{2k_1} \right) \left(\frac{\pi}{2} \right)^{1/2} \cdot \left(\frac{a_p G_c}{E^*} \right)^{1/2} \frac{1}{\lambda} \tag{4.7}$$

This scaling relationship is represented as the curve in Fig. (4.11).

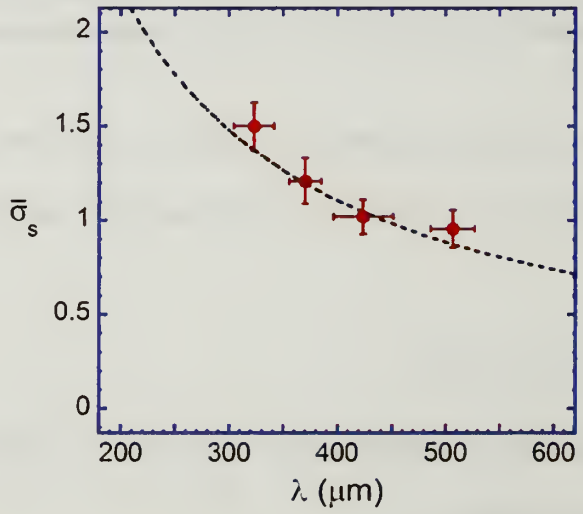

Figure 4.11 – Normalized separation strength results for the replicated wrinkles along with the scaling relationship based on Eqn. (4.7).

For materials with wrinkles significantly smaller than the probe size, i.e. $\lambda < a_p$, Eqn. (4.7) is particularly insightful since it suggests that the separation strength is

determined by the dimension of the wrinkles, λ. Therefore, the general strategy for adhesion enhancement is to reduce λ. This separation strength dependence with wavelength is precisely what is observed in our materials. Our empirical fit of the results (represented as the curve in Fig. 4.11) show that: $\bar{\sigma}_s \propto 1/\lambda$. This fit validites our scaling relationship (Eqn. (4.7)) and shows that separation strength scales inversely with wavelength. The prediction also suggests that the enhancement is unlimited provided we can generate smaller and smaller wrinkles. In practice, we encounter a lower wavelength limit, which is related to our materials approach. In an attempt to reduce the wrinkle wavelength by reducing the P*n*BA film thickness, we observe significant swelling that resulted in delamination of the swollen polymer film from the rigid substrate. The delamination can be avoided by improving the adhesion of the P*n*BA film to the rigid substrate, i.e. by covalently bonding the polymer-substrate interface.

4.4.2 Repeatable Adhesion

In addition to contact splitting enhancement, another unique characteristic of the gecko fibrillar structure lies in the ability to maintain consistent adhesion over many attachment/detachment cycles. However, repeatable adhesion is often a design challenge for synthetic patterned adhesives. For example, condensation or collapse of the fibrils is often observed an attachment/detachment cycles (Fig. 4.12). [14, 16, 25, 62] As a result, the efficiency for the patterns to contribute to contact splitting is lowered and hence, the adhesion is reduced.

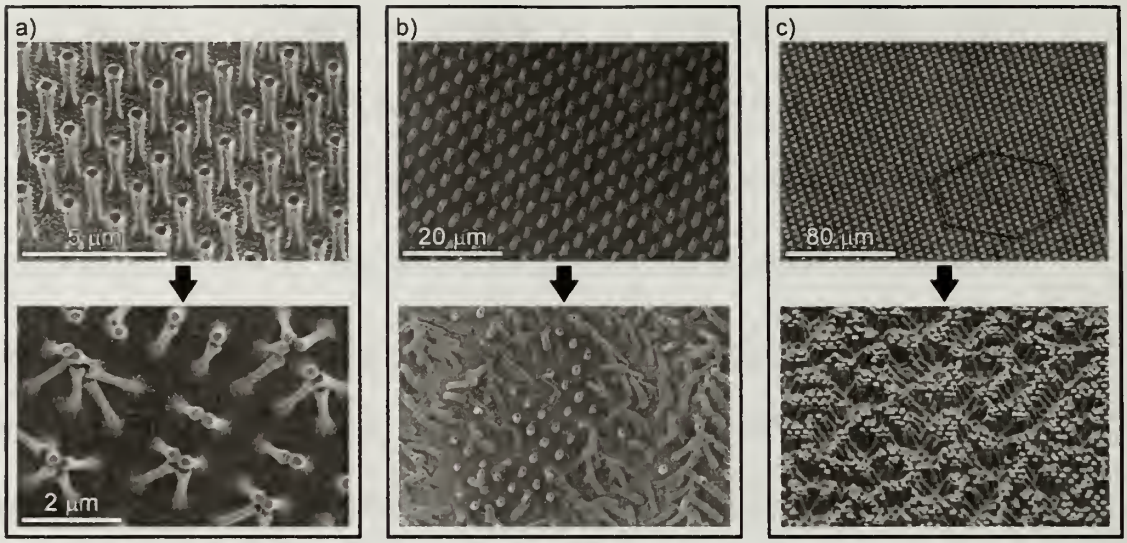

Figure 4.12 – Examples of fibril condensation in several patterned adhesive systems. Figures reproduced from a) Geim *et al.*[16], b) Glassmaker *et al.*[14], and c) Lamblet *et al.*[62]

In contrast, our materials demonstrate repeatability. We measure the separation force for the same region of the wrinkled P*n*BA over 10 attachment/detachment cycles. As Fig. 4.13 shows, the separation force is maintained over this cycling process and confirms our materials as a repeatable, "smart"adhesive.

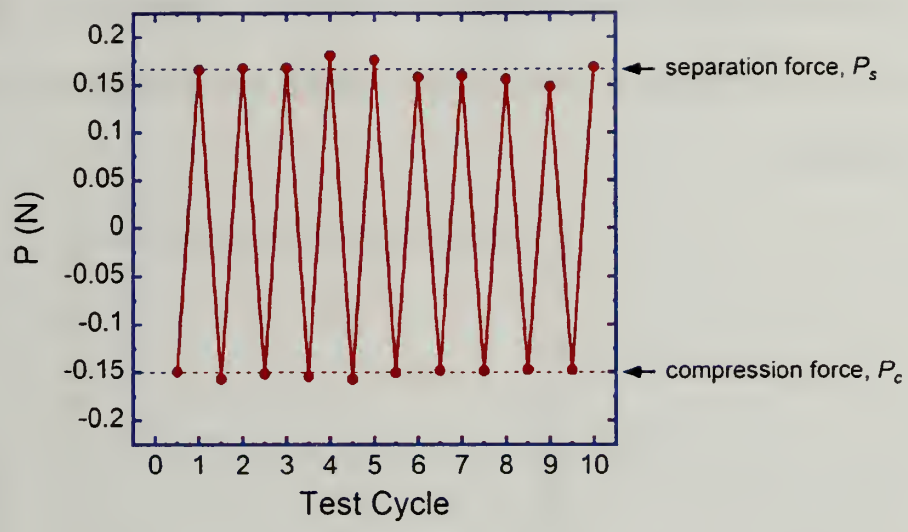

Figure 4.13 – Separation force as a function of adhesion test illustrating the reversible adhesion of the wrinkled P*n*BA. The results demonstrate repeatability in adhesion over 10 contact adhesion tests for the same region of the wrinkled surface where we compress the adhesive to the value of P_c and then measure the resultant separation force, P_s.

4.4.3 Viscoelastic Wrinkles

If repeatability is not required, the general strategy for surface wrinkled adhesives can be extended to materials with non-elastic, or viscoelastic contributions. In fact, these materials can prove useful in providing further increases in adhesion. As an example, we show in Fig. 4.14 the response for a viscoelastic wrinkled adhesive system. The material is chemically identical to the previously described P*n*BA elastomer, except that we purposely undercure the material to enhance its viscoelastic properties. The results again show an inverse scaling with wavelength; but more importantly, an even greater enhancement compared to our previously reversible wrinkled adhesive. In fact, we measure nearly a 7-fold increase in σ_s for the highest enhancement. However, this example is purely illustrative since the adhesion for this system is non-reversible, i.e. a one-time use adhesive. In addition, our current theory of contact splitting does not

account for other mechanisms of enhancement such as viscoelasticity. Future work will focus on developing a more complete theory that accounts for these additional mechanisms.

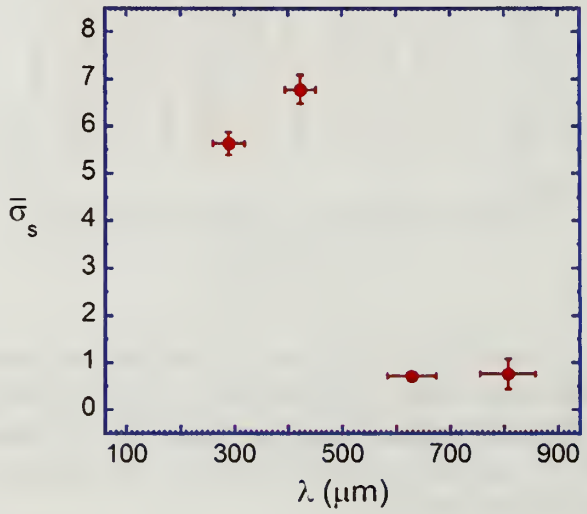

Figure 4.14 – The adhesion for the viscoelastic wrinkled P*n*BA adhesive as a function of wrinkle wavelength. We observe nearly a 7-fold increase in σ_s relative to the smooth P*n*BA for the highest enhancement.

4.4.4 The Design Envelope - Determining G_c and E^* of the P*n*BA elastomer

By rearranging Eqn. (4.7), we can develop a design envelope that establishes the critical wavelength, λ_c for enhancement and is defined solely by the contact radius, a_p and its materials properties:

$$\lambda_c = \left(1+\frac{1}{2k_1}\right)\left(\frac{\pi}{2}\right)^{1/2}\cdot\left(\frac{a_p G_c}{E^*}\right)^{1/2} \tag{4.8}$$

Therefore, the critical wavelength for enhancement is dependent on the materials of interest. To identify λ_c for our materials, we determine the G_c and E^* of our materials from the contact adhesion test. Fig. 4.15 is a representative result for the CAT of the smooth P*n*BA adhesive.

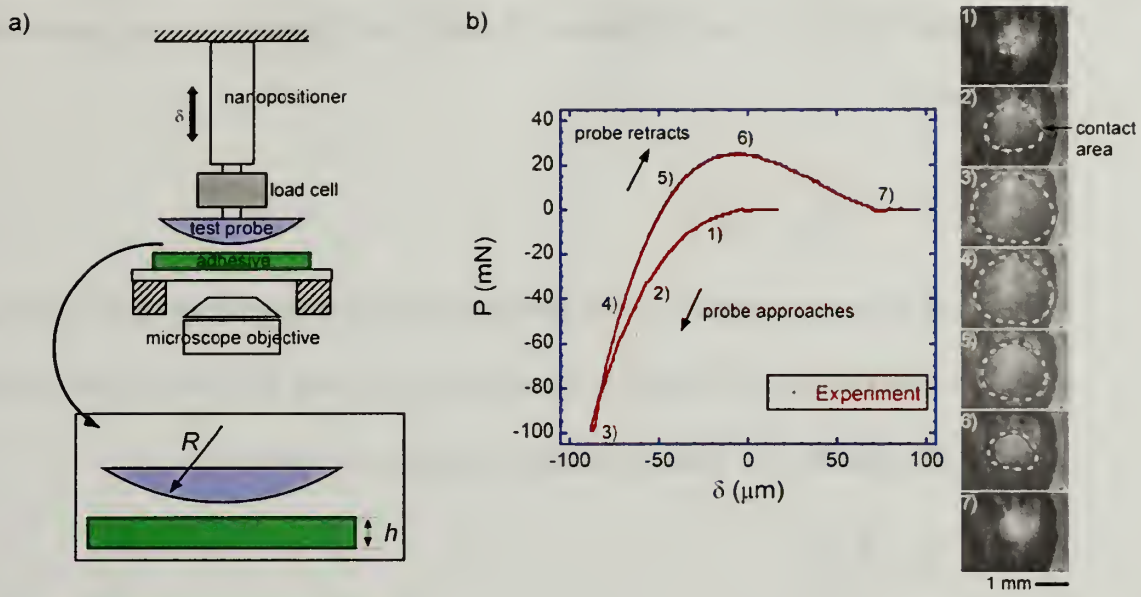

Figure 4.15 – Contact adhesion test (CAT) used to measure the adhesion of the smooth P*n*BA elastomer. a) We use a fused silica probe of radius of curvature, R = 5 mm for the tests. b) Force-displacement or "tack" curve for the smooth P*n*BA elastomer. The micrographs correspond to the interfacial contact history of the test, i.e. formation and failure of the interface.

Specifically, we use a fused silica hemisphere of radius of curvature, R = 5 mm, as the test probe (Fig. 4.15a). The testing conditions are identical to the CAT tests of the wrinkled P*n*BA. Again, we record the load, P, displacement, δ and interfacial contact area history of the entire test (Fig. 4.15b). We can determine G_c and E^* of the P*n*BA elastomer by using existing contact mechanics theory. We recommend the interested reader to refer to a review paper by Shull and co-workers on the adhesion of soft materials.[22, 73] Here, we will briefly go through the theory and show how it is implemented for our materials.

For a rigid hemisphere (of radius of curvature, R) in contact with a semi-infinitely thick, deformable elastomer, the compliance, C_o of this geometry (Fig. 4.16)

is equivalent to a flat, rigid, cylinderal flat punch (with diameter, *2a*) in contact with the elastomer.

$$C_o = \frac{1-\nu^2}{2Ea} = \frac{1}{2E^* a} \tag{4.9}$$

However, the contact radius, a for a hemisphere changes depending on the deformation; we can account for the change in contact area by using Hertzian contact mechanics theory. Specifically, the load, P_H and displacement, δ_H relationships are:

$$P_H = \frac{4}{3}\frac{E^* a^3}{R} \tag{4.10}$$

$$\delta_H = \frac{a^2}{R} \tag{4.11}$$

It is important to note that the Hertizan relationships refer to the contact between two surfaces in the absence of adhesion. Additionally, P, δ and C are not independent variables but at a fixed contact radius, a, are related by:

$$C = \left.\frac{\Delta\delta}{\Delta P}\right|_a = \frac{\delta_2 - \delta_1}{P_2 - P_1} \tag{4.12}$$

For an adhesive interface, the actual values of load and displacement will be quite different from the Hertzian values for a given value of a. To account for adhesion, we use the theory of Johnson, Kendall and Roberts (JKR) to describe the adhesion at the interface.[2] The JKR load, $P_{JKR} = P$, which describes the load due to adhesion, is related to the adhesion energy, G_c, E^* and a by the following:

$$G_c = \frac{(P - P_H)^2}{4\pi a}\frac{dC}{da} = \frac{\left(P - \frac{4}{3}\frac{E^* a^3}{R}\right)^2}{8\pi E^* a^3} \tag{4.13}$$

As an example, we can estimate the compliance from the load-displacement or 'tack' curve presented in Fig. 4.16. The slope of the linear portion of the tack curve is the stiffness or inverse compliance of the elastomer; between points 1 and 2, the deformation occurs at a fixed contact radius.

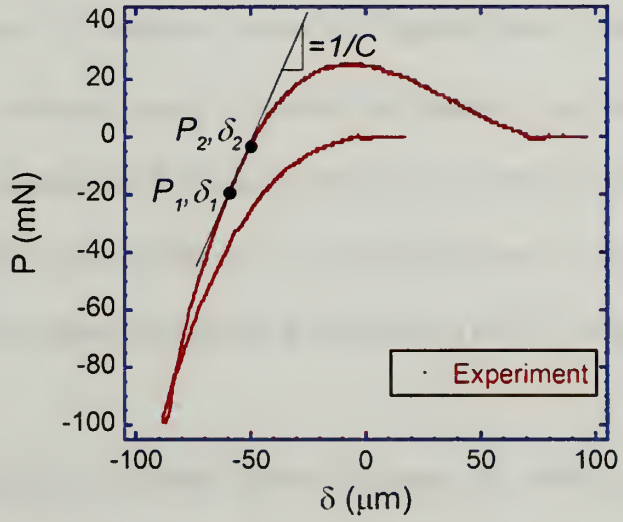

Figure 4.16 – Experimental measurement of compliance, *C* based on the results of the "tack" curve.

Qualitatively, we can assume that point 1 occurs in the absence of adhesion. To reach point 2, while maintaining the same contact radius, adhesion must be present. Hence, we can describe the load and displacement at point 1 using the Hertzian relationships and at point 2, we can use the JKR relationships. Eqn. (4.12) now becomes:

$$C = \frac{\delta_{JKR} - \delta_H}{P_{JKR} - P_H} = \frac{\delta - \delta_H}{P - P_H} \tag{4.14}$$

To determine the elastic modulus of the elastomer, we rearrange Eqn. (4.14) and substitute with Eqn. (4.10) and (4.11) to yield the following load prediction, P_{JKR}.

$$
\begin{aligned}
P &= P_H + \frac{1}{C}\cdot(\delta - \delta_H) \\
&= -\frac{4}{3}\frac{E^* a^3}{R} + 2E^* a \cdot \left(\delta + \frac{a^2}{R}\right) \\
&= 2E^* a \cdot \left(\delta + \frac{a^2}{3R}\right)
\end{aligned}
\tag{4.15}
$$

The procedure to determining E^* is to use the values of δ and a determined from CAT and determine the corresponding values of P using the above equation. A best fit to the experimental tack curve. The theory presented above assumes the adhesive to be semi-infinitely thick, where the thickness of the adhesive, h is significantly larger than the maximum contact radius (determined at maximum compressive force), a_{max}, i.e. $a_{max}/h \approx 0$.

For our P*n*BA elastomer, we cannot assume the thickness of the film to be semi-infinite since $a_{max}/h \approx 1.2\ mm/0.6\ mm \approx 2$. An adhesive is considered laterally confined when the thickness of film, h is significantly less than the contact radius, a.[65] During separation of the interface, the adhesive cannot relieve the lateral strains as it is pinned to the rigid substrate. As a result, a significant lateral stress develops in the adhesive that leads to the development of an overall triaxial stress. The change in the stress state will play an important role in the debonding mechanism of the adhesive. In order to relieve this stress, the adhesive will sometimes (depending on the degree of confinement and materials' properties of G_c and E) relieve this triaxial stress by developing an elastic instability such as fingering instabilities or cavitation. These modes of separation are more dissipative than simple interfacial separation. For example, most tapes are purposely designed to be thin in the thickness dimension to maximize their performance as the geometry facilitates the formation of fingering

instabilities, i.e. formation of fibrils, during peeling of the adhesive. For a more detailed understanding of these modes of separation, we recommend the reader to the work of Crosby and co-workers on the analysis of laterally confined adhesives.[65]

For an axi-symmetric probe-type test geometry such as our CAT, Crosby and co-workers have developed analytical corrections to the Hertian, compliance and JKR expressions to account for finite size effects.[65] The modified Hertizan relationships are:

$$P_H\left(a/h\right) = P_H\left(a/h = 0\right) \cdot f_p\left(a/h\right) = \frac{4}{3}\frac{E^* a^3}{R} \cdot \left(1 + 0.33 \cdot \left(\frac{a}{h}\right)^3\right) \tag{4.16}$$

$$\delta_H\left(a/h\right) = \delta_H\left(a/h = 0\right) \cdot f_\delta\left(a/h\right) = \frac{a^2}{R} \cdot \left(0.4 + 0.6 \cdot exp\left(-1.8\frac{a}{h}\right)\right) \tag{4.17}$$

The modified compliance relationship is:

$$C\left(a/h\right) = C_o \cdot f_C\left(a/h\right) = \frac{1}{2E^* a} \cdot \left(1 + \left(\frac{0.75}{\left(\frac{a}{h}\right) + \left(\frac{a}{h}\right)^3} + \frac{2.8 \cdot (1 - 2\nu)}{\left(\frac{a}{h}\right)}\right)^{-1}\right)^{-1} \tag{4.18}$$

Assuming that the material is incompressive, i.e. Poisson's ratio, $\nu = 0.5$, then, Eqn. (4.18) simplifies to:

$$C\left(a/h\right) = \frac{1}{2E^* a} \cdot \left(1 + 1.33 \cdot \left(\frac{a}{h}\right) + 1.33 \cdot \left(\frac{a}{h}\right)^3\right)^{-1} \tag{4.19}$$

Accounting for confinement by subsitituting Eqn. 4.27, 4.28 and 4.29 into 4.26, the modulus fit expression now becomes:

$$\begin{aligned} P &= P_H\left(a/h\right)+\frac{1}{C}\cdot\left(\delta-\delta_H\left(a/h\right)\right) \\ &= -\frac{4}{3}\frac{E^* a^3}{R}\cdot f_p\left(a/h\right)+\frac{2E^* a}{f_C\left(a/h\right)}\cdot\left(\delta+\frac{a^2}{R}\cdot f_\delta\left(a/h\right)\right) \\ &= \frac{2E^* a}{f_C\left(a/h\right)}\cdot\left(\delta+\frac{a^2}{R}\cdot\left(f_\delta\left(a/h\right)\right)-\frac{2}{3}\cdot f_P\left(a/h\right)\cdot f_C\left(a/h\right)\right) \end{aligned} \tag{4.20}$$

We use Eqn. (4.20) to determine the Young's modulus E^* of the P*n*BA elastomer. Specifically, we predict the load, P at a given displacement, δ by substituting into the Eqn. (4.20) the experimentally measured values of δ and a along with the constants R = 5 mm, h = 0.6 mm and ν = 0.5. The E^* of the material is determined by the best fit of the tack curve, i.e. where the fit superimposes onto the experimental result as shown below (Fig. 4.17). For our materials, we determine $E^* \approx 1.2 \times 10^5$ N/m^2 based on the best fit of the tack curve.

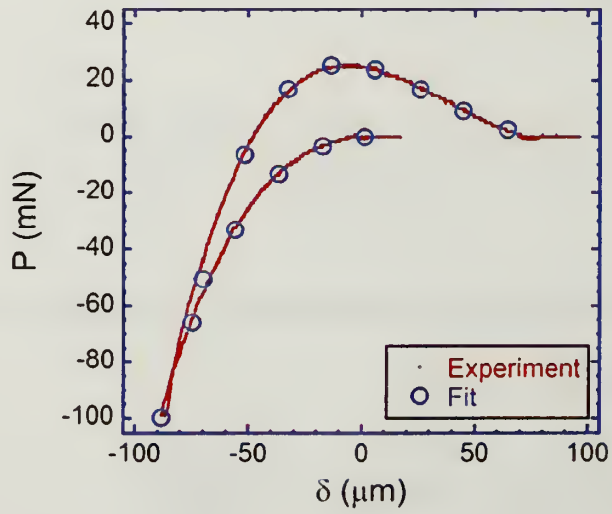

Figure 4.17 – Force-displacement or "tack" curve for the P*n*BA elastomer measurement by the CAT of the smooth P*n*BA.

Similarly, we need to account for confinement effects when determining the adhesion energy, G_c. Subituting Eqn. (4.16) and (4.18) into the energy release rate relationship from Eqn. (4.13), we obtain the following:

$$G_c\left(a/h\right) = \frac{\left(P - P_H\left(a/h\right)\right)^2}{4\pi a}\frac{dC\left(a/h\right)}{da}$$

$$= \frac{3\cdot\left(P - \frac{4}{3}\frac{E^* a^3}{R}\cdot f_P\left(a/h\right)\right)^2}{8\pi E^* a^3}\cdot\left(\frac{3+4\cdot\left(2\cdot\left(\frac{a}{h}\right)+4\cdot\left(\frac{a}{h}\right)^3\right)}{\left(3+4\cdot\left(\left(\frac{a}{h}\right)+\left(\frac{a}{h}\right)^3\right)\right)^2}\right) \qquad (4.21)$$

We take our previously determined value of E^*, along the experimental values of P, a and constants of R and h, to determine the G_c of the elastomer. Fig. 4.18 is a plot of G_c as a function of a.

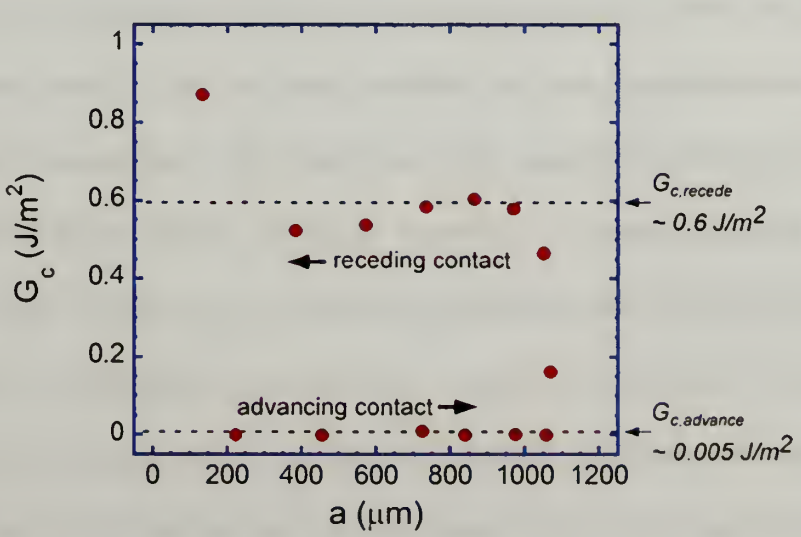

Figure 4.18 – Determination of the G_c for our P*n*BA elastomer based on extrapolation of the $G_{c,recede}$ vs. a plot.

In general, G_c is a materials' property that quantifies the amount of energy needed to drive crack forward a distance a. In the contact adhesion test, when the amount of applied energy $G_{applied}$ reaches G_c, the crack will advance. Hence, we are determining G_c indirectly by measuring $G_{applied}$, i.e. we assume $G_c = G_{applied}$. For an interface (formed by material A and B) that is separating under true thermodynamic equilibrium, there should be one value of G_c and the value should be equivalent to the thermodynamic work of adhesion, w:

$$w = \gamma_A + \gamma_B - \gamma_{AB} \tag{4.22}$$

where γ_A and γ_B correspond to the surface energies of material A and B, respectively and γ_{AB} is interfacial energy for an A/B interface. In theory, regardless of whether the crack is advancing (the contact radius grows with time) or receding (the contact radius reduces with time), the value of G_c should be a constant for a thermodynamic system. However, since polymers are generally viscoelastic materials, G_c does not correspond to the thermodynamic work of adhesion since the test is rarely performed under true thermodynamic conditions. More importantly, the receding and advancing values of G_c will be very different for polymers. Generally, the advancing contact G_c, $G_{c,advance}$ is significantly less than the receding contact G_c, $G_{c,recede}$ and the value of w sets the upper and lower bounds for $G_{c,advance}$ and $G_{c,recede}$, respectively. In other words, for a dissipative material, the formation and failure of an interface is an irreversible process and will result in an energy penalty that is not recoverable. For our materials, $G_{c,advance}$ is ~0.05 J/m^2, which is slightly greater than the work of adhesion for typical acrylate elastomers. We take the $G_{c,recede}$ value (~0.6 J/m^2) as the value of G_c for our P*n*BA elastomer since this value corresponds to the energy required for separation.

With the materials' properties determined by our adhesion tests, a_p = 1.2 mm, G_c = 0.6 J/m^2 and E^* = 1.2 x 10^5 N/m^2, and assuming the k_1 = 1, we find that $\lambda_c \approx 150$ μm for our materials. As a first approximation of the critical length-scale for enhancement, this prediction is comparable with our experimental results (Fig. 4.11). More importantly, it demonstrates that our simple scaling relationship predicts quite well the critical length-scale of adhesion control for wrinkled interfaces. Therefore, for enhancement to occur (i.e. $\overline{\sigma}_s > 1$), one must design a wrinkled surface with $\lambda < \lambda_c$. Provided that one can overcome the fabrication issues, our theory predicts that the enhancement in adhesion for a wrinkled interface is inversely proportional to λ. When $\lambda > \lambda_c$, a wrinkled surface does not increase adhesion but rather enhances release (i.e. $\overline{\sigma}_s < 1$). The result is again attributed to the changes in contact line, whereby for sufficiently large wrinkles, the total contact line per area becomes less than that of the smooth non-wrinkled case. For wrinkles that are significantly greater than the probe size, i.e. $\lambda >> a_p$, both wrinkled and smooth adhesive will have similar adhesion since the dimensions of the probe size now defines the interfacial contact.

4.5 Summary

In summary, we have demonstrated a unique design of a repeatable, "smart" adhesive. Our strategy to generating a patterned adhesive by surface wrinkling is elegant and highly scaleable. Since our wrinkling approach is based on the swelling of a laterally confined polymer film, the process is amenable to a variety of polymers and swelling agents. The demonstrated enhancement is determined by the length-scale of

the wrinkle patterns and is associated with the changes in the contact line during release. The critical wrinkle wavelength for enhancement, λ_c, is materials-defined. Enhanced adhesion occurs when the wavelength of the wrinkles is sufficiently small to increase the total contact line per area, i.e. $\lambda < \lambda_c$. Given our current materials system, the enhancement of adhesion is limited to the smallest wrinkle wavelength we are able to generate reliably. However, with the appropriate choice of materials, our general fabrication strategy can be extended to generating smaller wavelength structures that can provide even greater enhancement.

4.6 Acknowledgements

We thank Justin Turner and Steve Koback of Zygo Corporation for assistance and the use of the Zygo NewView 6000. We also thank REU Erica J. Smith for initial work on the creation of the wrinkled adhesives and preliminary adhesion measurements of the materials. We also acknowledge Prof. Ryan C. Hayward for helpful discussions.

APPENDIX A

QUANTIFYING RELEASE IN STEP-AND-FLASH IMPRINT LITHOGRAPHY

A.1 Introduction

Nanoimprint lithography (NIL)[74-76] and step-and-flash imprint lithography (S-FIL)[77, 78], constitute the two principal imprint-based lithographic technologies capable of replicating sub 10 nm features in a low cost and high throughput manner. Compared with the current photolithographic technologies, where the feature resolution is limited by the constraints of diffraction and scattering of incident light, imprint-based approaches are devoid of these limitations as the process does not rely on complex exposure optics.[79] The principle behind these imprint-based techniques is similar: a rigid, imprint template containing topographic features is used to pattern a thin film by mechanical deformation of the film at controlled temperatures and pressures. This film will serve as an etch barrier during subsequent transfer of the pattern into the underlying substrate. In the NIL approach, a glassy polymer is used as the patterned material. The embossing is performed at elevated temperatures (above the thermal transition of the polymer) and at pressures greater than 10 N/m^2.[74] S-FIL differs from NIL as it uses a low viscosity photopolymerizable monomer solution rather than a glassy polymer to form the etch barrier; hence, there are no issues with patterning isolated recessed features which is often difficult to generate in NIL.[80] This makes S-FIL an attractive nanofabrication alternative as the imprinting can be performed at room temperatures and at low pressures over large areas.

In a typical S-FIL process, a low viscosity photopolymerizable monomer solution is deposited onto a planarized substrate.[78] An imprint template is then brought into contact with the substrate, and capillary pressure ensures that the monomer formulation completely fills the features of the template. Ultraviolet light (intensity ~20 mJ/cm^2) is illuminated through the backside of the template which polymerizes and crosslink the monomer solution, thus forming the etch barrier layer. Finally, the template is separated from the cured polymer layer revealing the negative image of the template's pattern on the polymer surface. Further chemical processing of this patterned substrate by reactive ion etch transfers the pattern onto the underlying layer.

The release of the template from the cured, patterned polymer is a vital step in the S-FIL process. Following the illumination and subsequent curing of the photopolymer, it is crucial that the etch barrier layer remains adhered to the underlying transfer layer and releases cleanly from the imprint template. The consequence of an imperfect release is two-fold. First, improper release of the polymer film from the template creates defects in the etch barrier layer. Subsequent processing to transfer the pattern onto the underlying layer will amplify these defective features and render the pattern unusable. Second, any residual photopolymer that remains on the template from a previous incomplete release creates defects in subsequent imprinted patterns. Therefore, to minimize defects, the release characteristics must be properly understood and carefully controlled to ensure proper release of the etch barrier from the template. While several groups are designing new surface chemistries for the template to minimize defect generation, the mechanism of release in this application is not well understood and a standard metrology is required for future materials development. In

this paper, we provide 1) a metrology to quantify the stress development during the imprinting process and 2) an illustration of how the template's materials properties control the release behavior.

A.2 Experimental Approach

A.2.1 Photopolymerizable Monomer Formulation

We use an acrylate formulation consisting of 3 components (Table A.1): 75 wt% of 2-hydroxyethyl acrylate monomer (HEA), 1 wt% of two photoactive initiators (Irgacure 184 and 819) and 25 wt% of ethylene glycol dimethacrylate (EGDM) serving as the crosslinker. Both the monomer and the crosslinker, purchased from Sigma-Aldrich, are filtered through alumina columns to remove the inhibitors prior to use. The photoactive initiators are acquired from Ciba-Giegy Specialty Chemical Divisions. The components are then combined to yield a clear bright yellow low-viscosity liquid.

Monomer	Crosslinker	Photoinitiators	
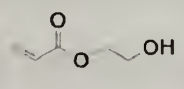	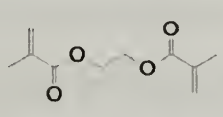	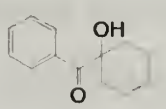	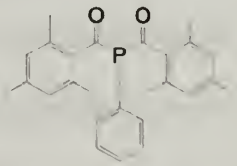
2-hydroxyethyl acrylate (~75%)	ethylene glycol dimethacrylate (~25%)	Ciba® Irgacure® 183 (1%)	Ciba® Irgacure® 819 (1%)

Table A.1 – The photocurable acrylate formulation used for imprinting.

Again, the solution is light-sensitive, therefore, care must be taken to minimize light exposure. This specific formulation was chosen as it does not swell the soft templates

(described below) in a noticeable manner. Other acrylates, such as *n*-butyl acrylate, may cause excessive swelling in soft templates, which can lead to template distortion and undesired but interesting wrinkling patterns as presented in Chapter 4. As a side note, this paper initiated a lot of my Ph.D. work on wrinkling. The specific conditions used to form the surface wrinkles in Chapter 4 were developed in this work where we were designing a surface modified PDMS template by UVO (described below).

A.2.2 Template Fabrication and Materials Properties

To demonstrate the impact of template materials properties, we replace the conventional rigid quartz template of S-FIL with 3 soft, polymer-based templates in our imprinting experiments. We refer to these 3 templates as PDMS, PDMS-u and NO60-p. PDMS is a soft, crosslinked poly(dimethyl siloxane) made from commercially-available Dow Corning Sylgard® 184. PDMS-u is PDMS that is exposed to ultraviolet/ozone (UVO) for 15 minutes to oxidize the surface and near-surface molecules. NO60-p is fabricated from commercially-available Norland Optical 60 (Edmunds Optics), an optical adhesive that photopolymerizes to produce a rigid, optically-transparent solid. Each template is fabricated through a molding process from an etched silicon pattern master template (Fig. A.1). For the PDMS templates, an uncured mixture is poured onto the master template and subsequently cured. Following curing, the daughter templates are removed from the master. No further processing is conducted for the PDMS templates prior to imprinting. For the PDMS-u templates, the daughter PDMS template is exposed to UVO for 15 minutes prior to imprinting. For the NO60-p template, a thin layer of Sylgard 184 is spun-coated onto the NO60 and cured at 110°C for 1 hr. This

step is performed to ensure similar surface properties as the PDMS template. To verify that the NO60-p is indeed coated with PDMS, and therefore have similar surface properties as PDMS, we measured the static contact angle for the templates by using the acrylate formulation as the wetting liquid (Table A.2) – i.e. a liquid with EHA and EGDM.

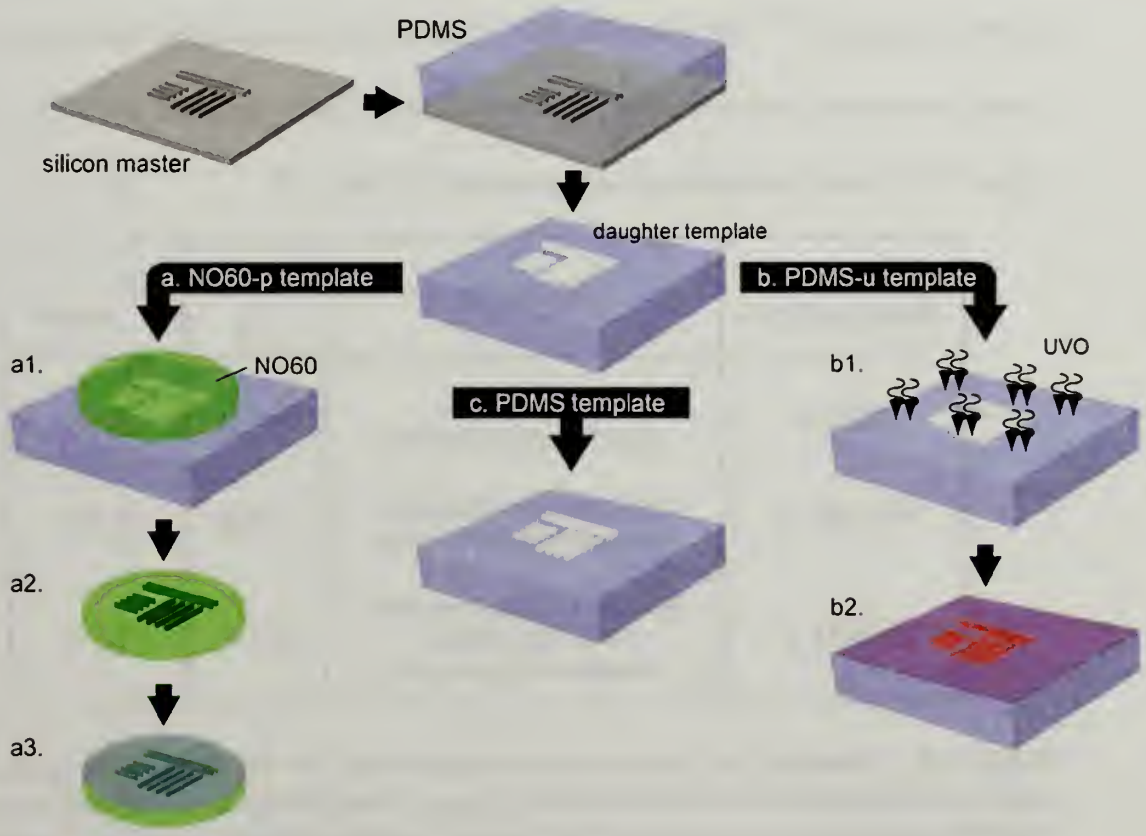

Figure A.1 – Fabrication procedure for the three templates. In all cases, we use the etch Si as the master template to prepare the daughter templates to facilitate subsequent pattern transfer into other materials. a) The NO60-p template procedure. a1) The NO60-p is fabricated by depositing the liquid Norland Optical 60 adhesive onto the daughter template, and a2) then curing the optical adhesive to form the rigid NO60 template. a3) Finally, the surface of the template is coated with a thin layer of PDMS by spin-coating Sylgard 184 (10:1 base to curing agent) onto the template surface and then curing the PDMS at 110°C. b) The PDMS-u template procedure. b1) We take a PDMS daughter template and UVO oxidize the surface for ~15 min. b2) This causes a change in near-interfacial properties of the template since a silicate-like skin layer develops. c) The PDMS template is simply a daughter template.

The Young's moduli of the template materials are measured using contact mechanical tests involving the contact and subsequent separation of a hemispherical lens (fused silica, R = 5 mm) with the substrate (the template material) at a controlled separation rate.[81] The displacement, δ, force, P and contact area, $A=\pi a^2$ are recorded simultaneously and allow for the determination of the Young's modulus, E of the template materials.[73] The determination of the elastic modulus from the results of the contact mechanical test (or contact adhesion test) has been discussed in Chapter 4. The values of the elastic modulus are also presented in Table A.2.

Template designation	Material	θ_{static} (°)	$E^*_{template}$
PDMS	crosslinked poly(dimethyl siloxane)	61.0	0.75
PDMS-u	UVO-oxidized crosslinked poly(dimethyl siloxane)	35.0	0.78
NO60-p	Norland Optical 60 coated with crosslinked poly(dimethyl siloxane)	61.0	10.5

Table A.2 – Summary of the template designation for the three templates along with the materials of the three different types of templates; also included are static contact angle measurements and the Young's moduli of the templates. The contact angle measurements are performed using the acrylate formulation as the liquid probe. The Young's moduli for the three templates are determined using contact mechanical tests.

Accordingly, this template library is used to demonstrate the importance of both surface and bulk properties on the imprinting process and associated defect generation. The PDMS and PDMS-u template have identical bulk properties but different surface

properties. The PDMS and NO60-p properties have identical surface properties but different bulk properties.

A.2.3 Imprinting Procedure

The imprinting experiments are performed with a custom-built imprinting instrument (Fig. A.2). The imprinter consists of 4 components: 1) an inverted optical microscope (Zeiss Axiovert 200M) to record contact area images as well as provide a platform stage for securing the imprint template, 2) a load cell (Honeywell Sensotec Sensor Model 34, 1kg) that monitors stress development during the imprinting process, 3) a nanopositioner (Burleigh EXFO IW-812) which controls and monitors the displacement between the imprint template and the superstrate and 4) a computer that interfaces all hardware components. The entire experiment is controlled and monitored through a custom-designed National Instruments LabVIEW® interface. Unlike other S-FIL imprinters, our mold template is actually the substrate. Additionally, we use a hemispherical superstrate as opposed to a planar one. This solves many of the mis-alignment issues encountered in current S-FIL imprinting processes, where due to mis-alignment between the substrate and superstrate, there is thickness variation across the molded polymer film. As demonstrated by Crosby and co-workers on the effects of film thickness on polymer adhesion[65], this thickness variation will have a profound influence on the separation mechanism of the polymer film.

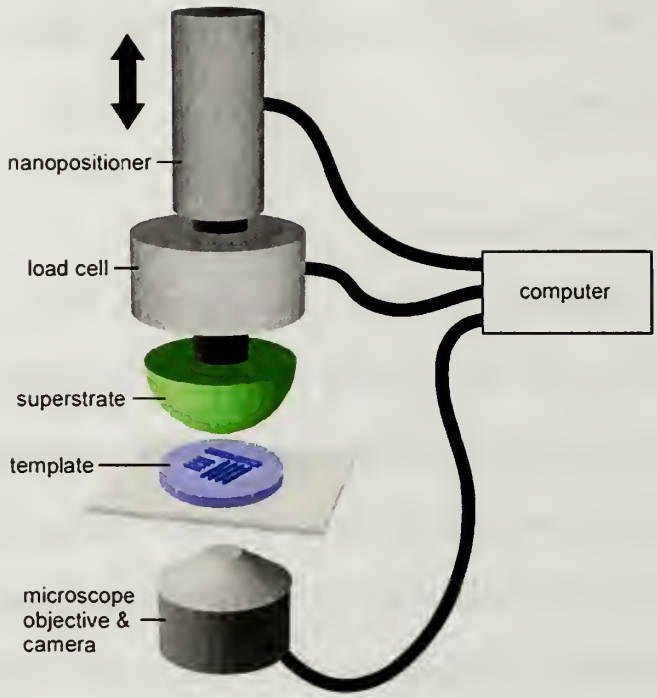

Figure A.2 – Schematic of our custom-built imprinting instrument. Unlike typical by S-FIL imprinters, we invert the setup by mounting the imprint template as the substrate. UV illumination occurs through the microscope objective, transmitting through the backside of the template. Rather than use a typical planar superstrate, we adopted a hemispherical superstrate. This eliminates many of the alignment issues that arise in nanoimprinting.

All of our imprinting experiments are performed at room temperature and the procedure is summarized in Fig. A.3: 1) A rigid hemispherical indenter (R = 2 mm) made of NO60 optical adhesive, is aligned with a selected patterned region of the template (which is mounted above the inverted microscope). 2) The acrylate monomer solution (volume = 0.75 μL) is deposited onto the template with a micropipette. 3) The indenter is brought into contact with the monomer solution and then the monomer solution is cured under UV radiation (~5 MW/cm^2) for 5 min. 4) Upon completion of the photocuring process, the sample is allowed to rest for 50 s and then separated at a controlled separation rate of 5 μm/s.

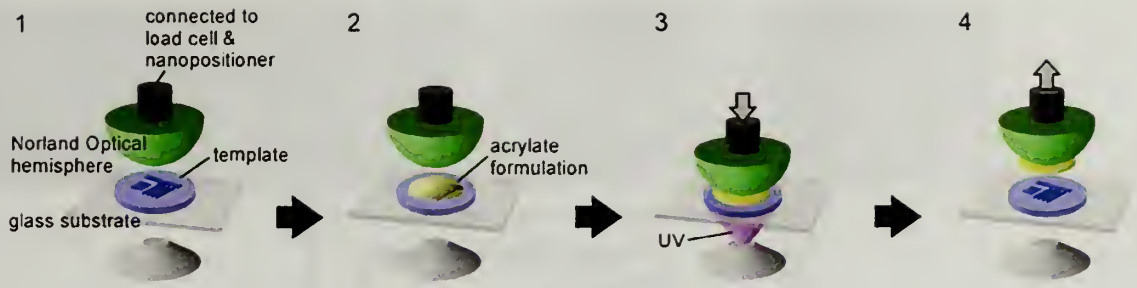

Figure A.3 – Procedure of an imprinting experiment. 1) A hemispherical lens is brought into alignment with the template. The hemispherical lens is made of NO60. 2) The UV-curable 2-hydroxethyl acrylate formulation is deposited onto the template. 3) The hemisphere is brought into contact with the acrylate solution and the UV is turned on which photopolymerizes the acrylate mixture. 4) Upon curing, the acrylate polymer is separated from the template. The stresses developed during photopolymerization as well as during separation are monitored with the load cell attached to the hemisphere.

Through our custom-written software interface, we monitor the force, P, time, t, displacement, δ and the cross-sectional area established between the template-polymer surface throughout the entire imprinting process. The results for a typical imprinting experiment are shown in Fig. A.4. For our sign convention, a positive value of force is tensile. Data collection begins at t = 0 s. After 10 s of hold time, the UV source is turned on and the polymerization of the acrylate mixture begins. Past t = 310 s, the UV is turned off and the acrylate polymer is allowed to rest for 50 s. Subsequently, the nanopositioner retracts at a crosshead speed of 5 μm/s, and separation proceeds. As the acrylate film adheres strongly to the hemispherical indenter, the separation occurs at the template-acrylate interface. The force reduces to a zero value as final separation occurs.

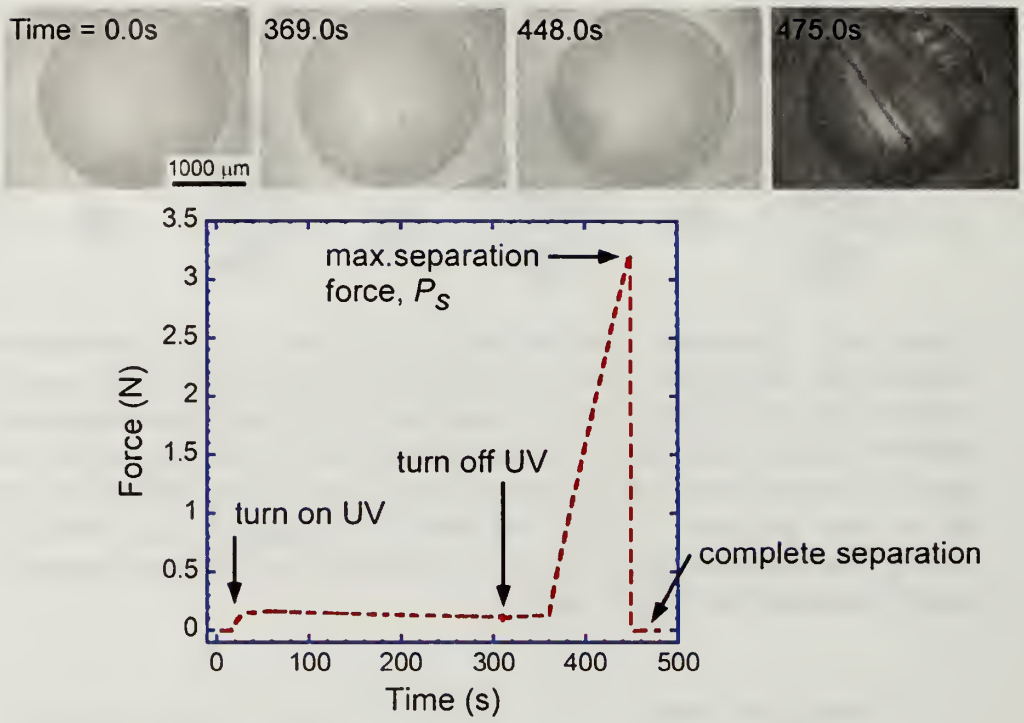

Figure A.4 – Force-time curve generated from an imprinting experiment. The acrylate is cured for 5 min. Following a 50 s hold time, the acrylate polymer is released from the template. Separation occurs when the maximum separation is reached. The optical microscope images correspond to the contact area established during the experiment.

A.3. Results and Discussion

A3.1. Cure history

Representative stress histories for all three imprint template materials are shown in Fig. A.5. In all three cases, a tensile force develops immediately upon UV illumination. This tensile stress is attributed to the volume shrinkage of the acrylate film as it photopolymerizes. The magnitude of this shrinkage stress is identical for the softer PDMS and PDMS-u templates but twice as great for the NO60-p system.

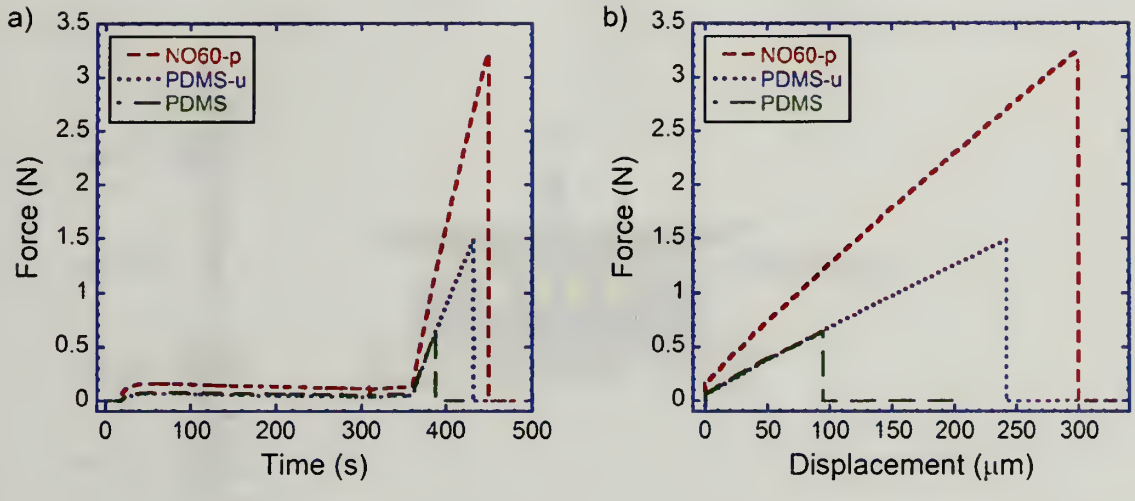

Figure A.5 – Results from the imprinting experiments. a) Representative force-time curves of the imprinting experiments for all three template materials. b) Force-displacement curves for the same experiments. The slope of the force-displacement curve corresponds to the stiffness of the template-acrylate system, which allows for the determination of the modulus of the system, E^*. The G_c values are determined by substituting P_s and E^* values into Eqn. (A.12).

The difference is due to the elastic moduli of the templates and can be explained by considering the imprinting system as mechanically equivalent to a set of springs connected in series (Fig. A.6). Each of the four components (superstrate, polymer film, template and substrate) having a unique stiffness, k that is proportional to the materials elastic modulus, E and the contact radius, a of the cross-sectional area, in other words,

$$k \propto Ea \tag{A.1}$$

As the components are connected in series, they all experience the same curing force P_{cure}, but a different degree of deformation, δ. Since the overall distance between the top of the superstrate and the bottom of the substrate stays fixed, the total deformation of the "spring" components must equal zero.

$$P_{cure} = P_{superstrate} = P_{film} = P_{template} = P_{substrate} \tag{A.2}$$

$$\delta_{total} = \delta_{superstrate} + \delta_{film} + \delta_{template} + \delta_{substrate} = 0 \tag{A.3}$$

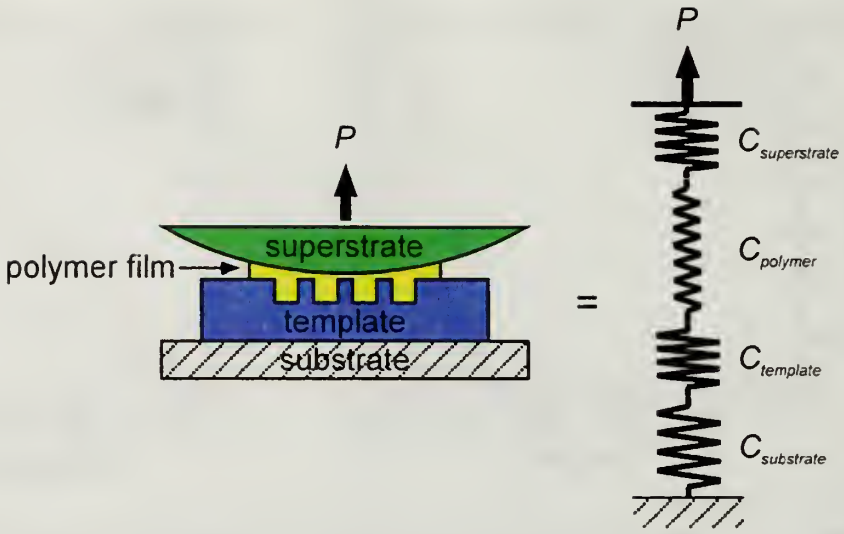

Figure A.6 – The imprinting assembly is mechanically equivalent to a system of springs connected in series, each component consisting of a unique compliance, *C*. When imprinting with a rigid template, the compliance of the soft, imprinted polymer is much greater than the other 3 components. As a result, the deformation due to curing stress will be localized within the polymer film.

The deformation in the curing film, δ_{film}, is directly related to the volume shrinkage caused by curing,

$$\varepsilon_{\text{film}} = \left(\frac{\Delta V}{V_o} + 1 \right)^{\frac{1}{3}} - 1 \tag{A.4}$$

and the original thickness of the monomer solution, h_{film}. This deformation is opposed by the deformation of the other components, assuming adhesion is maintained between all components.

$$\delta_{film} = \varepsilon_{film} \cdot h_{film} = \delta_{superstrate} + \delta_{template} + \delta_{substrate} \tag{A.5}$$

Using the definition of stiffness, $k = P/\delta$, and the above equations, we determine a relationship for P_{cure}.

$$P_{cure} = (k_e)(h_{film})(\varepsilon_{film}) \tag{A.6}$$

where k_e is an effective stiffness that is related to the properties of each component:

$$\frac{1}{k_e} = \frac{1}{k_{superstrate}} + \frac{1}{k_{template}} + \frac{1}{k_{substrate}} = \frac{1}{C_1 a}\left\{\frac{1}{E_{superstrate}} + \frac{1}{E_{template}} + \frac{1}{E_{substrate}}\right\} \quad \text{(A.7)}$$

C_1 is a proportionality constant related to geometry and the Poisson's ratio of the component materials. In general, the template stiffness is defined by a combination of material's stiffness (as defined by its elastic modulus) and geometric stiffness (defined by the dimensions of the template such as its lateral size or thickness). For our imprinting geometry, the template stiffness scales with the modulus, E and contact radius, a. For templates with a stiffness significantly less than both the substrate stiffness and superstrate stiffness ($k_{template} << k_{substrate}$ and $k_{template} << k_{superstrate}$), only the elastic modulus of the template needs to be considered when determining the curing stress.

$$P_{cure} \approx C_1 a(h_{film})(\varepsilon_{film})(E_{template}) \quad \text{(A.8)}$$

For our experiments, Eqn. (A.8) is valid for PDMS templates, but Eqn. (A.6) must be used for the NO60-p templates. Accordingly, we can compare the cure stresses for PDMS and NO60-p using these equations:

$$\frac{P_{cure,NO60-p}}{P_{cure,PDMS}} = \frac{1}{2}\left(\frac{a_{NO60-p}}{a_{PDMS}}\right)\left(\frac{h_{NO60-p}}{h_{PDMS}}\right)\left(\frac{E_{NO60-p}^{*}}{E_{PDMS}^{*}}\right) \approx \frac{1}{2}(0.85)(0.5)(11) = 2.3$$

We see that this simple model provides explanation for the experimental curing stresses measured with different templates. More importantly, this simple relationship provides critical insight into the control parameters associated with defect generation during the curing process.

Eqn. (A.8) contains 3 adjustable parameters: 1) h_{film}, the initial thickness of the monomer solution, 2) ε_{poly}, controlled through the chemical formulation of the photocured polymer film (i.e., initiator, crosslinker, etc) and 3) $E_{template}$. The two parameters ε_{poly} and $E_{template}$, should be consistent for each imprint procedure in normal imprinting applications; whereas h_{film} may vary across the imprinted film due to short or long range roughness or vertical misalignment between the template and superstrate. Any deviation in h_{film} can have critical implications since P_{cure} can be directly related to defect generation. As we discuss below, the interfacial separation of the photocured film from the template can be described as an interfacial fracture event.

In all the imprinting experiments, all the templates used are patterned surfaces. Hence, the local fracture process involves a structured interface. In analyzing the overall separation process, we only consider the contact geometry on the global length scale while the local structured interfaces are ignored. As the template is globally flat, the fracture process can be described by a stress intensity factor, K_I that is related to P:[82]

$$K_I = \frac{P}{\sqrt{4\pi a^3}} \tag{A.9}$$

During the process, $P=P_{cure}$. If the applied K_I is greater than the material-defined K_{Ic}, then either local or global fracture will occur. This is equivalent to the previous discussion in Chapter 4 on the onset of separation when the applied adhesion energy reaches the critical adhesion energy release rate required for separation. During the cure process, K_{Ic} of the curing film is increasing constantly as P_{cure} also increases. If h_{film} is slightly different than the value used for materials design, P_{cure} could cause K_I to exceed

K_{Ic} during cure. This event would cause cohesive fracture in the curing layer across the entire template surface or within a local feature where hfilm varies. We have observed this result experimentally in imprinting experiments when h_{film} is improperly defined. Alternatively, if K_{Ic} for the film-template interface is sufficiently low, then premature adhesive failure will occur during the curing process. If the cured film is sufficiently stiff to prevent feature distortion, this failure mode will not produce defects and suggests the reason for success in decreasing defect generation through the improvement of surface chemistry. Overall, the physics behind Eqn. (A.5) and (A.6) demonstrates the importance of precisely controlling h_{film} and K_{Ic} during each imprinting step to ensure defect-free pattern replication.

A.3.2 Controlled separation

If premature fracture does not occur during the curing process, then defect generation may occur during the controlled separation process when the template is withdrawn from the cured polymer film at a defined separation rate. For perfect pattern transfer, separation is induced and limited to the interface between the cured polymer and the patterned template. Similar to the separation of an adhesive from a substrate, the interfacial separation process in imprinting can be modeled as a fracture event. Accordingly, the material property that governs the separation is K_{Ic}. If the applied K_I is greater than the interfacial-defined K_{Ic}, then separation proceeds. For elastic materials, K_{Ic} is related to the critical energy release rate, G_c by a simple relationship,

$$G_c = \frac{K_{Ic}^{\ 2}}{2E^*} \tag{A.10}$$

where E^* is equal to $E/(1-\nu^2)$.[82]

The parameter G_c (energy/area) gives an absolute measure of the strength of the template-polymer film interface. In other words, to separate the interface, a sufficient amount of applied energy, $G_{applied}$ must be supplied to overcome the energy barrier G_c. The lower limit of G_c is the thermodynamic work of adhesion, w,[22] or the work required to separate the interface (with energy $\gamma_{template\text{-}film}$) into their respective free surfaces, $\gamma_{template}$ and γ_{film}.[83]

$$w = \gamma_{template} + \gamma_{film} - \gamma_{template-film} \tag{A.11}$$

For polymers, the value of G_c is usually well above this theoretical minimum. The additional contribution of G_c is associated with the irreversible release of energy by polymer chains away from the template-polymer film interface. The classic model that accounts for energy dissipation is the Lake-Thomas model.[84] During the separation process, as the template displaces away from the polymer film, a certain amount of applied energy is stored within the polymer chains. However, as these strained polymer chains relaxes upon separation, the stored energy is dissipated and cannot contribute to separation process.

To measure G_c for the template-film interface, we analyze our imprint data with the well-established methodologies of the polymer adhesion community.[73] The specific analysis that is analogous to the S-FIL separation process is the characterization of a probe-type adhesion test. In these tests, a rigid probe of defined curvature contacts and separates from the polymer surface at a controlled velocity. Using the theory of Johnson, Kendall and Robert (JKR)[2] or an equivalent fracture mechanics approach, the applied force and interfacial area can be used to quantify G_c at which fracture occurs. In

the case of a flat probe separating from a flat polymer surface (i.e. imprint template separating from a cured polymer film), the $G_{applied}$ at the point of separation is:[3]

$$G_c = \frac{P_s^2}{8\pi a_{max}^3}\left(\frac{1}{E_{template}^*} + \frac{1}{E_{poly}^*}\right) \tag{A.12}$$

In this geometry, fracture proceeds in an unstable manner. In other words, upon initiation of a crack at the perimeter of contact, there is already sufficient stored elastic energy at the interface that allows the separation to "self-propagate". In this scenario, the instantaneous change in applied adhesion energy as a changes (specifically, a reduces) is:

$$\frac{dG_{applied}}{da} > 0$$

As a result, complete separation occurs nearly instantaneously after a peak tensile force is applied to the template-polymer film interface (Fig. A.4). Therefore, G_c is determined by knowing the elastic properties of the cured polymer film and the template and measuring the peak force and interfacial area during the template separation process. Regardless of the template material, the separation process is rate-dependent. Hence, the materials' properties (G_c and E) that govern separation will change depending on the rate of separation. For our materials, the relevant relaxation time-scales are much longer compared to our separation times. Therefore, we do not consider the rate-dependent effects here and regard the materials as primarily elastic systems.

To demonstrate this measurement, we compare the release properties of different template materials. Shown in Fig. A.7 are two plots comparing the $E_{template}^*$

and G_c for the three templates. As the plots show, G_c scales proportional with $E_{template}^*$, which suggests that a stiffer template requires more applied energy for the interface to separate. In all three cases, we did not observe any defects due to cohesive fracture on the imprinted polymer films with repeated imprinting trials using the same templates, which suggests that $G_c < G_{fracture}$ for these template-polymer film interfaces.

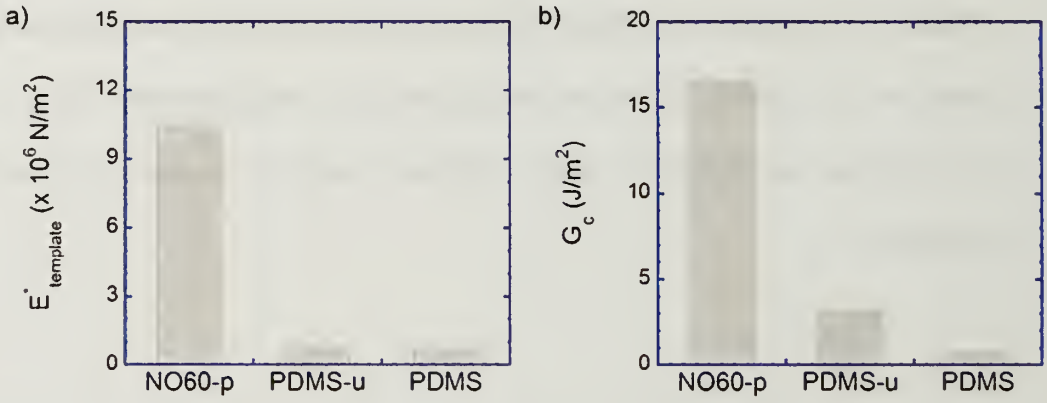

Figure A.7 – Plots of template modulus, $E_{template}^*$ and critical adhesion, G_c for the 3 templates. a) The $E_{template}^*$ values are determined from contact adhesion tests. b) Based on P_s and E^* values, the values of G_c are calculated using Eqn. (A.12).

One strategy to enhancing release and decreasing defects is to minimize G_c. A simple and straightforward approach to minimizing G_c, often employed by S-FIL development, is to reduce the surface energy of the inorganic template to the absolute minimum which is approximately 7 mJ/m^2 for a perfluorinated surface.[85] While the approach has demonstrated improved durability for the template, it does not completely eliminate the generation of defects in the imprinted polymer. The disadvantage of this approach is it lacks direct control over the separation pathway. In other words, slight changes in hfilm, or the local mechanical properties of the cured film could cause the separation crack to deviate from the template-film interface and cause a local cohesive

fracture, or defect. An alternative and directed approach in controlling the separation pathway is to adjust the interfacial mechanical properties.

If we consider the separation process described in Fig. A.8. During separation, the rigid template is displacing from the imprinted polymer film. As the polymer film is much more compliant than the template and the substrate, the deformation due to the separation process will be confined within the polymer layer. If this applied separation energy, $G_{applied}$ is less than the fracture strength $G_{fracture}$ of the polymer but greater than G_c of the interface ($G_c < G_{applied} < G_{fracture}$), then a clean adhesive separation will occur (Fig. A.7a). However, when the deformation energy exceeds the polymer layer's fracture strength ($G_c > G_{applied} > G_{fracture}$), a cohesive fracture will occur which is undesired. Since the topographic features (i.e. posts, lines) are high aspect ratio structures that are geometrically compliant, the fracture will occur at the base of these structures where the stress concentration is greatest. We can delocalize the deformation (and reduce the deformation experienced by the polymer film) if we lower the stiffness of the template such that local mechanical properties of the template match that of the polymer film.

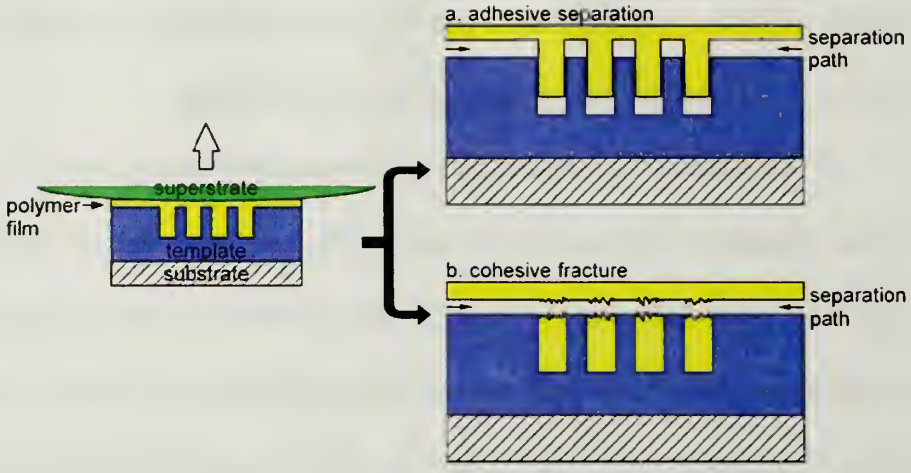

Figure A.8 – The two possible separation process of the polymer film from the template. a) Adhesive separation occurs whereby the separation path follows the contours of the interface between the polymer film and template. The template releases cleanly from the polymer film, resulting in a defect-free polymer film. b) In cohesive fracture, the separation path does not follow the contours of the interface and leads to fracture of the topographic features of the polymer film.

A.3.3 Balancing G_c and E^*

While minimizing G_c enhances release, a minimal value in G_c (approaching the thermodynamic limit of w) for the template surface often implies that the monomer solution has a low affinity to the template. As a result, the solution will not spread completely across the surface. To combat this problem, the S-FIL process often involve compressing (pressure ~4000 N/m^2) the rigid quartz template to overcome the surface tension,[78] which forces the monomer solution to spread and fill the topographic channels of the template. However, applying pressure to a soft, deformable template such as the PDMS template will lead to pattern distortion and even feature collapse. Therefore, for soft templates zero to low pressure can only be tolerated during film formation. For the PDMS and NO60-p systems, this procedure prevents complete replication of the smallest resolution features on our templates. Shown in Fig. A.9a is

the SEM micrograph of the polymer pattern imprinted by the PDMS template. While the PDMS template can successfully imprint lines ≥ 500 nm, poor registry develops for line widths less than 500 nm.

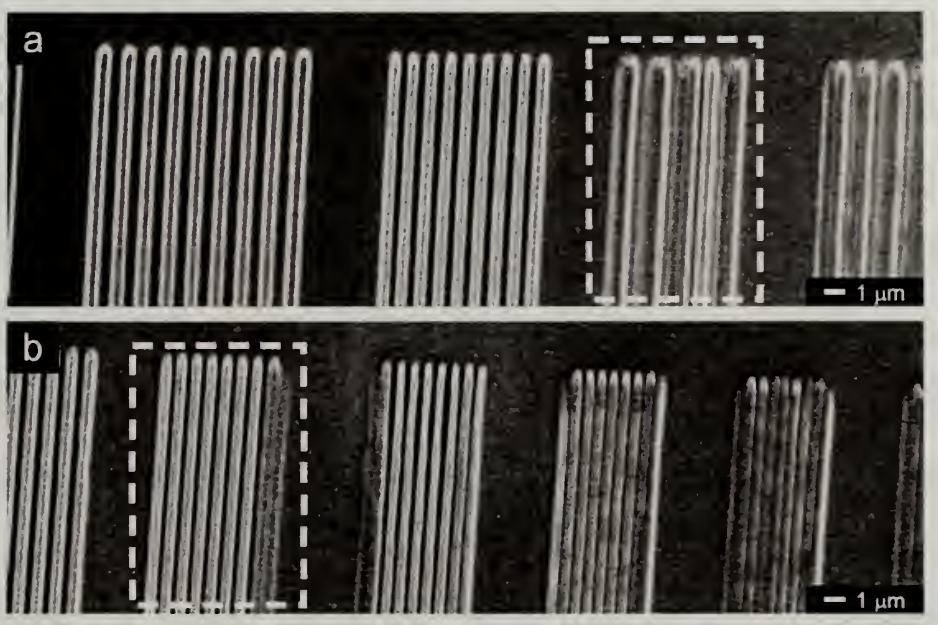

Figure A.9 – SEM micrographs of the imprinted acrylate polymer. a) When imprinted by the PDMS template, the feature registry for line widths below 500 nm becomes reduced. b) However, this is not so for the PDMS-u system, where the feature registry is maintained down to 350 nm.

To overcome this challenge while still retaining the same mechanical properties of the soft template, we altered the surface properties of PDMS through the UVO oxidation process. The UVO surface modification improved the wetting of the acrylate formulation to the PDMS-u surface by increasing the value of G_c slightly but maintaining nearly identical $E_{template}^*$ as PDMS. As the SEM micrograph shows (Fig. A.9b), this modified surface improves the replication of line widths well below 500 nm. This example illustrates the importance of selecting a template with the appropriate interfacial properties, G_c as well as mechanical properties, $E_{template}^*$ to ensure a successful imprint and proper release.

A.4 Summary

In this work, we have provided a methodology for quantifying release in S-FIL. The success of the imprinting process is dictated by proper imprinting and subsequent separation of the template from the molded polymer film. During cure, developing stresses can exceed the limits of the interfacial or bulk properties of the curing polymer and lead to early defect generation. These curing stresses can be tuned by three adjustable parameters: thickness of the film, volumetric shrinkage due to polymerization and the elastic moduli of the template and polymer. During separation, the generation of defects is directly related to the control of G_c, or K_{Ic} at the template-film interface. This interfacial property not only involves the surface energies of both the template and film, but also the mechanical properties of the near-interface regions. Therefore, the measurement of G_c, not surface energy, is critical for materials development in S-FIL. In addition to minimizing of G_c, the separation pathway has to be properly guided to minimize the generation of defects. A directed approach in controlling the separation pathway is by adjusting the interfacial mechanical properties. Contrast in the interfacial moduli of the cured polymer film and the template aids in the confinement of the crack to the interface during separation. Finally, balance between interfacial and the mechanical properties must be achieved to ensure not only proper separation, but also proper pattern formation.

A.5 Acknowledgements

We like to thank Prof. Kenneth C. Carter for providing the etched Si master templates. We also thank Louis Raobin in providing assistance with the SEM. We are also grateful to Ciba Speciality Chemicals in providing the IRGACURE photoinitiators for this work.

APPENDIX B

PATTERN CONTROL OF ADHESION FOR A CONFINED ADHESIVE LAYER

B.1 Introduction

For purposes of locomotion, nature uses many strategies in adapting to rough terrain and different environments. One strategy involves topography and viscous layer to control adhesion and release. In particular, we are interested in how nature controls adhesion and release with patterned, thin viscoelastic, adhesive layers. For example, echinoderms (sea urchins and sea stars) such as the *Paracentrotus lividus* and *Asterias rubens* secretes adhesive and de-bonding viscous layers for attachment and detachment purposes (Fig. B.1).[86] This mechanism of adhesion is not limited to marine animals, similar mechanisms are adopted by many insects such as the ant, *O. smaragdina*,[87] the bush cricket, *Orthoptera Tettigoniidae*,[88] and the locust, *Locusta migratoria*.[89] However, in all these systems, the adhesive layer only accounts for a portion of the adhesion. Additional contributions of adhesion include pattern geometry of the foot pad as well as the viscoelastic nature of the cuticle layer of the foot pad.[86, 89, 90] The geometric structure of the patterned foot pad enhances compliance and facilitates conformal contact with a rough surface. The secreted adhesive further improves conformal contact to the surface profiles. Hence, the combination of geometry and viscous behavior allows these creatures to adapt to a range of surface irregularities. Upon deposition of the viscous adhesive, the thinness of the adhesive coating along with the viscoelastic nature of the footpad enhances adhesion due to lateral confinement and rate effects.[86-91]

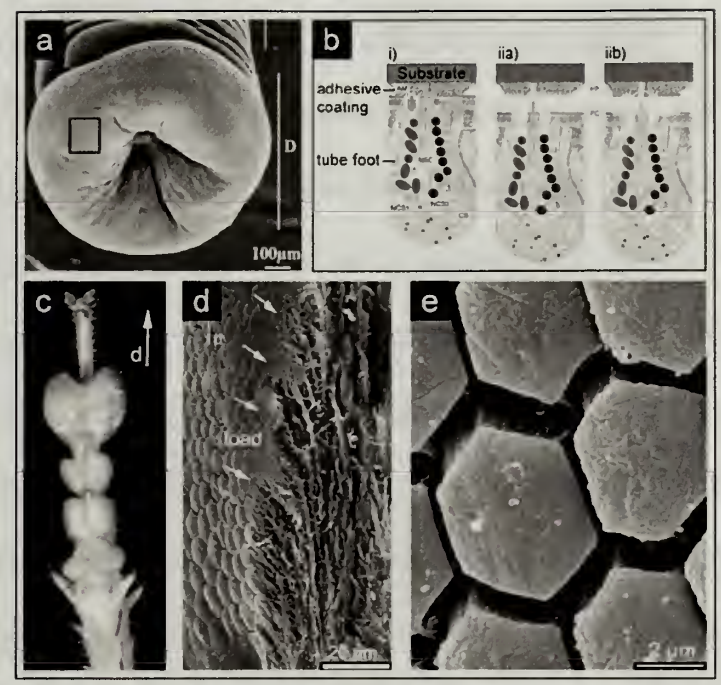

Figure B.1 – The footpad for various animals that utilize patterns and confined viscous layers to control adhesion. a) The tube foot of the sea star *Asteria rubens* reproduced from Santos *et al.*[86] The foot pad surface contains pores for secretion of the adhesive and debonding fluids. b) The attachment and detachment model of the tube foot, reproduced from Flammang *et al.*[92] i) During attachment, the adhesive material is secreted through the pores to "glue" the foot onto the substrate. The adhesive remains even after detachment. Two models have been proposed to describe the purpose of the secretion of the "debonding" fluid. iia) The competition model suggests that the de-adhesive screens ionic interactions between the adhesive and the substrate. iib) The enzyme model proposes that the debonding fluid breaks down the interface between the adhesive coating and the tube foot. c) The foot pad of the buch cricket, *Orthoptera Tettigoniidae*. d) The foot pad highlighting the hierarchical pattern structures. e) Magnified image of the pad surface illustrating the geometric patterns. Figures c), d), and e) reproduced from Gorb and Scherge.[88]

B.1.1 Synthetic Versions of Patterned Confined Adhesive Layers

Inspired by these natural examples, several researchers have developed synthetic variations of highly confined patterned thin elastic layers (Fig. B.2).[93, 94] The biomimetically patterned adhesives enhance adhesion by 1) controlling the stability of the crack propagation process and 2) spatial control over the development of

instabilities during separation. During peeling of the patterned elastic layer, the discontinuous nature of interface serves to disrupt the propagation of the crack. As we will discuss later, confinement enhances adhesion if instabilities such as cavities or fingering develop. The presence of the void regions within the patterned adhesive acts as nucleation sites for cavities. In order for the crack to propagate, the cavities must coalesce. Hence, the crack propagates intermittently; the crack "stops" upon nucleation of cavities and propagates only following growth and coalescence of the cavities. Furthermore, the control of adhesion is related to the pattern dimensions and density as both parameters influence the nucleation and density of the cavities. Successive crack initiation and propagation events lead to the increase in the W_{adh} of the patterned confined layer.

Although these synthetic systems demonstrate enhanced adhesion relative to smooth interfaces, they are primarily elastic systems and unlike the previously described marine adhesive, do not rely on viscoelastic effects to control adhesion. Here, we are interested in extending the concept of patterned adhesion to viscoelastic polymer systems and explore pattern interactions with confinement and viscoelastic effects. Before we describe our material system, we will briefly discuss the mechanisms of adhesion due to confinement and viscoelastic effects.

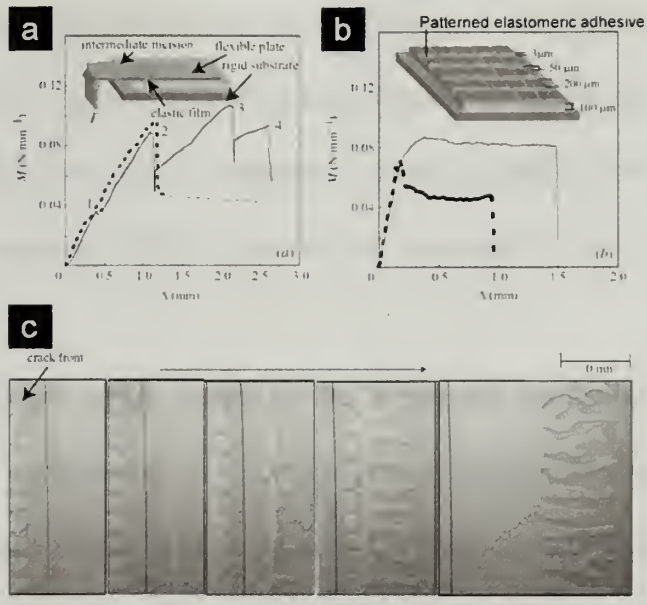

Figure B.2 – A biomimetically patterned thin elastic layer. a) The schematic of the peel test used to measure the adhesion of the films and the peeling moment vs. displacement results. b) For a patterned surface, the adhesion energy is increased as demonstrated by the greater hysteresis from the moment *vs.* displacement curve. c) The patterned surface nucleates fingering instabilities. The propagation of the crack requires the growth and coalescence of the instabilities. Figures reproduced from Ghatak *et al.*[93]

B.1.2 Control of Adhesion with Lateral Confinement

Lateral confinement can significantly alter the separation mechanisms of polymer adhesives to tune adhesion.[95] For a laterally confined adhesive (Fig. B.3), the lateral dimensions (area = πa^2) of the layer are much greater than its thickness, h.

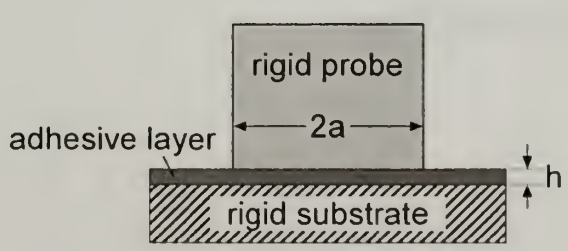

Figure B.3 – Geometry of a thin adhesive that is laterally confined due to adhesion to the substrate. At separation, significant stresses develop within the adhesive due to lateral strains.

Upon separation, as the adhesive stretches in the thickness direction, significant lateral strains develop within the material due to Poisson's effect. As this lateral strain cannot be easily accommodated, significant stresses develop within the adhesive layer which alters the mechanical response and ultimately affect the separation mechanism of the material.

Depending on the extent of the lateral stress, the adhesive can undergo 3 primary modes of separation (Fig. B.4):[95] 1) simple edge crack, 2) internal crack propagation and 3) cavitation. The simplest mode is simple edge crack, characterized by clean, adhesive separation at the interface where the edge of interfacial contact recedes in a radial manner. Internal crack propagation becomes the dominant mode of separation when the interface develops a significant hydrostatic stress that leads to the formation of a penny-shaped, internal crack. In cavitation, the initial development of the penny-shaped flaw is similar to internal crack propagation. However, the cavity expands into the bulk of the adhesive layer rather than growing at the interface. A subclass of cavitation is bulk fingering, where a shape-instability develops within the bulk adhesive. Both cavitation and bulk fingering lead to fibrillation, which is a principal mechanism of energy dissipation commonly observed in pressure-sensitive adhesives such as Scotch™ tape.

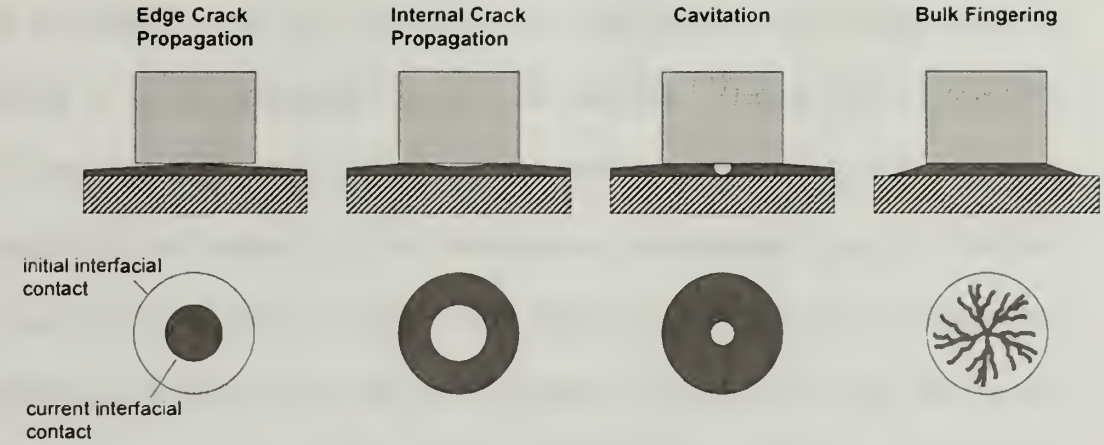

Figure B.4 – The modes of separation that a laterally confined adhesive can undergo. As the adhesive is laterally confined, significant stresses can develop within the adhesive and cause bulk instabilities such as cavitation and fingering to occur.

B.1.3 Viscoelastic Contributions to Adhesion

Viscoelastic systems offer additional adhesion mechanisms compared with their elastic counterparts in that their adhesive properties are history and rate dependent. During separation, a crack of length, a develops at the adhesive-substrate interface. The rate at which a changes with time, t is defined as the crack velocity ($v=-da/dt$). For polymer adhesives that demonstrate local viscoelastic response, the critical adhesion energy G_c is sensitive to the crack velocity. Empirically, the G_c scales with v by the following relationship:[96]

$$G_c = W\left[1+\psi(v)\right]\left[1+\varphi(a_T \cdot v)\right]$$

The term $W\left[1+\psi(v)\right]$ is the adhesion energy for an infinitely slow moving crack (i.e. $v \sim 0$) where φ can be 0 but ψ can have a large value.[96] Under true thermodynamic conditions, $W\left[1+\psi(v)\right]$ captures the "interfacial" energy dissipation due to the creation of new interfaces. The term $\left[\varphi(a_T \cdot v)\right]$ accounts for the dissipative contributions of the

"near-interfacial" contributions near the crack tip (Fig. B.6). Theoretical model proposed by De Gennes[97] describe the velocity dependence of G_c as dissipative processes that occur entirely within this interfacial region. The size-scale of the interfacial region is approximated as the product of the relaxation time of the polymer and the crack velocity; hence, a higher crack velocity results in an increase in the "interfacial" and "near-interfacial" regions. However, as the adhesive is a continuum, the classification of "interfacial" and "near-interfacial" contributions is difficult since the rate-dependent effects involves a range of length or time scales.

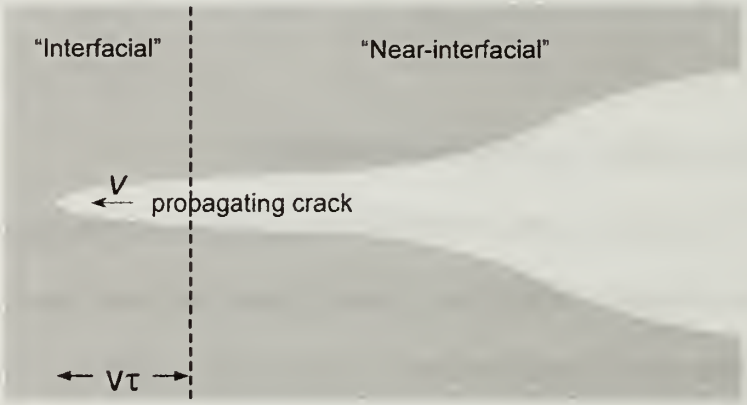

Figure B.5 – De Gennes' "Trumpet" Model that describes the rate-dependent adhesion energy of a soft polymer.[97]

B.1.4 Pattern Interaction with Confined Viscoelastic Layer

Patterns can provide a means to tune both the degree of lateral confinement and viscoelastic response of an adhesive. In this work, we are interested in understanding pattern interaction with a thin, viscoelastic adhesive. Specifically, to explore the effects of lateral confinement and viscoelasticity, we study the interaction between post patterns and an interprenetrated poly(*n*-butyl acrylate) (i-P*n*BA) polymer (Fig. B.3). As we demonstrate in this work, the patterns tune the adhesion of the thin i-P*n*BA layer by:

1) altering the mode of separation, 2) controlling of the debonding process by changing the stability of the crack propagation and 3) changing the global viscoelastic response.

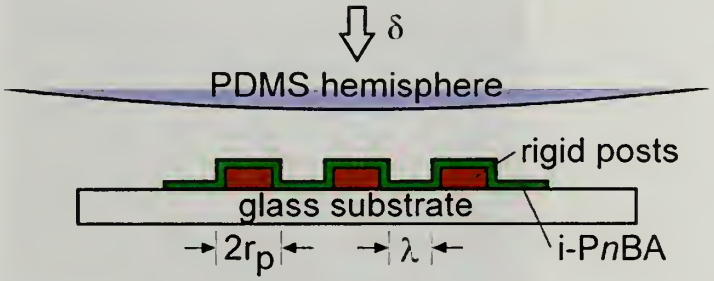

Figure B.6 – The topographically patterned, confined i-P*n*BA layer.

B.2 Experimental Approach

B.2.1 Patterned Adhesive

The patterned adhesive layer consists of a thin polymer adhesive layer that is conformally coated onto a patterned substrate (Fig. B.6). To generate this conformal adhesive layer, we use a combination of photolithography. In the next 2 sections, we will describe the fabrication process.

B.2.1.1 Combinatorial Design of Patterned Substrate

To investigate the effects of post size and spacing on adhesion, we use a combinatorial approach to prepare the patterned adhesive. The advantage of using a combinatorial library is that processing and thermal history is consistent across all the patterns. Figure B.8 illustrates a combinatorial library of SU-8 photoresist post patterns prepared using conventional photolithography.

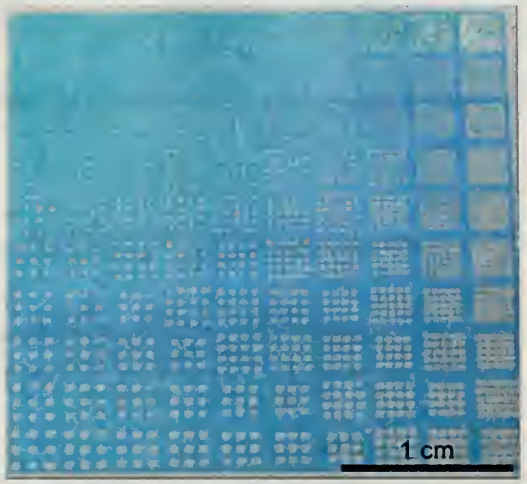

Figure B.7 – A combinatorial library of post patterns.

The example pattern library consists of a 10 by 10 array of discrete test cells where the post radii is varied along one axis (r_p = 25 to 250 μm) and post spacing is varied along the orthogonal axis (λ = 50 to 500 μm). For this work, a smaller version of the library of post patterns is prepared where the λ = 50 to 250 μm. Specifically, we prepare cylindrical posts of a commercial negative photoresist (Microchem SU8 2007, Newton, MA) by conventional photolithography (Fig. B.8). In general, there are a total of 5 steps to photolithography: coating, soft-bake, exposure, post-expose bake and development. To form a uniform layer of photoresist, we coat the photoresist solution onto a glass substrate by spin-coating. The thickness of the spun-coat layer depends on the viscosity of the solution and the spin-coating conditions (spin-speed, acceleration and time). Hence, a calibration curve should be established for a given solution. The calibration is developed by preparing samples at different spin-speeds for a given spin-coating acceleration and time and then measuring the film thicknesses with stylus profilometry. The calibration is developed by plotting the film thickness as a function of spin-coating speed to provide a general trend in thickness *vs.* spin-speed relationship.

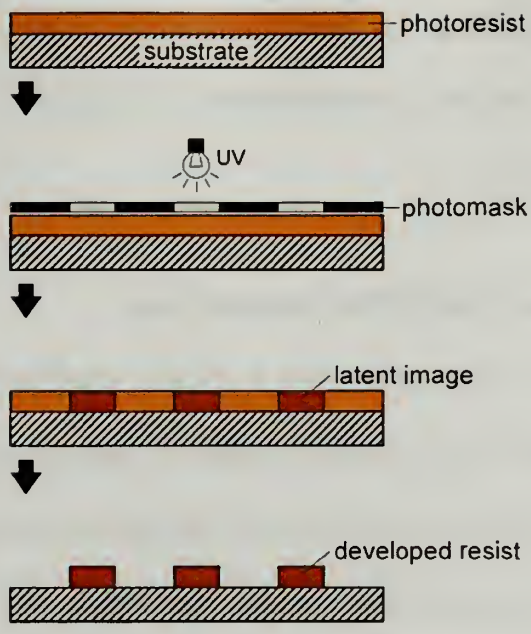

Figure B.8 – General photolithographic process for fabricating arrays of posts. SU-8, a commercially available photoresist, is used as the pattern material. The developed resist pattern will serve as the patterned substrate.

Following spin-coating, the residual solvent that remains in the resist is removed by a procedure called "soft-bake". Generally, soft-baking entails evaporating the solvent from the polymer film by heating the film at an elevated temperature. For the SU-8 resist, we bake the film at ~95°C for 1 min. and then allow the film to cool for ~5 min. The heating process should be done on a hot plate as opposed to an oven since directional heating from the substrate up facilitates evaporation of the solvent from the top, free surface of the film. Since the resist is light sensitive, the film is covered with foil to limit light exposure. Next, we pattern the resist by exposing the photopolymer with UV light through a photomask (λ = 365 nm, intensity = 15 MW/cm^2, exposure time = 50s). Similar to photography, this exposure develops a latent image in the resist. Following UV exposure, the resist is post-exposed bake (PEB, 1 min. at 95°C) to complete the photochemistry. At the end of this stage, the pattern should be clearly

visible. After allowing the resist to cool for ~5 min., the resist is developed by immersing it into the photodeveloper (~3 min.) to dissolve the non-patterned (unexposed) regions.

B.2.1.2 Interpenetrated P*n*BA Adhesive Layer

Next, we conformally coat a viscous, photocurable P*n*BA solution onto the patterned substrate. This solution consists of 2 primary components (Table B.1): linear chains of P*n*BA (Table B.1a) dissolved in a photocurable acrylate monomer formulation (Table B.1b). The linear P*n*BA polymer is synthesized by photopolymerization of *n*BA with 1 wt% of the two photoactive initiators (Ciba-Giegy Speciality Irgacure 184 and 819). The monomer (purchased from Sigma-Aldrich) is filtered through alumina to remove the inhibitors and then combined with the photoinitiators to yield a clear bright yellow low-viscosity liquid. Typically, we take 1 g of the solution and photopolymerize (OAI, intensity = 20 MW/cm^2) it for 6 min. to form the P*n*BA linear polymer.

The photocurable acrylate monomer (Table B.1b) solution is identical to the *n*BA formulation described in Chapter 4. To form the i-P*n*BA solution, 2.5 wt % of the linear P*n*BA is dissolved in the acrylate monomer formulation. The primary purpose of the linear chains is to increase the viscosity of the solution (into the consistency of syrup), which facilitates conformal coating of the acrylate formulation onto the patterned substrate.

a)

Linear polymer formulation	
Monomer	Photoinitiators
n-butyl acrylate	Ciba® Irgacure® 183; Ciba® Irgacure® 819

photopolymerize → Linear polymer: poly(*n*-butyl acrylate)

b)

Linear polymer	Soft Polymer Network		
	Monomer	Crosslinker	Photoinitiators
poly(*n*-butyl acrylate)	*n*-butyl acrylate (~98%)	ethylene glycol dimethacrylate (~2%)	Ciba® Irgacure® 183; Ciba® Irgacure® 819

Table B.1 – a) The photocurable *n*BA formulation used to synthesize the linear P*n*BA polymer. b) The photocurable i-P*n*BA formulation.

The patterned adhesive layer is fabricated by spin-coating the i-P*n*BA formulation onto the patterned substrate (Fig. B.9). Due to the viscosity of the formulation, the solution conformally coats the surfaces of the patterned substrate. Finally, we photocure the entire assembly to stabilize the i-P*n*BA layer and form the patterned adhesive.

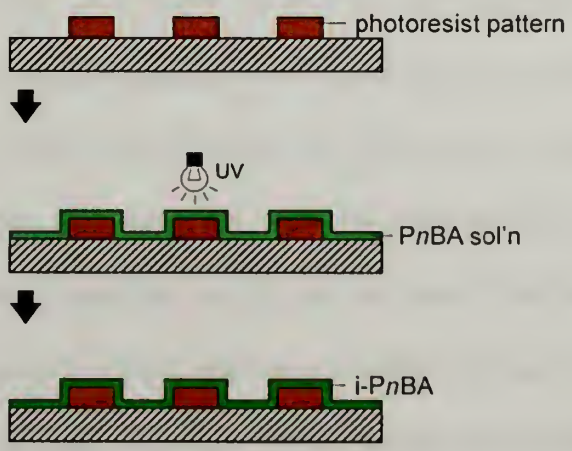

Figure B.9 – Procedure for conformal coating of the i-P*n*BA layer.

B.2.2 Contact Adhesion Tests

Similar to the testing approach described in Chapter 4, we use a Johnson, Kendall and Roberts (JKR) type contact adhesion test (CAT) to measure the adhesion of our materials. Since the patterns are on the micron length-scale, we monitor the contact area with optical microscopy while simultaneously recording the force, P, displacement, δ and interfacial contact history, $A = \pi a^2$ of the entire adhesion test. The test begins by bringing a spherical probe into contact with the elastomer at a fixed displacement rate (= 0.86 μm/s) until a predetermined compressive load is established. Once the interfacial contact is established, the probe is separated from the adhesive layer at the same displacement rate. The test stops when the interface completely separates. In all of the adhesion tests, we use a deformable crosslinked PDMS probe with $R = 5$ mm.

As discussed in Chapter 4 (Section 4.4.4), the results from the CAT allow for the determination of the materials' properties of G_c and E. However, G_c becomes difficult to determine in instances where the true contact area cannot be measured in a straight-forward manner. Materials where the contact areas are difficult to determine include patterned interfaces (such as our wrinkles in Chapter 4 or post patterns in this work) or interfaces with separation mode besides simple, clean edge separation. Instead, alternative adhesion descriptors (as discussed in Chapter 1) must be used. Again, we emphasize that most of these alternate descriptors are extensive quantities and hence, not materials-defined. Here, we use W_{adh} as adhesion descriptor of our materials. We choose to use W_{adh} as the primary descriptor since our material is viscoelastic and W_{adh} captures the energy dissipation during separation regardless if the dissipation occurs near the crack tip or within the bulk material.

The force-displacement curve (tack curve) for non-patterned i-P*n*BA is shown in Fig. B.10. For experimental consistency, this smooth i-P*n*BA film has the same thickness and consists of the same photoresist underlayer as the patterned i-P*n*BA. All the tack curves shown have the same axes scaling relative to the smooth i-P*n*BA. This is done for the purposes of comparing adhesion values for different patterns. The contact area images show that separation occurs by fingering mechanism for our material.

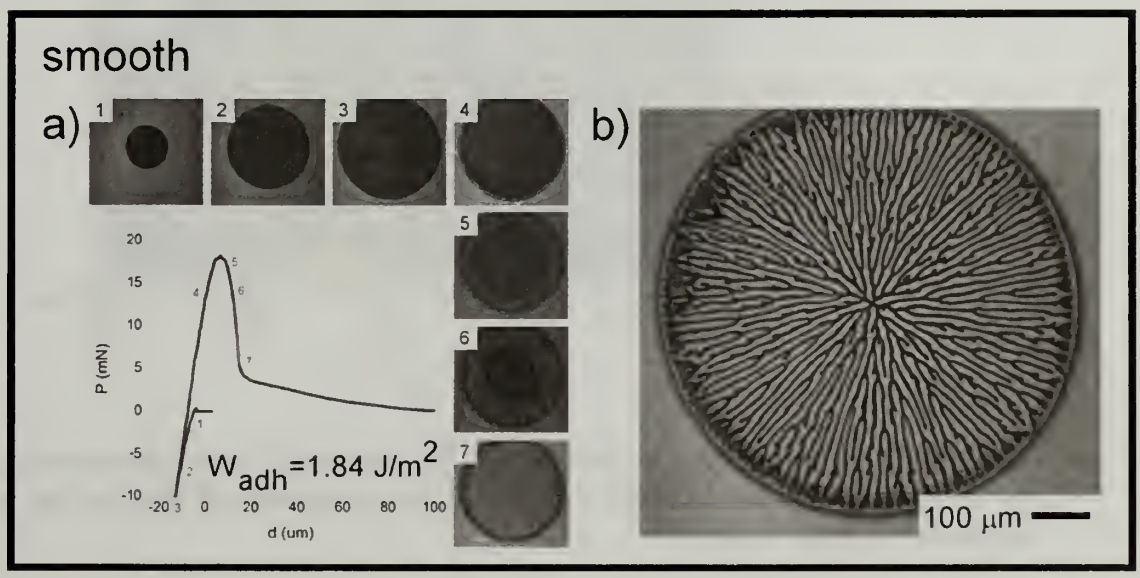

Figure B.10 – Adhesion test of the smooth i-P*n*BA. a) Tack curve for the smooth i-P*n*BA. b) Final contact area image showing separation by fingering.

B.3 Results and Discussion

We use the CAT to measure the adhesion of our combinatorial library of patterned i-P*n*BA adhesives. The W_{adh} results for all the patterns are presented in a normalized W_{adh} plot below (Fig. B.11). The normalized W_{adh} results indicate that the patterns enhance the release properties significantly relative to the smooth i-P*n*BA. In other words, in most instances, the patterns reduce the adhesion of the i-P*n*BA significantly. To understand the role of the post patterns in release enhancement, we

divide the results into 3 regions and discuss the mechanisms of enhancement separately (Fig. B12).

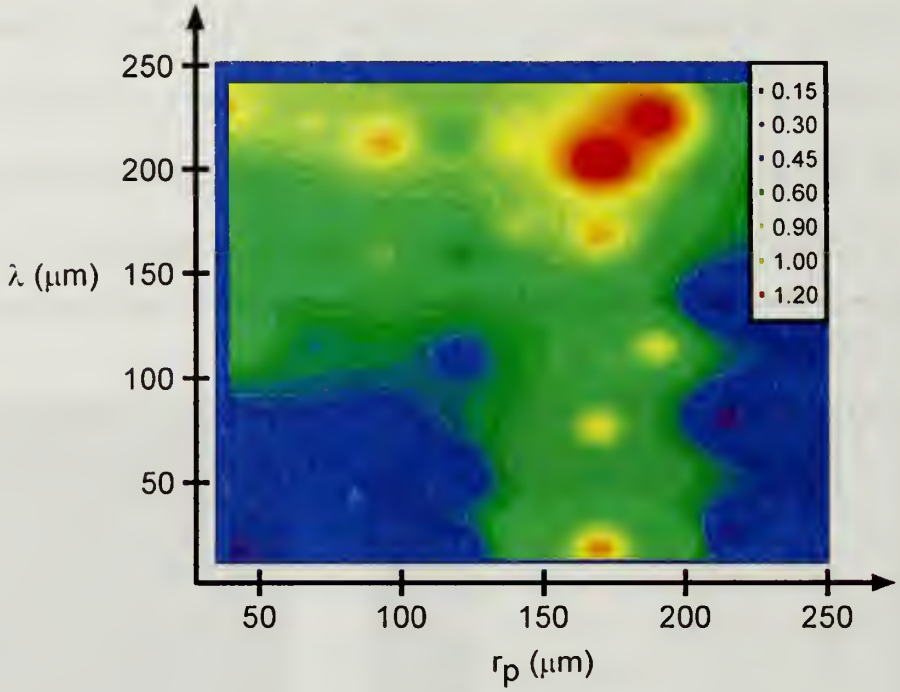

Figure B.11 – Contour plot of normalized W_{adh} as a function of post radius, r_p and post spacing, λ. The normalized W_{adh} is defined as the ratio of W_{adh} for the pattern versus the smooth i-P*n*BA.

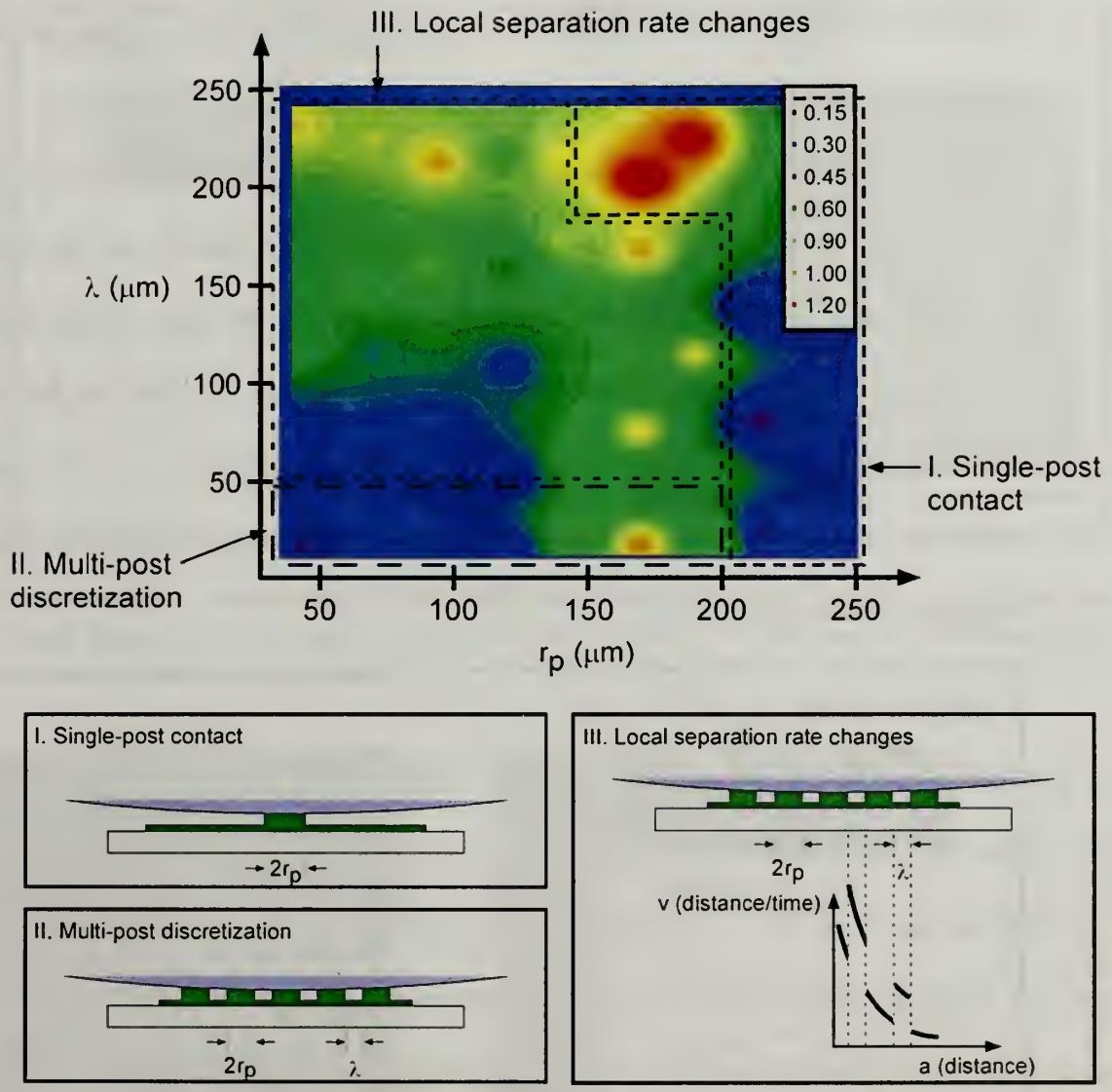

Figure B.12 – Mechanisms of adhesion provided by the post patterns.

B.3.1 Single-post Contact

As we have discussed previously, confinement effects can change the stress state of the adhesive significantly and alter the mode of separation of the material. The degree of lateral confinement is determined by the size of the interfacial contact relative to the adhesive thickness. For smooth adhesives, the size of the contact is controlled by the specific loading conditions and contact geometry. For a patterned adhesive, the

pattern provides an alternative means to control confinement since the post dimensions now determine the contact size.

The simplest scenario is the single-post contact geometry (Fig. B.13). Similar to the separation mode for the smooth i-P*n*BA, this geometry leads to the debonding by development of fingering instabilities (Fig. B.13). As both the mode of separation and overall contact area are nealy indentical, the value of W_{adh} is similar to that for the smooth adhesive. However, by increasing the post radius slightly (r_p = 201 μm, Fig. B.14), the separation mode switches into edge crack propagation and we observe a significant reduction in W_{adh}.

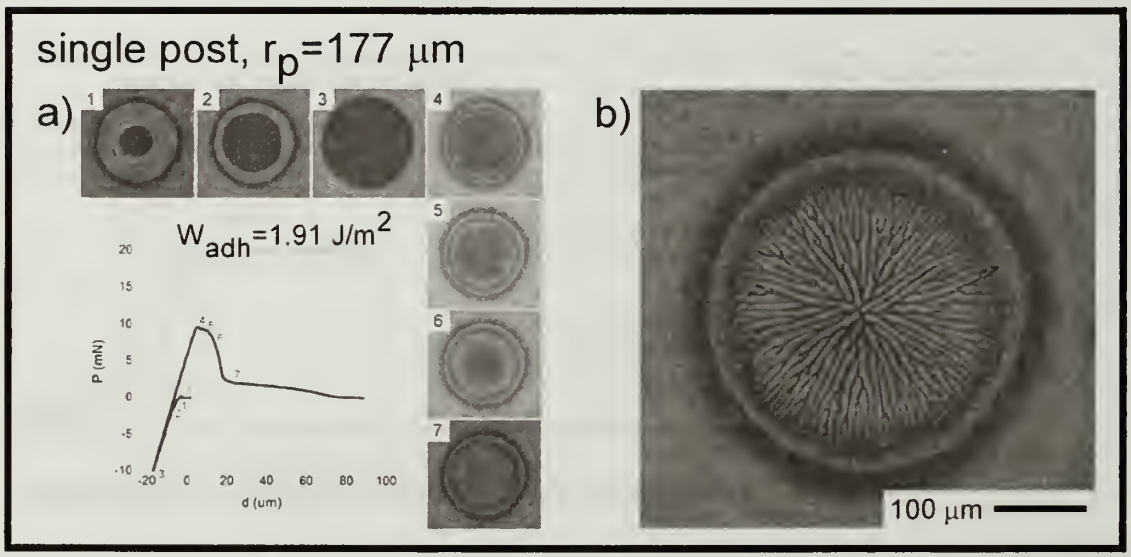

Figure B.13 – Adhesion test for single-post contact for post radius, r_p = 177 μm. a) Tack curve for single-post contact for post radius, r_p = 177 μm. b) The separation mechanism occurs by development of fingering instabilities.

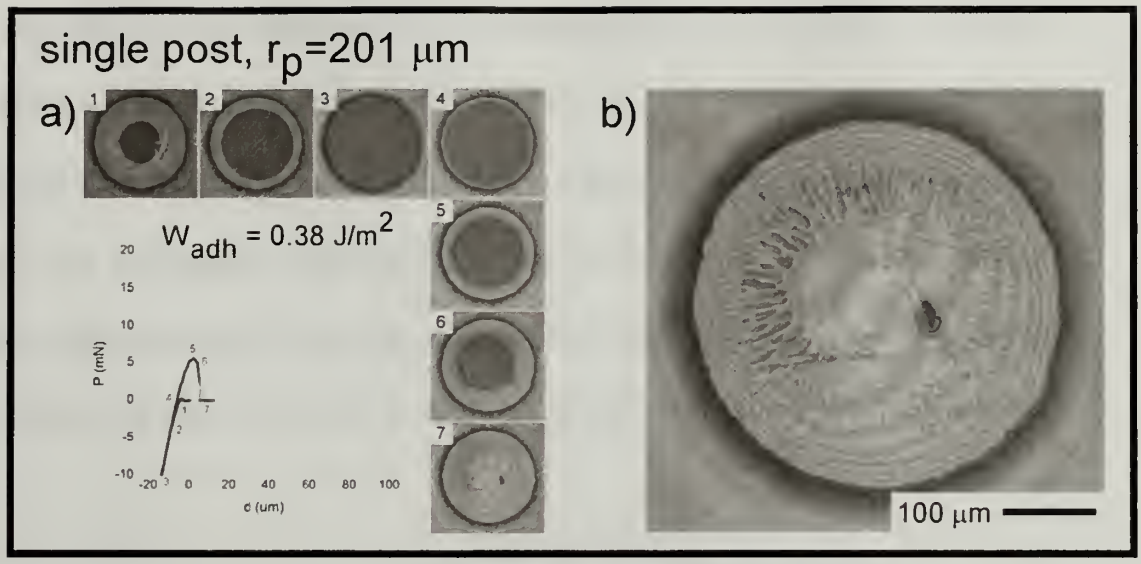

Figure B.14 – Adhesion test for single-post contact for post radius, r_p = 201 μm. a) Tack curve for single-post contact for post radius, r_p = 201 μm. b) The separation occurs by simple edge crack.

While more work is needed to better understand the origin of this change in deformation mode, we can develop a qualitative understanding by using the deformation map developed by Crosby and co-workers.[65] The deformation mode map allows for the prediction of the separation mode by relating the contact radius, a to two length-scales: a materials-defined length scale of G_c/E^* and a geometric length scale as defined by film thickness, h. For our materials, we develop a deformation mode map (Fig. B.15) and included the response for the smooth i-P*n*BA (1), i-P*n*BA post with r_p = 177 μm (2) and 201 μm (3), respectively. If we assume the i-PnBA to be an incompressible material (ν = 0.5), all three samples lie above this line therefore, all should deform by bulk fingering. However, this is not the case for the i-P*n*BA post of r_p = 201 μm since this sample separates by simple edge crack. This change in separation mode continues for all post radii greater than 201 μm up to 250 μm. We can explain this deviation qualitatively if we consider the compressibility of our system. Since the

elastomer contains a mixture of crosslinked and linear chains of P*n*BA, the material is most likely compressible, i.e. $\nu < 0.5$. At high levels of confinement, the deformation boundary is very sensitive to changes in ν, and if all three samples lie on a deformation boundary (as shown in Fig. B.15 for $\nu = 0.48$), slight changes in the boundary conditions of the stress distribution can cause switching between separation modes. In our materials, this change in boundary conditions is controlled by the post radius.

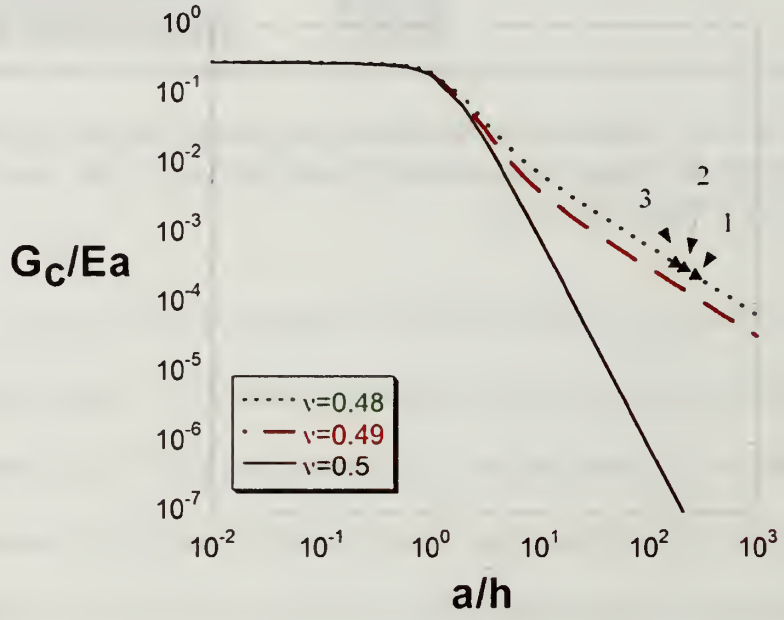

Figure B.15 – Deformation map for different values of Poisson' ratio, ν. Also included in the plot are experimental G_c/Ea values obtained for 3 i-P*n*BA samples: 1) smooth i-P*n*BA, 2) i-P*n*BA post with r_p = 201 μm and 3) i-P*n*BA post with r_p = 177 μm.

B.3.2 Multi-post Discretization

One of the effects of patterning the i-P*n*BA is the localization of crack initiation sites. More importantly, this specific contact geometry leads to the discretization of fingering instabilities. As Fig. B.16 shows, the fingering occurs only in regions of the adhesive where the posts are present. It is interesting to note that the fingering events

are all independent and confined within their respective post. The directionality observed for the posts along the perimeter is associated with the axi-symmetric nature of the hemispherical test probe.

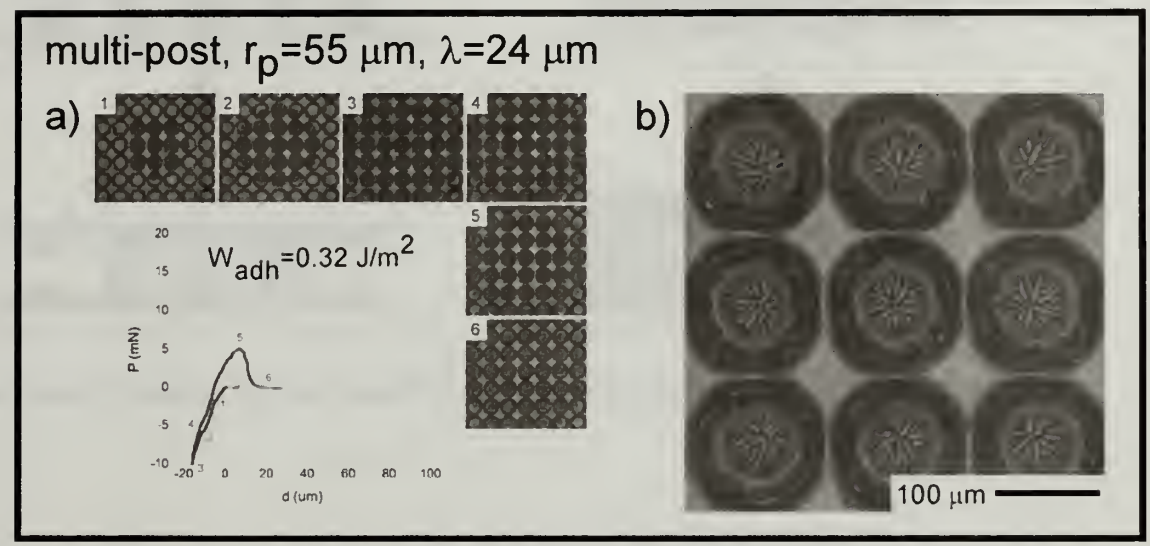

Figure B.16 – Adhesion test for multi-post contact. a) Tack for for multi-post contact. b) The posts break the fingering into discrete fingering regions.

The localization of the fingering instabilities results in a significan reduction in W_{adh} relative to the smooth i-P*n*BA. Qualitatively, we can understand this reduction in adhesion by comparing the separation process for the multi-post contact and the smooth i-P*n*BA (Fig. B.17). In the initial stage of separation, both the smooth and i-P*n*BA develop fingering instabilities. As the separation process continues, there is significant growth (characterized by extension of polymer fibrils away from the interface) of the fingering instabilities for the smooth i-P*n*BA system and leads to significant energy dissipation (and W_{adh}) away from the interface. However, this is not true for the patterned i-P*n*BA. Due to the contact line defined by the perimeter of each post, the separation process propagates in an unstable manner. As the probe continues to separate from the patterned interface, the propagation of the fingering instabilities terminates

prematurely. Hence, this unstable crack propagation limits fibril extension, which minimizes the energy dissipation and leads to an overall decrease in W_{adh}.

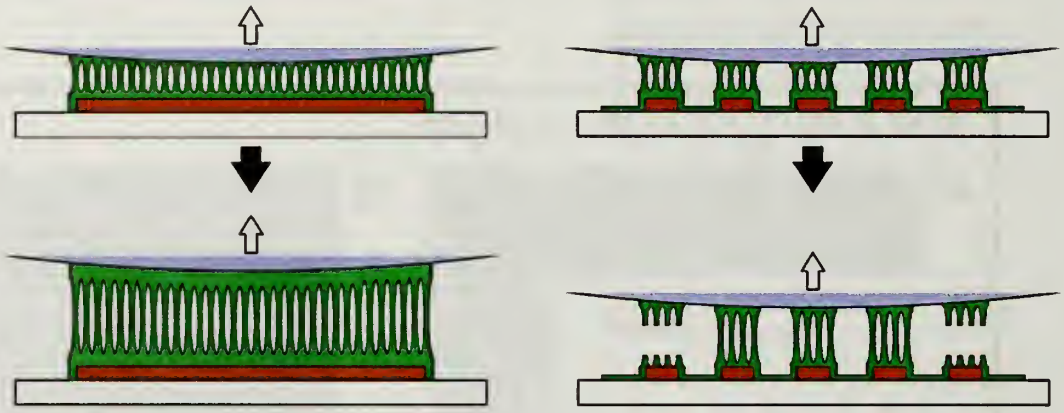

Figure B.17 – Comparison of the separation process for the smooth i-P*n*BA vs. the multi-post i-P*n*BA.

B.3.3 Viscoelastic Response versus Post Spacing

Post patterns can alter the global viscoelastic response of the adhesive. The effects of post patterns in tuning the viscoelastic response can be visually represented as an array of "speed bumps" for an advancing crack. Both the size (as represented by r_p) and spacing, λ will change the local crack velocity and alter the mechanical response of the viscoelastic polymer. Changes in the mechanical response can alter the extent of irreversible energy dissipation of the viscoelastic polymer adhesive.

As we demonstrate below, adjusting the post spacing, λ leads to changes in the area fraction of fingering region. The area fraction of fingering is defined by the area of fingering within the center post normalized by the total area of the center post. As the figure shows, at a fixed post radius (r_p = 153 μm), the area fraction decreases with λ, which we attribute to a change in the local crack velocity. The increase in the local crack velocity changes the mechanical response of the viscoelastic adhesive and causes

the material to go from a fluid-like behavior (smaller E) to a more elastic-like response (larger E). An increase in the elastic modulus effectively reduces the G_c/Ea ratio changes the separation mode. In this instance, the i-P*n*BA adhesive transitions from a purely fingering separation to one that is more edge crack dominated as we increase λ. As a result, we observe a reduction in W_{adh}.

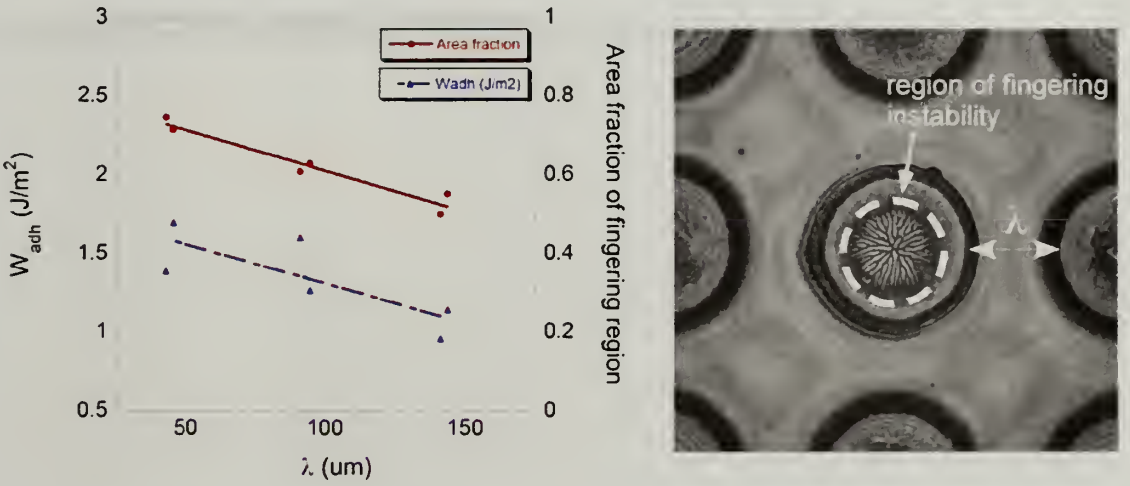

Figure B.18 – Effect of post spacing in reducing W_{adh}. This reduction in adhesion is a result of the decrease of the area fraction of fingering regions.

B.4 Conclusions

In this work, we demonstrate that a patterned interface can significantly change the adhesion of a confined, viscoelastic i-P*n*BA layer. Specifically, the post patterns tune the adhesion of the i-P*n*BA in 3 unique ways: 1) altering the local separation mode through lateral confinement, 2) controlling the initiation and propagation of fracture instabilities, and 3) changing the local crack velocity to alter the global viscoelastic response. We find that the control of adhesion for this material is due to changes in the mode of separation and this mode change is controlled by the contact geometry as defined by the post dimensions (post radius and spacing). Finally, the development of

bulk instabilities (such as fingering) during separation leads to significant energy dissipation and the interaction with patterns provides a means to control the development of these instabilities.

B.5 Acknowledgements

We thank Ciba Speciality Chemicals for providing the IRGACURE initiators.

REFERENCES

[1] E. P. Chan, C. Greiner, E. Arzt, A. J. Crosby, *MRS Bulletin* **2007**, *32*, 496.
[2] K. L. Johnson, K. Kendall, A. D. Roberts, *Proc. R. Soc. A.* **1971**, *324*, 301.
[3] D. Maugis, M. Barquins, *J. Phys. D: Appl. Phys.* **1978**, *11*, 1989.
[4] A. J. Crosby, M. Hageman, A. Duncan, *Langmuir* **2005**, *21*, 11738.
[5] T. Thomas, A. J. Crosby, *J. Adhes.* **2006**, *82*, 311.
[6] E. Arzt, S. Gorb, R. Spolenak, *PNAS* **2003**, *100*, 10603.
[7] K. Autumn, A. M. Peattie, *Integr. Comp. Biol.* **2002**, *42*, 1081.
[8] K. Autumn, M. Sitti, Y. C. A. Liang, A. M. Peattie, W. R. Hansen, S. Sponberg, T. W. Kenny, R. Fearing, J. N. Israelachvili, R. J. Full, *PNAS* **2002**, *99*, 12252.
[9] G. Huber, H. Mantz, R. Spolenak, K. Mecke, K. Jacobs, S. Gorb, E. Arzt, *PNAS* **2005**, *102*, 16293.
[10] M. Varenberg, A. Peressadko, S. Gorb, E. Arzt, *Appl. Phys. Lett.* **2006**, *89*, 121905.
[11] D. H. Kaelble, *Trans. Soc. Rheol.* **1960**, *4*, 45.
[12] C. Y. Hui, N. J. Glassmaker, T. Tang, A. Jagota, *J. R. Soc. Inteface* **2004**, *1*, 35.
[13] J. Y. Chung, M. K. Chaudhury, *J. R. Soc. Inteface* **2005**, *2*, 55.
[14] N. J. Glassmaker, A. Jagota, C.-Y. Hui, J. Kim, *J. R. Soc. Interface* **2004**, *1*, 23.
[15] N. J. Glassmaker, A. Jagota, C. Y. Hui, *Acta Biomaterialia* **2005**, *1*, 367.
[16] A. K. Geim, S. V. Dubonos, I. V. Grigorieva, K. S. Novoselov, A. A. Zhukov, S. Y. Shapoval, *Nat. Mater.* **2003**, *2*, 461.
[17] T. Tang, C. Y. Hui, N. J. Glassmaker, *Journal Of The Royal Society Interface* **2005**, *2*, 505.
[18] H. E. Jeong, S. H. Lee, P. Kim, K. Y. Suh, *Nano Letters* **2006**, *6*, 1508.
[19] M. T. Northen, K. L. Turner, *Current Applied Physics* **2006**, *6*, 379.
[20] K. Kendall, *Proc. R. Soc. A* **1975**, *341*, 409.
[21] A. Ghatak, L. Mahadevan, J. Y. Chung, M. K. Chaudhury, V. Shenoy, *Proc. R. Soc. A* **2004**, *460*, 2725.
[22] K. R. Shull, *Mater. Sci. Eng., R* **2002**, *36*, 1.
[23] K. Autumn, Y. A. Liang, S. T. Hsieh, W. Zesch, W. P. Chan, T. W. Kenny, R. Fearing, R. J. Full, *Nature* **2000**, *405*, 681.
[24] N. J. Glassmaker, A. Jagota, C.-Y. Hui, J. Kim, *J. R. Soc. Inteface* **2004**, *1*, 23.
[25] C. Greiner, A. del Campo, E. Arzt, *Langmuir* **2007**, *23*, 3995.
[26] M. Lamblet, E. Verneuil, T. Vilmin, A. Buguin, P. Silberzan, L. Leger, *Langmuir* **2007**, *23*, 6966.
[27] S. A. Mitchell, A. H. C. Poulsson, M. R. Davidson, N. Emmison, A. G. Shard, R. H. Bradley, *Biomaterials* **2004**, *25*, 4079.
[28] D. Falconnet, G. Csucs, H. M. Grandin, M. Textor, *Biomaterials* **2006**, *27*, 3044.
[29] A. Pallandre, K. Glinel, A. M. Jonas, B. Nysten, *Nanoletters* **2003**, *4*, 365.
[30] K. A. Wier, L. Gao, T. J. McCarthy, *Langmuir* **2006**, *22*, 4914.
[31] D. H. Kaelble, *Trans. Soc. Rheol.* **1959**, *3*, 161.
[32] A. Ahagon, A. N. Gent, *J. Polym. Sci.* **1975**, *13*, 1285.
[33] D. A. Ramrus, J. C. Berg, *J. Adhesion Sci. Technol.* **2004**, *18*, 1395.

[34] J. Cook, J. E. Gordon, *Proc. R. Soc. A* **1964**, 508.
[35] T. Tanaka, S.-T. Sun, Y. Hirokawa, S. Katayama, J. Kucera, Y. Hirose, T. Amiya, *Nature* **1987**, *325*, 796.
[36] N. Bowden, S. Brittain, A. G. Evans, J. W. Hutchinson, G. W. Whitesides, *Nature* **1998**, *393*, 146.
[37] C. M. Stafford, C. M. Harrison, K. L. Beers, A. Karim, E. J. Amis, M. R. Vanlandingham, H.-C. Kim, W. Volksen, R. D. Miller, E. E. Simonyi, *Nature Materials* **2004**, *3*, 545.
[38] D.-Y. Khang, H. Jiang, Y. Huang, J. A. Rogers, *Science* **2006**, *311*, 208.
[39] Y. Sun, V. Kumar, I. Adesida, J. A. Rogers, *Advanced Materials* **2006**, *18*, 2857.
[40] E. S. Matsuo, T. Tanaka, *Nature* **1992**, *358*, 482.
[41] W. T. S. Huck, N. Bowden, P. Onck, T. Pardoen, J. W. Hutchinson, G. W. Whitesides, *Langmuir* **2000**, *16*, 3497.
[42] C. Harrison, C. M. Stafford, W. Zhang, A. Karim, *Applied Physics Letters* **2004**, *85*, 4016.
[43] D. B. H. Chua, H. T. Ng, S. F. Y. Li, *Applied Physics Letters* **2000**, *76*, 721.
[44] N. Bowden, W. T. S. Huck, K. E. Paul, G. W. Whitesides, *Applied Physics Letters* **1999**, *75*, 2557.
[45] S. J. Kwon, J.-H. Park, J. G. Park, *Physical Review E* **2005**, *71*, 011604/1.
[46] R. C. Hayward, B. F. Chmelka, E. J. Kramer, *Macromolecules* **2005**, *38*, 7768.
[47] W.-F. Chen, T. Atsuta, *Theory of Beam-Columns*, Vol. 1, McGraw-Hill, Inc, New York **1976**.
[48] K. O. Friedrichs, J. J. Stoker, *PNAS* **1939**, *25*, 535.
[49] C. E. Pearson, *J. Aeronaut. Sci.* **1950**, *17*, 417.
[50] W. H. Wittrick, *Aeronaut. Quart.* **1953**, *4*, 151.
[51] K. Efimenko, M. Rackaitis, E. Manias, A. Vaziri, L. Mahadevan, J. Genzer, *Nature Materials* **2005**, *4*, 293.
[52] H. G. Allen, *Analysis and Design of Structural Sandwich Panels*, Pergamon Press, Oxford **1969**.
[53] S. P. Timoshenko, J. M. Gere, *The Theory of Elastic Instability*, McGraw-Hill, New York **1961**.
[54] J. Groenewold, *Physcia A* **2001**, *298*, 32.
[55] K. Efimenko, W. E. Wallace, J. Genzer, *Journal of Colloid and Interface Science* **2002**, *254*, 306.
[56] C. L. Mirley, J. T. Koberstein, *Langmuir* **1995**, *11*, 1049.
[57] E. Cerda, L. Mahadevan, *Phys. Rev. Lett.* **2003**, *90*, 074302.
[58] E. Kim, G. M. Whitesides, *Chemistry of Materials* **1995**, *7*, 1257.
[59] S. N. Gorb, *Attachment devices of insect cuticle*, Kluwer Academic Publishers, Dordrecht **2001**.
[60] S. N. Gorb, M. Scherge, *Biological micro and nanotribology: Nature's solutions*, Springer-Verlag, Berlin **2001**.
[61] S. Kim, M. Sitti, *Appl. Phys. Lett.* **2006**, *89*.
[62] M. Lamblet, E. Verneuil, T. Vilmin, A. Buguin, P. Silberzan, L. Leger, *Langmuir* **2007**, *in press*.

[63] B. Aksak, M. P. Murphy, M. Sitti, *Langmuir* **2007**, *23*, 3322.
[64] E. Southern, A. G. Thomas, *J. Polym. Sci., Part A: Polym. Chem.* **1965**, *3*, 641.
[65] A. J. Crosby, K. R. Shull, H. Lakrout, C. Creton, *J. Appl. Phys.* **2000**, *88*, 2956.
[66] G. A. D. Briggs, B. J. Briscoe, *J. Phys. D: Appl. Phys.* **1977**, *10*, 2453.
[67] P. R. Guduru, *J. Mech. Phys. Solids* **2007**, *55*, 445.
[68] P. R. Guduru, C. Bull, *J. Mech. Phys. Solids* **2007**, *55*, 473.
[69] K. N. G. Fuller, F. R. S. Tabor, *Proc. R. Soc. Lond. A.* **1975**, *345*, 327.
[70] B. N. J. Persson, E. Tosatti, *J. Chem. Phys.* **2001**, *115*, 5597.
[71] K. L. Johnson, J. A. Greenwood, J. G. Higginson, *Int. J. Mech. Sci.* **1985**, *27*, 383.
[72] K. L. Johnson, *Int. J. Solids Structures* **1995**, *42*, 423.
[73] K. R. Shull, D. Ahn, W. L. Chen, C. M. Flanigan, A. J. Crosby, *Macromolecular Chemistry and Physics* **1998**, *199*, 489.
[74] S. Y. Chou, P. R. Krauss, P. J. Renstrom, *J. Vac. Sci. Technol. B* **1996**, *14*, 4129.
[75] S. Y. Chou, P. R. Krauss, P. J. Renstrom, *Applied Physics Letters* **1995**, *67*, 3114.
[76] S. Y. Chou, P. R. Krauss, P. J. Renstrom, *Science* **1996**, *272*, 85.
[77] T. Bailey, B. J. Choi, M. Colbum, M. Meissl, S. Shaya, J. G. Ekerdt, S. V. Sreenivasan, C. G. Willson, *J. Vac. Sci. Technol. B* **2000**, *18*, 3572.
[78] M. Colbum, A. Grot, B. J. Choi, M. Amistoso, T. Bailey, S. V. Sreenivasan, J. G. Ekerdt, C. G. Willson, *J. Vac. Sci. Technol. B* **2001**, *19*, 2162.
[79] B. D. Gates, Q. Xu, M. Stewart, D. Ryan, C. G. Willson, G. W. Whitesides, *Chemical Reviews* **2005**, *105*, 1171.
[80] H.-C. Scheer, H. Schults, F. Gottschalch, T. Hoffmann, C. M. Sotomayer Torres, *J. Vac. Sci. Technol. B* **1998**, *16*, 3917.
[81] K. L. Johnson, *Contact Mechanics*, Cambridge University Press, Cambridge **1985**.
[82] D. Maugis, M. Barquins, *J. Phys. D: Appl. Phys.* **1983**, *16*, 1843.
[83] R. J. Stokes, D. F. Evans, *Fundamentals of interfacial engineering*, Wiley-VCH, Inc., New York **1997**.
[84] G. J. Lake, A. G. Thomas, *Proc. Roy. Soc. London A* **1967**, *300*, 108.
[85] T. Nishino, M. Meguro, K. Nakamae, M. Matsushita, Y. Ueda, *Langmuir* **1999**, *15*, 4321.
[86] R. Santos, S. Gorb, V. Jamar, P. Flammang, *The Journal of Experimental Biology* **2005**, *208*, 2555.
[87] W. Federle, M. Riehle, A. Curtis, R. J. Full, *Integr. Comp. Biol.* **2002**, *42*, 1100.
[88] S. Gorb, M. Scherge, *Proc. R. Soc. Lond. B.* **2000**, *267*, 1239.
[89] W. Votsch, G. Nicholson, R. Muller, Y.-D. Stierhof, S. Gorb, U. Schwarz, *Insect Biochemistry and Molecular Biology* **2002**, *32*, 1605.
[90] S. Gorb, Y. Jiao, M. Scherge, *J. Comp. Physiol. A* **2000**, *186*, 821.
[91] S. N. Gorb, E. V. Gorb, *The Journal of Experimental Biology* **2004**, *207*, 2917.
[92] P. Flammang, A. Michel, A. van Cauwenberge, H. Alexandre, M. Jangoux, *The Journal of Experimental Biology* **1998**, *201*, 2383.
[93] A. Ghatak, L. Mahadevan, J. Y. Chung, M. K. Chaudhury, V. Shenoy, *Proc. R. Soc. Lond. A.* **2004**, *460*, 2725.

[94] J. Y. Chung, M. K. Chaudhury, *J. R. Soc. Lond. Inteface* **2005**, *2*, 55.
[95] A. J. Crosby, K. R. Shull, H. Lakrout, C. Creton, *Journal of Applied Physics* **2000**, *88*, 2956.
[96] K. R. Shull, D. Ahn, W.-L. Chen, C. M. Flanigan, A. J. Crosby, *Macromol. Chem. Phys.* **1998**, *199*, 489.
[97] P. G. de Gennes, *Langmuir* **1996**, *12*, 4497.

5591.9